

# UC Irvine

## UC Irvine Electronic Theses and Dissertations

### Title

Folded MEMS approach to NMRG

### Permalink

<https://escholarship.org/uc/item/9vh9r5hf>

### Author

Gundeti, Venu Madhav

### Publication Date

2015

Peer reviewed|Thesis/dissertation

UNIVERSITY OF CALIFORNIA,  
IRVINE

Folded MEMS approach to NMRG

THESIS

submitted in partial satisfaction of the requirements  
for the degree of

MASTER OF SCIENCE

in Engineering with concentration in Materials and Manufacturing Technology

by

Venu Madhav Gundeti

Thesis Committee:  
Professor Andrei M. Shkel, Chair  
Professor Peter Burke  
Dr. Lawrence Kulinsky

2015



# DEDICATION

To Mom, Dad & Sis

# TABLE OF CONTENTS

	Page
<b>LIST OF FIGURES</b>	<b>vi</b>
<b>LIST OF TABLES</b>	<b>viii</b>
<b>ACKNOWLEDGMENTS</b>	<b>ix</b>
<b>ABSTRACT OF THE THESIS</b>	<b>x</b>
<b>1 Introduction</b>	<b>1</b>
1.1 Motivation . . . . .	1
1.2 Background . . . . .	2
1.3 Miniaturization Trends . . . . .	5
1.4 Contribution in Thesis . . . . .	6
1.5 Thesis Outline . . . . .	7
<b>2 Basics of NMRG</b>	<b>8</b>
2.1 NMRG - Theory of Operation . . . . .	8
2.2 Optical Pumping . . . . .	10
2.3 Spin Exchange . . . . .	12
2.4 Xe Magnetization . . . . .	14
2.5 Rb Magnetometer . . . . .	16
2.5.1 Dehmelt Detection . . . . .	16
2.5.2 Faraday Detection . . . . .	17
<b>3 Design Approach</b>	<b>18</b>
3.1 Coils . . . . .	19
3.1.1 Design . . . . .	20
3.1.2 Fabricated Samples . . . . .	23
3.1.3 Characterization . . . . .	24
3.2 Heaters . . . . .	25
3.2.1 Characterization . . . . .	26
3.2.2 Magnetic Field from Heaters . . . . .	27
3.3 Vapor Cell . . . . .	28
3.3.1 Fabrication . . . . .	28
3.3.2 Characterization . . . . .	29

3.4	Folded Structure . . . . .	29
3.4.1	Design . . . . .	30
3.4.2	Practical Consideration for the Design . . . . .	30
3.4.3	Optical Modeling for the Folded Structure . . . . .	31
3.4.4	Optical Characterization of Dielectric Mirrors . . . . .	33
3.4.5	Fabrication of Folded Structure . . . . .	35
3.4.6	Assembly of Folded Structure . . . . .	36
3.4.7	Optical Characterization of Folded Structure . . . . .	37
3.4.8	Miniaturization of Folded Prototype . . . . .	37
3.5	Novel Design for Folded Structure . . . . .	38
3.5.1	Redesign of Helmholtz Coils . . . . .	40
3.5.2	Mask Design . . . . .	40
3.5.3	Fabrication . . . . .	42
3.5.4	PCB Design for Assembly . . . . .	42
3.5.5	Assembly . . . . .	43
3.5.6	Metallic Mirror Comparison . . . . .	44
3.6	Magnetic Shielding . . . . .	45
3.6.1	Analytical Modeling . . . . .	46
3.6.2	Design . . . . .	47
3.6.3	FEM Modeling . . . . .	48
3.6.4	Manufactured Shields . . . . .	50
<b>4</b>	<b>Experimental Setup and Characterization</b>	<b>51</b>
4.1	VCSEL/Optics Setup . . . . .	51
4.1.1	VCSEL Characterization . . . . .	52
4.2	DC Heater Oven . . . . .	53
4.3	Macro Coils/Shields . . . . .	53
4.3.1	Coil Calibration/Degaussing . . . . .	55
4.4	Rb Macro Vapor Cell Characterization . . . . .	56
4.4.1	Zeeman Resonances . . . . .	56
4.4.2	Rb Magnetometer using Macro Cell . . . . .	57
4.5	Micro Vapor Cell Magnetometer . . . . .	58
4.5.1	NMR Setup . . . . .	59
4.5.2	Zeeman Resonances and Magnetometer . . . . .	62
4.5.3	Magnetometer Sensitivity . . . . .	62
4.5.4	Alternate Magnetometer Configuration . . . . .	63
4.6	Estimation of Xe Signal Level . . . . .	64
4.6.1	AC Heater Implementation . . . . .	66
4.6.2	Experiments with TOptica Laser . . . . .	67
4.6.3	Xe Response Spectrum . . . . .	68
4.7	Experiments for Relaxation Time Measurements . . . . .	69
4.7.1	DC Offset Cancellation . . . . .	69
4.7.2	Primary DC field (Z axis) Estimation . . . . .	70
4.7.3	Cross Axis Rejection Ratio . . . . .	70
4.7.4	Xe Drive Amplitude Optimization . . . . .	71

4.7.5	Estimation of $\pi$ and $\pi/2$ pulses . . . . .	72
4.7.6	Relaxation Time Measurements . . . . .	73
<b>5</b>	<b>Conclusion</b>	<b>74</b>
5.1	Improvements on Current Work . . . . .	75
5.2	Future Work . . . . .	75
	<b>Bibliography</b>	<b>76</b>
<b>A</b>	<b>Vendors</b>	<b>81</b>

# LIST OF FIGURES

	Page
2.1 Rb Zeeman splitting . . . . .	10
2.2 Hyperfine splitting of Rb . . . . .	11
2.3 Rb-Xe spin exchange optical pumping . . . . .	13
2.4 Xe Larmor precession frequency . . . . .	13
2.5 Spin-Spin relaxation time . . . . .	14
2.6 Spin-Lattice relaxation time . . . . .	14
3.1 Assembly flow of folded NMRG . . . . .	19
3.2 Folded Helmholtz coils with vapor cell . . . . .	19
3.3 Coil configuration . . . . .	20
3.4 Homogeneity vs radius of coils . . . . .	21
3.5 Homogeneity for Dipole and Octapole heaters . . . . .	22
3.6 Fabrication of Helmholtz coils . . . . .	23
3.7 Wire bonding of coils . . . . .	24
3.8 Characterization of coils . . . . .	25
3.9 Micro heaters . . . . .	26
3.10 Electrical connection to heaters . . . . .	26
3.11 Micro heater vs commercial heater . . . . .	27
3.12 Micro vapor cell . . . . .	29
3.13 Rb absorption dip at 65°C . . . . .	30
3.14 45° Folded pyramid structure design . . . . .	31
3.15 Optical modeling of folded structure . . . . .	32
3.16 Optical flux modeling . . . . .	32
3.17 Polarization modeling . . . . .	33
3.18 Setup for dielectric mirror characterization . . . . .	34
3.19 Polarization changes due to dielectric mirrors . . . . .	34
3.20 Fabrication mask for folded structure . . . . .	35
3.21 Assembled prototype using folded structure . . . . .	36
3.22 Optical testbed for folded structure . . . . .	37
3.23 Modified folded structures with metallic mirrors . . . . .	38
3.24 Novel design for folded structure . . . . .	39
3.25 Folding sequence of double folded structure . . . . .	39
3.26 Fully folded structure . . . . .	40
3.27 Modified Helmholtz coil design . . . . .	41

3.28	Layout masks for folded structure, coils . . . . .	41
3.29	Fabrication process flow . . . . .	43
3.30	PCB design . . . . .	43
3.31	Assembly of the new folded prototype . . . . .	44
3.32	Metallic mirror characterization setup . . . . .	45
3.33	Rb polarization vs laser power . . . . .	46
3.34	Shielding factor and volume vs number of shields . . . . .	47
3.35	Magnetic shield design . . . . .	48
3.36	Effect of optical ports on shielding factor . . . . .	49
3.37	Effect of spacing and thickness on shielding factor . . . . .	49
3.38	Shielding factor of 4 layer nested shields . . . . .	49
3.39	Manufactured 5 layer magnetic shield . . . . .	50
4.1	VCSEL mounting . . . . .	53
4.2	VCSEL characterization . . . . .	54
4.3	Heater assembly for macro vapor cell . . . . .	54
4.4	Macro shields on optical table . . . . .	55
4.5	Rb absorption vs wavelength for different temperature . . . . .	56
4.6	Zeeman resonance of Rb . . . . .	57
4.7	Rb magnetometer absorption and dispersion mode curves . . . . .	58
4.8	Optical setup for cell characterization . . . . .	59
4.9	Micro vapor cell aligned inside macro shields . . . . .	61
4.10	Orientation of magnetic fields . . . . .	62
4.11	Allan variance of Rb magnetometer . . . . .	63
4.12	Alternate Dehmelt technique . . . . .	63
4.13	Micro vapor cell magnetometer dispersion mode response . . . . .	64
4.14	Cell temperature vs time . . . . .	66
4.15	Schematic of AC heater . . . . .	67
4.16	Rb dip using TOptica laser source . . . . .	68
4.17	Spectrum showing Xe response . . . . .	69
4.18	Drive amplitude optimization for Xe <sup>131</sup> . . . . .	71
4.19	pi, pi/2 pulse amplitude optimization . . . . .	72
4.20	Relaxation time measurements . . . . .	73

# LIST OF TABLES

	Page
1.1 Different gyroscope technologies . . . . .	2
3.1 Homogeneities for different conditions with Helmholtz coils . . . . .	23
3.2 Optical characterization of dielectric mirrors . . . . .	34
3.3 Reflectivity comparison . . . . .	44
3.4 Polarization comparison . . . . .	45
4.1 VCSEL characterization . . . . .	53
4.2 Temperature vs Xe signal level . . . . .	65
5.1 Xe relaxation times . . . . .	75

# ACKNOWLEDGMENTS

I would like to thank my Advisor/Committee Chair Prof. Andrei Shkel for having given me this opportunity to work on one of the most interesting projects. His support, encouragement and constant feedback have helped me gain valuable insight in the process of problem solving and debugging issues.

I would also like to thank the INRF staff for their training and support with all the clean room aspect of this work. More importantly, UCI Microsystems Lab colleagues have had a great influence on me, especially with the crucial suggestions and sharing their expertise. I would also like to acknowledge Mike Larsen from Northrop Grumman for very valuable suggestions and feedback. This project was funded by Defense Advanced Research Projects Agency (DARPA) Microsystems Technology Office (MTO) under the microPNT program with Grant No. W31PQ-13-1-0008.

# ABSTRACT OF THE THESIS

Folded MEMS approach to NMRG

By

Venu Madhav Gundeti

Master of Science in Engineering with concentration in Materials and Manufacturing  
Technology

University of California, Irvine, 2015

Professor Andrei M. Shkel, Chair

Atomic gyroscopes have a potential for good performance advantages and several attempts are being made to miniaturize them. This thesis describes the efforts made in implementing a Folded MEMS based NMRG. The micro implementations of all the essential components for NMRG (Nuclear Magnetic Resonance Gyroscope) are described in detail in regards to their design, fabrication, and characterization. A set of micro-scale Helmholtz coils are described and the homogeneity of the generated magnetic field is analyzed for different designs of heaters. The dielectric mirrors and metallic mirrors are compared in terms of reflectivity and polarization change upon reflection. A pyramid shaped folded backbone structure is designed, fabricated, and assembled along with all the required components. A novel double-folded structure  $1/4^{\text{th}}$  the size of original version is fabricated and assembled. Design and modeling details of a 5 layered shield with shielding factor  $> 10^6$  and total volume of around 90 cc are also presented. A table top setup for characterization of atomic vapor cell is described in detail. A micro vapor cell based Rb magnetometer with a sensitivity of 108 pT/ $\sqrt{\text{Hz}}$  is demonstrated. The challenges due to DC heating are addressed and mitigated using an AC heater. Several experiments related to measuring the relaxation time of Xe are provided along with results. For Xe<sup>131</sup>, relaxation times of  $T_1 = 23.78$  sec,  $T_2 = 18.06$  sec and for Xe<sup>129</sup>,  $T_1 = 21.65$  sec and  $T_2 = 20.45$  sec are reported.

# Chapter 1

## Introduction

Gyroscope is a sensor used to measure the rotation of an object. They have become very prevalent in modern day usage in many gaming consoles, cell phones but primarily were first invented as a tool for navigational usage. It can be used to track the objects orientation from the initial state. A 3 axis gyroscope, combined with a 3 axis accelerometers can be used to create a self-contained inertial navigation system to track the objects location and orientation.

### 1.1 Motivation

Several implementations of gyroscopes have been introduced using traditional Si MEMS. These have the advantage of occupying very less area and reduced the cost of the whole system. But currently, this type of device cannot measure very small rotation rates. The navigational grade inertial measurement requires detection rates on the order of  $.001^\circ/\text{hr}$ . This is where atomic gyroscopes (based on Nuclear Magnetic Resonance (NMR)) come into play [1].

Traditional atomic gyroscopes were demonstrated as early as 1970. But the systems were bulky and very expensive. Driven by the MEMS batch fabrication features, there has been a considerable effort in miniaturizing atomic gyroscopes as well. Several advances have been made in similar products like the MEMS based atomic clock. But still to date, there is no commercially available MEMS based atomic gyroscope. Some very interesting advances have been made by Northrop Grumman [2]. The potential for high performance inertial sensors and recent successes of technology drives research to miniaturize such a complex system.

In this thesis, we will be exploring the concept of folded structure based NMR Gyroscope (NMRG). This approach combines the size, weight, power, and cost advantages of traditional Si sensors and couples them with the high stability and precision of an atomic gyroscope. Also, implementing all the required sensors into one folded assembly is a huge step towards creating the complete Inertial Measurement solution.

## 1.2 Background

Different gyroscope technologies are tabulated in Table 1.1 and are very broadly classified based on their physical principle of operation.

<b>Vibratory</b>	<b>Optical</b>	<b>Atomic</b>	<b>Other</b>
Tuning Fork	RLG	AIG	ESG
DTG	FOG	ASG	Super-fluid
CMG	IOG		
Wine Glass(HRG)			

Table 1.1: Different gyroscope technologies

Most mechanical vibratory gyroscopes work on the principle of conservation of angular momentum. Also called Coriolis Vibratory Gyroscopes (CVG), they are based on Coriolis effect that causes a coupling between the two resonant modes of a mechanical resonator when the system rotates. There are several variations of this kind of gyroscope namely tuning fork,

wine glass, ring/disk resonators, Dynamically Tuned Gyroscopes (DTG), Control Moment Gyroscope (CMG) to name a few [3]. The basic tuning fork gyroscope has two metal tines connected to a common metal base. The fork tines oscillate in their primary mode of vibration and when the whole system rotates, the tines precess due to Coriolis forces and amplitude of this motion is proportional to the rotation rate of the system [5, 4]. This basic device was invented in 1950 and many gyroscope implementations are based on this concept. DTGs [6] and CMGs [7] were the most prominent gyroscope technologies used for many space and military applications during the 1960s and 1970s. They had bulky mechanical moving parts and were costly to implement [3].

The most well known implementation of wineglass shaped resonator is the hemispherical resonator gyroscope (HRG). HRGs consist of a highly polished hemispherical fused quartz shell (main sensor) along with electrodes around this shell to actuate it [5, 8]. The vibration patterns on the shell are displaced due to Coriolis forces when the system rotates, which are picked up by the sense electrodes. HRGs have very high Quality factor(Q) and are very robust as they does not have any moving parts, but are very expensive due to sophisticated manufacturing process. These are extensively used for space applications.

Most implementations of optical gyroscopes are based on Sagnac effect. This is based on the phenomenon that light reaches faster along one path and slower on the other path if the system is rotating. The phase shift corresponds to the rotation rate and thus this effect can be used as a gyroscope. This concept led to making Fiber Optic Gyroscope (FOG) [10] and Ring Laser Gyroscope (RLG) [9]. In FOG, a laser source is split and injected into a single fiber cable, both in clockwise and anticlockwise directions. The beam traveling against the rotation of the system is relatively faster compared to the other. This phase shift is used for rotation rate measurement. In RLG, a difference in frequencies of two beams is measured to deduce rotation rate. Due to absence of any mechanical moving parts, these optical gyroscopes can measure very precise rotation rates and are used in many

space applications. RLGs are more robust and immune to temperature, vibration or shock. FOGs can achieve the same sensitivity but the measurements can vary based on ambient perturbations (shock, vibrations, thermal). FOGs are not used in aircraft inertial navigation for this reason [11].

Atomic gyroscopes can be broadly classified as Atomic Interference Gyroscope (AIG) or Atomic Spin Gyroscope (ASG) [12]. AIG uses similar concept of Sagnac effect by treating atoms as waves instead of particles and interacting with them using light. The specific concepts are clearly explained in the references [13, 14, 15]. AIGs have far superior performance compared to their optical counterparts. On the other hand, ASGs are mostly based on principles of Nuclear Magnetic Resonance (NMR). Several implementations of NMRGs were demonstrated during 1980s [16, 17]. The change in precession frequency of spin polarized nuclei are measured by applying a set of magnetic fields to determine the rotation rate of the system [35]. Most NMRG use spin exchange optical pumping phenomenon described in Chapter 2. Having no moving parts, NMRGs have better sensitivity and are immune to vibrations or shocks compared to their mechanical counterparts. However, generating very homogeneous magnetic fields is a very crucial parameter for operation. Earlier versions [18] used superconducting coils and shields and were very expensive and bulky to implement. A two isotope approach was also proposed to mitigate the requirement on stringent shielding [19].

Electrostatically suspended gyroscope (ESG) consists of a suspended rotating sphere in a vacuum cavity by means of electric field [5]. The rotation of the system can be measured relative to a local reference and the spin axis of the sphere. Though very precise, the measurement are very sensitive to imperfections on the sphere and manufacturing the sphere itself is a difficult endeavor. ESG was used in many specialized aircrafts, submarines, ships for its high accuracy despite being heavy and expensive [20].

Super-fluid gyroscope consists of a super-fluid  $\text{He}^4$  at very low temperatures contained in a

toroid with a small aperture [3]. Super-fluid does not exhibit viscosity. When the system rotates, measuring the amount of back flow from the aperture, the rotation rate can be deduced [21].

### 1.3 Miniaturization Trends

There has been significant effort to miniaturize most of the gyroscopes described above, owing to the emerging MEMS technology. Small area, low cost, low power consumption and high levels of integration are driving forces towards miniaturizing sensors. High integration leads to more programmability and better calibration algorithms and control loops can be implemented. First Si MEMS based gyroscopes had very low performances and were used mainly for consumer applications. There has been constant improvement in the performance of these Si MEMS gyroscopes and these are well aligned to substitute for most of the yesteryear technologies, even in inertial navigation applications.

One of the earliest implementations of MEMS CVG was a tuning fork gyroscope [22, 23]. In another implementation, a poly Si ring gyroscopes was implemented with a high aspect ratio combined poly and single crystal Si MEMS fabrication method [24]. Another variant called QMG (Quad Mass Gyroscopes) [25] has been demonstrated to have Q close to 1 Million and with appropriate calibration schemes can be used in inertial navigation systems [26].

Several MEMS based wine-glass resonator gyroscope have been implemented with a very high Q factor [27, 28]. Though they are not close to the performance of actual HRG, but there have been significant improvements in these MEMS based designs.

Integrated Optical Gyroscope (IOG) work on the same principle as RLG or FOG and the components are all fabricated mostly using semiconductor technology, thus taking advantage of size, cost and power advantages. The basic building block is called the SRL (semiconductor

ring laser). The latest advances in this regard are well documented in these references [3, 11].

Advances in semiconductor based optical sources propelled miniaturization of NMRG. Having no mechanical moving components, NMRG are immune to vibration or shock and have very high resolution and stability. Shrinking these sensors does get difficult due to several complementary Physics principles in operation. Some of the earliest attempts were made at NIST in building chip scale atomic clocks [29]. The Princeton University Group under Prof. Romalis has also published some implementations for atomic magnetometers and NMRG [30, 31]. Erik Eklund at UCI demonstrated a micro atomic magnetometer along with NIST and also implemented a novel glass blowing technique to batch fabricate spherical atomic vapor cells [35]. Northrop Grumman have made many major advances in implementing miniaturized NMRG [2]. Recent trends include fusion of different technologies to create a complete inertial measurement solution [32, 33].

## 1.4 Contribution in Thesis

This work takes forward the already established milestones in our lab in developing NMRG. Previously, feasibility of glass blown spherical shell as the atomic vapor cell was demonstrated [34]. A folded Helmholtz coil design was proposed and micro heaters were fabricated.

In this thesis, design, analysis, modeling, fabrication, and characterization of individual components required for NMRG are described in detail. Analytical modeling for uniformity of magnetic fields produced by Helmholtz coils is presented. The effect of two different micro heater designs on magnetic field is also examined. A novel design of a double-folded structure to assemble all the individual components is provided along with design of magnetic shields. Details about table-top setup for characterization of atomic vapor cells are discussed. Several experiments related to detection of Xe are illustrated.

## 1.5 Thesis Outline

Chapter 2 explains briefly the dynamics behind NMRG. Keeping miniaturization as the main goal, the integrated Rb magnetometer and corresponding detection schemes are discussed. Chapter 3 explains the technical design approach and addresses each individual component with its own sections of design, fabrication, and characterization results. Design details of micro Helmholtz coils, micro heaters, and micro vapor cell are provided. Size optimization approach for the folded structure is explored. A comparison between dielectric mirrors and fabricated metallic mirrors is provided in terms of reflectivity and polarization changes. Results on analytical and FEM modeling of magnetic shields are reported. Chapter 4 is dedicated to the establishing the required experimental setup, the challenges faced and ultimately the experiments related to Xe. Experimental setup for operation of a Rb magnetometer are described. The issues with a DC heater are identified and usage of AC heating to detect Xe is explained. A set of experiments leading to Xe relaxation time measurements are also provided. Chapter 5 concludes the thesis with directions for future work and some of the latest results done in collaboration with the current students.

# Chapter 2

## Basics of NMRG

The basic principle of NMRG is to measure the precession frequency of the observed atomic species under applied magnetic field. If the frame of reference starts rotating, then the observed frequency is shifted accordingly, thus the rotation can be detected.

### 2.1 NMRG - Theory of Operation

Every atom contains positively charged nucleus and negatively charged electrons. Each has an inherent property called spin of nucleus and spin of electron. Associated with each spin is a magnetic moment due to the angular momentum and the relation is given by,

$$\bar{M} = \gamma \bar{I} \tag{2.1}$$

where  $\gamma$  = Gyromagnetic ratio , M = Magnetic moment, I = Angular momentum.

Though electron spin can also be considered, we deal only with nuclear spin in this project.

When placed in a magnetic field, the torque due to the applied field will attempt to change the magnetic moment.

$$\frac{dI}{dt} = \bar{M} \times \bar{B} \quad (2.2)$$

Hence the magnetic moments start precessing around the applied magnetic field. At a given time, all the nucleus would be randomly oriented but would still be precessing around the applied field. Combining the above two equations, we can write

$$\frac{d\bar{M}}{dt} = \bar{M} \times \gamma\bar{B} \quad (2.3)$$

where,  $\omega_0 = \gamma B$  is called the precession frequency or the Larmor frequency of the nucleus,  $\gamma$  is gyromagnetic ratio of the nuclei. If the frame of reference is rotating with  $\omega_R$ , then the detected precession frequency would be  $\omega = \gamma B - \omega_R$ . We know the applied field  $B$  and  $\gamma$  is the constant, hence  $\omega_R$  can be detected. This is the main principle behind NMRG. In this thesis we would be considering Xe as our nuclei of interest.

This concept is also used in the bulky Magnetic Resonance Imaging (MRI) scanners. The applied magnetic field is very huge (20T - 40T) in order to polarize the nuclei, and get very high precession frequencies (in MHz range) that can be easily detected using induction coils. In order to miniaturize such a system, the luxury of huge magnetic fields is difficult to afford. Instead, we depend on several interdependent Physics phenomenon to polarize the Xe nuclei and also to detect the rotation rate.

We use a technique called spin exchange optical pumping (SEOP) to increase the number of polarized nuclei. This was developed by Alfred Kastler in 1950 and is the basic principle used in most miniaturization attempts of atomic gyroscopes.

## 2.2 Optical Pumping

In thermal equilibrium state, there are very few nuclei that are polarized and the few that are, would be randomly oriented with almost equal orientations of parallel and anti-parallel magnetic moments resulting in an almost zero net magnetic moment. To increase the net magnetic moment, the nuclei need to be polarized.

Consider a vapor cell with Xe along with alkali metal, like Rb atoms. Instead of directly polarizing the Xe nuclei, we can polarize Rb that would later transfer polarization through collisions to Xe. The process of polarizing Rb atoms using optical means is the basis for optical pumping and is used to increase the magnetization along one direction.

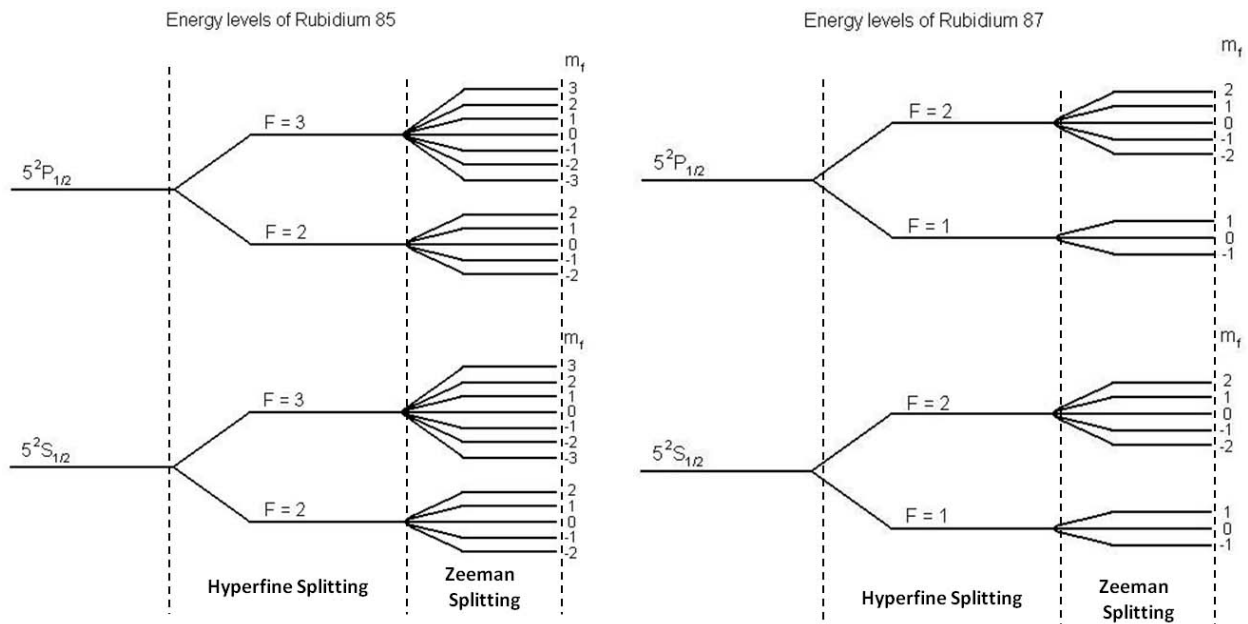


Figure 2.1: The Zeeman splitting of  $\text{Rb}^{85}$  (left) and  $\text{Rb}^{87}$  (right) (reproduced from [36] )

Rb atoms at certain temperature and in the presence of magnetic field undergo Zeeman splitting of their energy states (Figure 2.1). If a circular polarized light of certain wavelength is incident on this sample, only certain atomic transitions are allowed and after certain time, the atoms end up with a configuration such that it cannot absorb any more light. This is called optical pumping of Rb and thus results in magnetization in a certain direction, parallel

to the applied field [35].

After applying a steady magnetic field and causing the Zeeman splitting in Rb, it is very crucial for the pumping light to be circularly polarized to allow only certain atomic transitions [37]. Improperly polarized light may not result in optical pumping. With the use of circular polarized light, all the Rb atoms can be polarized along the direction of the pump beam. Reversing the circular polarization of light (from left to right or vice versa) or even flipping the magnetic field, would cause the Rb atoms polarization to flip directions.

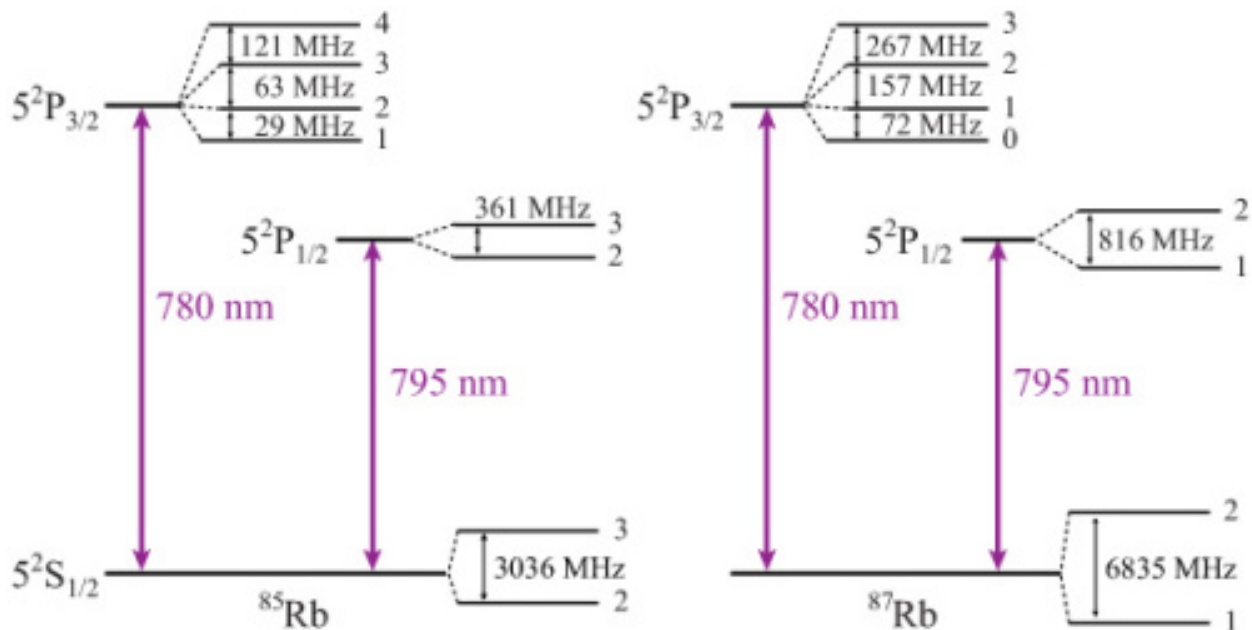


Figure 2.2: The hyperfine levels in the  $\text{Rb}^{85}$  (left) and  $\text{Rb}^{87}$  (right) involved in the D1 and D2 transitions, labeled with their F values (reproduced from [38] )

Naturally occurring Rb has two isotopes,  $\text{Rb}^{87}$  and  $\text{Rb}^{85}$ . Some of the vapor cells can be enhanced to contain only one isotope. Both have slightly different gyromagnetic ratios.

There are two possible transitions based on the atomic structure of Rb (Figure 2.2). They are called the D1 line at 795 nm and D2 line at 780 nm [39, 40]. Optical pumping can be achieved with either of these wavelengths. In this work, we would use 795 nm as our laser source.

For optical pumping to occur, Rb needs to be in a vapor state. Rb vaporises at around 40°C. The higher the temperature, the more Rb in vapor state (Rb Number Density) and thus more polarized Rb. For a miniaturized cell, it is imperative to operate at very high temperatures to significantly increase the Rb number density. Thus temperature plays a crucial role in operation of NMRG.

Rb atoms lose their polarization very quickly due to internal collisions. Hence the pumping laser power needs to be high enough to keep pumping rate of Rb faster than the decay to maintain a net Rb polarization [35]. A more detailed review on this topic is presented in [41].

## 2.3 Spin Exchange

Theoretically, only a sample of Rb can be used for NMRG but because the gyromagnetic ratio of Rb is very high, a small change in magnetic field causes a huge change in Larmor precession frequency. Hence Xe is considered as the sensing sample which has gyromagnetic ratio that is 3 orders less than that of Rb. Moreover the relaxation time of Rb is too small compared to Xe.

The net polarization developed by optical pumping of Rb is transferred to Xe through a process called spin exchange [42]. The Rb atoms lose their polarization but are optically pumped again (Figure 2.3). After enough time Xe atoms will have acquired net magnetization and start precessing around the applied magnetic field at their own Larmor frequency.

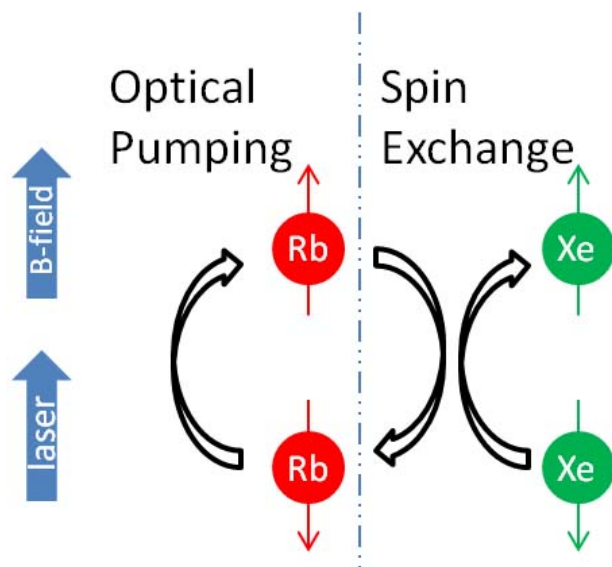


Figure 2.3: Rb-Xe spin exchange optical pumping

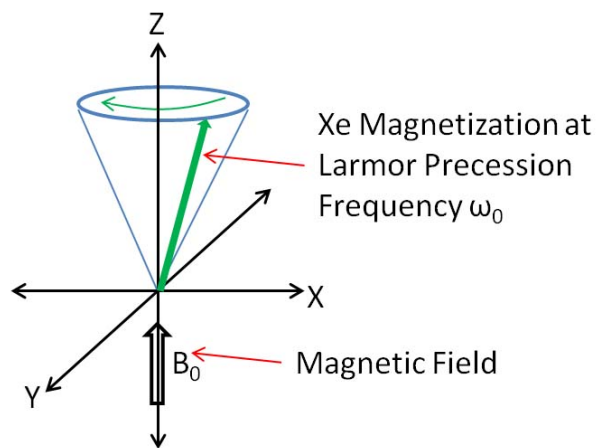


Figure 2.4: Xe Larmor precession frequency

## 2.4 Xe Magnetization

After SEOP, we have a net magnetization vector due to Xe precession around the direction of applied field ( $B_0$ ) at the Larmor precession frequency  $\omega_0 = \gamma B_0$ , where  $\gamma$  is the gyromagnetic ratio of Xe. The Xe precession is shown in Figure 2.4. If a perpendicular magnetic field at the same frequency  $\omega_a = \omega_0$  (hence the name, nuclear magnetic resonance) as Xe precession is applied, it pushes the Xe magnetization into the perpendicular XY plane. Based on the duration and amplitude of the orthogonal field, the Xe magnetization may be flipped  $90^\circ$  or  $180^\circ$ .

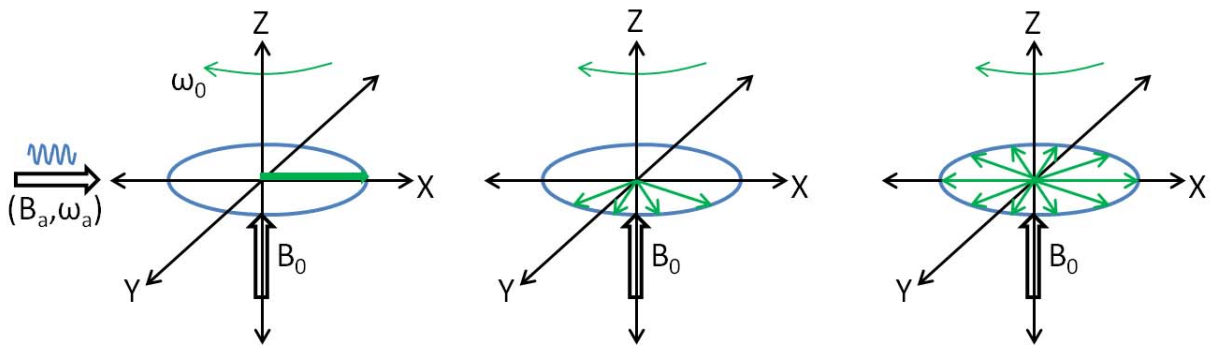


Figure 2.5: Spin-Spin relaxation time

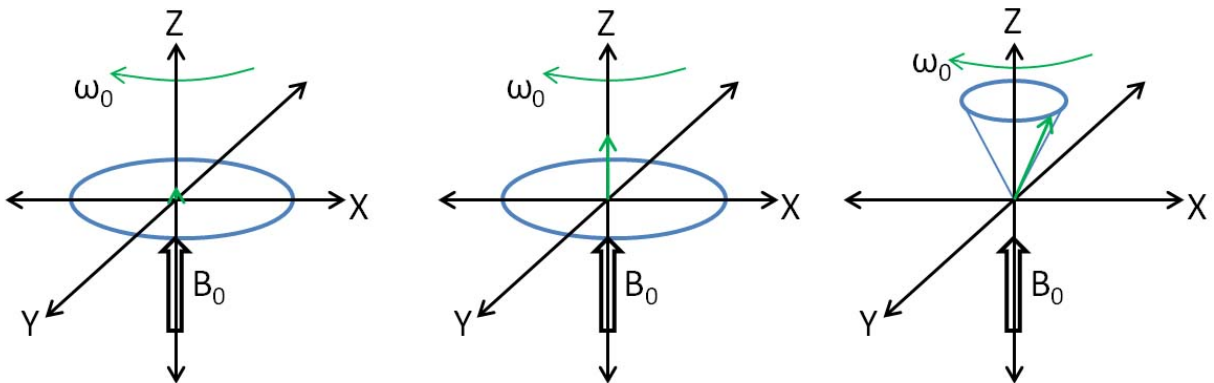


Figure 2.6: Spin-Lattice relaxation time

Observing the precession frequency of the flipped Xe magnetization, the rotation rate of the system can be measured. This signal is maximized when Xe is flipped at  $90^\circ$ . If the

orthogonal field is removed, the Xe component along the perpendicular direction becomes zero with some time constant(Figure 2.5). This relaxation is termed as Spin-Spin relaxation time or  $T_2$  [43, 44].

After it is flipped to XY plane, the Xe polarization grows back to being aligned along the Z direction (Figure 2.6). This time constant is known as Spin-Lattice relaxation time or  $T_1$ . These are two very important parameters required to evaluate the gyroscope performance. More specifically, we need to have higher  $T_2$  for more accurate measurements. In most practical cases,  $T_1$  would always be greater than  $T_2$ .

This entire dynamics can be represented using Bloch equations which relates rate of change of magnetization to the applied magnetic field. This gives us an analytical model to describe the gas dynamics.

For a typical MRI system, huge induction coils are used to detect the nuclei precession. In a micro NMRG implementation, the signal generated by these nuclei is very small and would be hard to pickup using induction coils. So we use the inherent Rb atoms in the cell to detect the magnetization changes of Xe as described in the next section.

One of the most important consideration for designing NMRG is the spatial homogeneity of the magnetic field. Having a non uniform field would result in different nuclei precessing at different Larmor frequencies. This results in a spread of frequencies and can be related to the relaxation time  $T_2$  [35].

$$T_2 = \frac{1}{(\pi\gamma\Delta B)} \quad (2.4)$$

In order to increase  $T_2$ , a highly uniform field is required.This is a crucial design parameter.

## 2.5 Rb Magnetometer

Using the Rb atoms to detect the Xe precession totally eliminates the need for another detection system all together. Instead of having only a pump beam for SEOP, introducing an orthogonal beam can be used to detect the Xe precession by observing Rb atoms.

The Rb atoms undergo precession at their own Larmor frequency which is at least three orders of magnitude higher than Xe. With just pump magnetic field, they rotate around that axis at  $\omega_c$ . If there is Xe rotating at a different frequency  $\omega_a$ , the Rb would start to get modulated by that frequency. Probing the Rb atoms from the perpendicular direction would give a signal that is modulated at  $\omega_c$  and  $\omega_a$ . Demodulating this twice would give us the rotation rate of the system. Most of the derivation is presented in [35] and [45] on the Rb Magnetometer. Two different detection mechanisms [46] are prevalent based on the kind of probe light used.

### 2.5.1 Dehmelt Detection

If the similar circularly polarized light as the pump beam is used for detection, it is called the Dehmelt technique [47]. The photodetector voltage would be modulated at  $\omega_c$  and  $\omega_a$ , and double demodulation at appropriate frequencies would give the rotation rate of Xe [48, 49]. The disadvantage is that there could be a competition between the probe and pump beams to dominate the pumping process. Hence the probe beam has to be kept at a lower power which then might affect the SNR. The advantage is that only a single laser source can be used for both pumping and probing by careful routing of optical beams.

## 2.5.2 Faraday Detection

In Faraday detection, a linearly polarized beam is made to interact with the Rb atoms. Based on the amount of magnetic field due to Xe precession, the linear polarized light would rotate after passing through the cell. At the detector if the beam is passed through a polarizing beam splitter, the double demodulation of the difference of these two split signals would give the rotation rate.

Though this uses more components, it gives a better SNR as the pump and probe are not competing with each other. Also, the detection is not highly dependent on the probe power as the detection is based on the rotation of the linear polarization angle [50, 51, 61].

SNR improvements in both Dehmelt and Faraday methods can be made by operating the probe beam at the 780 nm instead of 795 nm to eliminate any interference.

# Chapter 3

## Design Approach

The whole concept of folded NMRG is described in the assembly flow diagram shown in Figure 3.1. It is to be noted that this process is compatible with batch fabrication and requires minimal assembly. Thus an atomic gyroscope can be implemented with the advantages of MEMS fabrication methods. Each of the steps in the Figure 3.1 are given below. Each individual component required for the complete NMRG will be discussed in detail in the following sections.

1. Batch fabrication of folded pyramid and Helmholtz coil structures with thru-wafer vias.
2. Assembling both folded structures together such that the vias align.
3. Assembling heaters and vapor cell accordingly, inside the folded structures.
4. Folding the Helmholtz coils.
5. Assembling the optical components on side walls of folded pyramid structure.
6. Complete structure after folding the pyramid structure.
7. Magnetic shielding of the whole assembly.

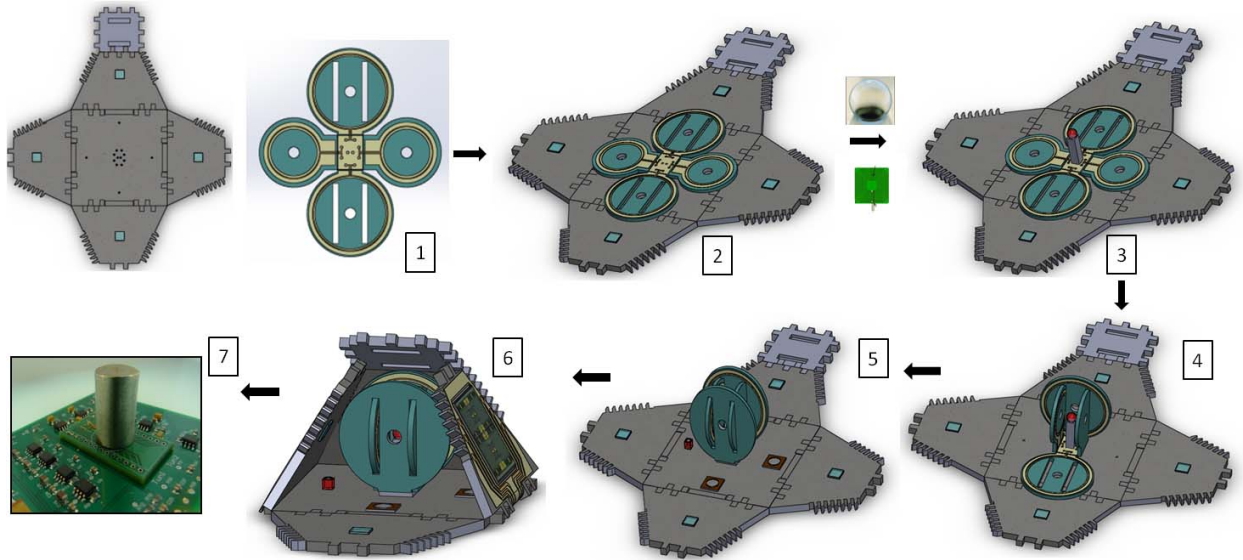


Figure 3.1: Assembly flow of folded NMRG

### 3.1 Coils

One of the important criteria for operation of Rb magnetometer is uniformity of magnetic field. As the approach is to miniaturize the whole sensor, the Helmholtz coils are first design choice to produce magnetic field. Helmholtz coils are a pair of coils separated by a distance equal to the radius of the coils. This configuration generates uniform magnetic field at the geometric center.

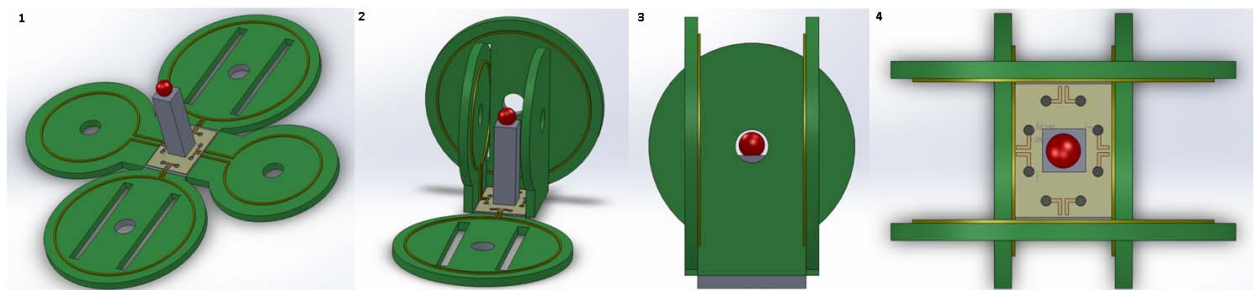


Figure 3.2: (1) Unfolded structure with vapor cell (2) Semi-folded (3) Side view of completely folded assembly (4) Top view

The atomic vapor cell would be a spherical glass blown cell which would be filled with the required gases (Rb, Xe and buffer gas). Previously at UCI, successful fabrication of

spherical cells with a diameter of around 1 mm was demonstrated [53]. The conceptual sketch of foldable Helmholtz coils and glass blown vapor cell is shown above in Figure 3.2. The folded coils can be batch fabricated using polyimide as the foldable hinge. Similar folded structures have been demonstrated earlier at UCI.

### 3.1.1 Design

The most important criteria for Helmholtz coil design is the radius of the coils which determines both the size of the coils and also the homogeneity. The schematic shown in Figure 3.3 is the configuration used for analysis.

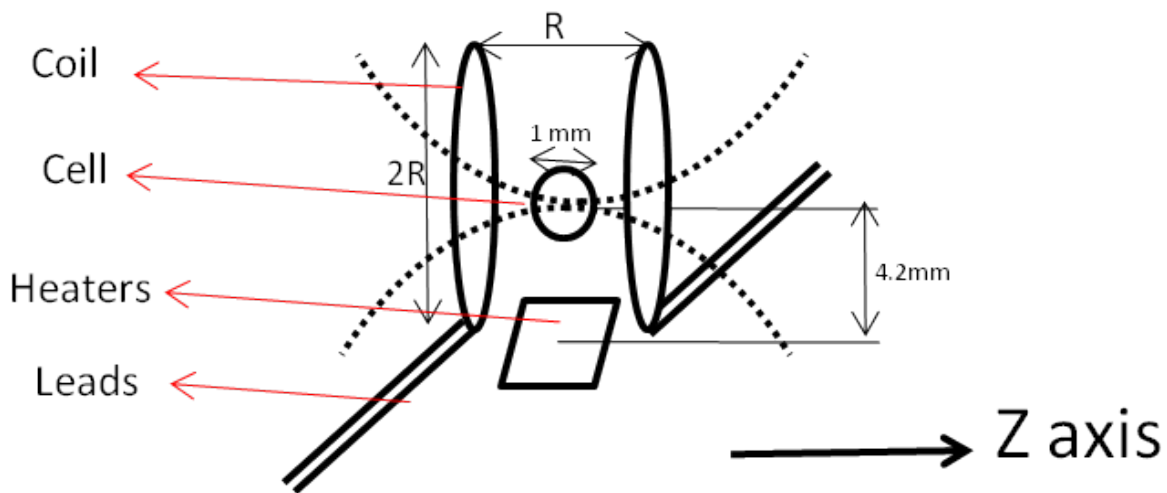


Figure 3.3: Coil configuration

Magnetic field due to a current ( $I$ ) carrying loop (radius  $R$ ,  $N$  loops)  $B = \frac{\mu NI}{2R}$

Magnetic field at a distance  $z$  along the axis,  $B = \frac{\mu NI R^2}{(2(z^2 + R^2))^{3/2}}$

Magnetic field due to a pair of Helmholtz coils, arranged such that distance between them

is R,

$$B = \frac{\mu N I R^2}{(2((z - \frac{R}{2})^2 + R^2)^{3/2})} + \frac{\mu N I R^2}{(2((z + \frac{R}{2})^2 + R^2)^{3/2})} \quad (3.1)$$

Homogeneity is defined as  $H = \frac{\Delta B}{B_0} \times 1e6$  ppm, where  $B_0$  is the field at the center of the Helmholtz coils. Homogeneity is calculated along the z axis at the center of the coils. The difference of maximum and minimum magnetic field along this axis equals to  $\Delta B$  around the 1 mm diameter corresponding to the cell size. Hence homogeneity is calculated.

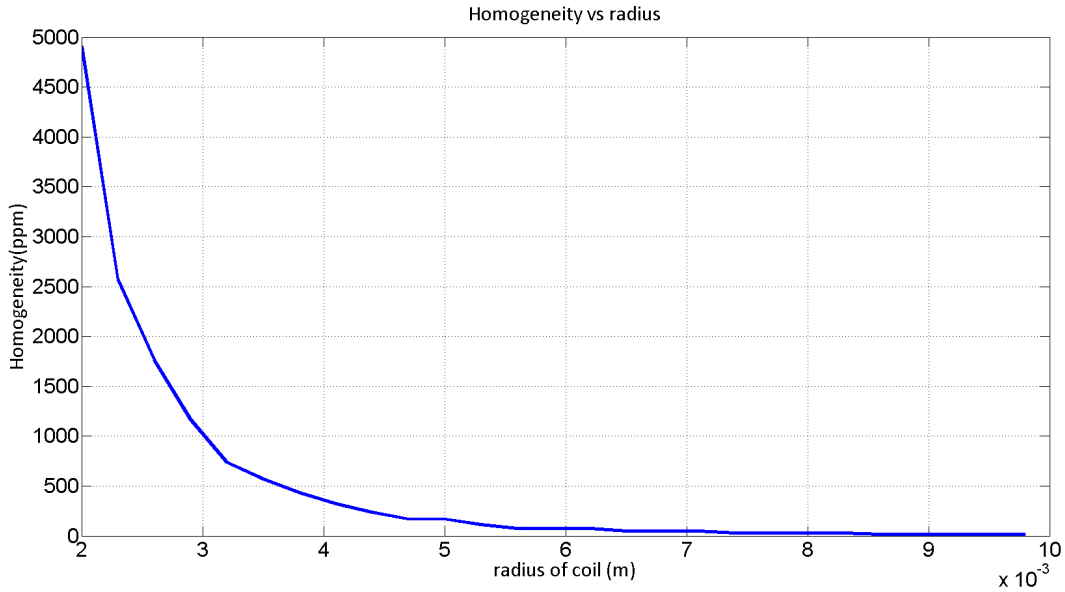


Figure 3.4: Homogeneity vs radius of coils

Figure 3.4 shows the variation of homogeneity as a function of radius. It can be seen that increasing the radius above 5 mm does not significantly improve the homogeneity but does increase the total volume of the coils. Hence a design choice of 4.2 mm is made for the coils.

The parameters for analysis are, radius of coil = 4.2 mm, current in coil = 60 mA, height of cell from heater = 4.2 mm, leads length  $\approx$  10 mm, distance between leads  $\approx$  0.3 mm.

As discussed in previous chapters, homogeneity affects the relaxation time directly.  $T_2 =$

$$1/(\pi\gamma\Delta B), \gamma= 1e7; \implies \Delta B = 30 \text{ nT}, H = 3000 \text{ ppm for } T_2 =1;$$

For the radius of choice and the lead configuration as shown in Figure 3.3, the homogeneity was calculated as  $\approx 827$  ppm at the center.

It is assumed that the heaters will be placed below the cell or on the base and there would be a thermally conductive pedestal which is non-magnetic, like Si or Aluminum on which the cell will be placed as shown in Figure 3.1. The heaters are required to increase the cell temperature such that the Rb inside the cell is properly vaporized. Two designs for heater are considered, Octapole design, where the pattern of conductors is  $+-+--+$ , where as the Dipole design has the pattern  $+--+--+$  for the same number of conductors. More details are in this [52]. Using these, the homogeneity was evaluated taking into account the spurious fields generated by heaters placed at 4.2 mm below the cell on the base of Helmholtz coil, and shown in Figure 3.5.

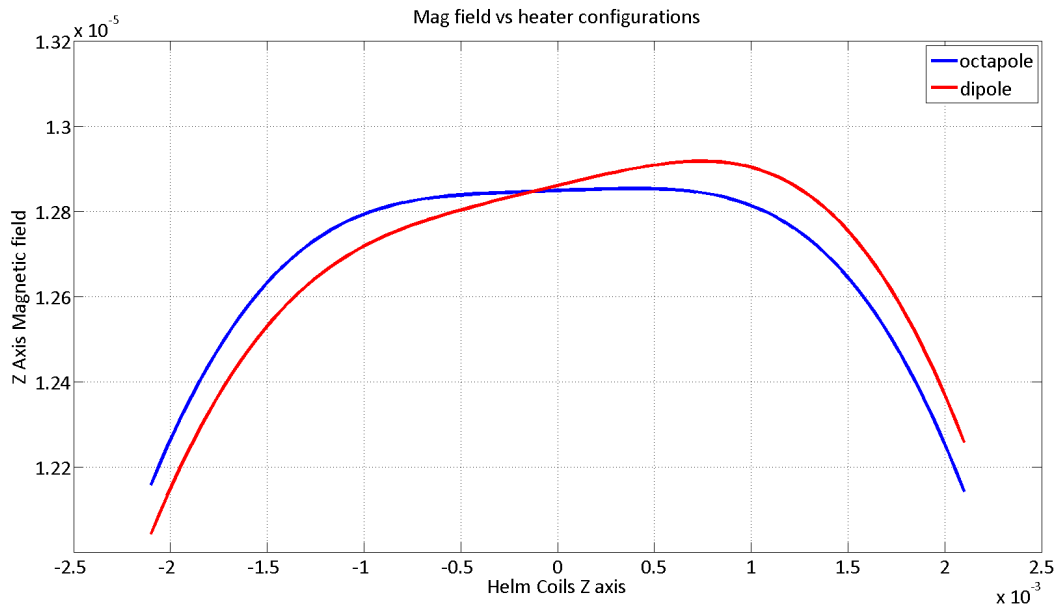


Figure 3.5: Homogeneity for Dipole and Octapole heaters

The homogeneity values are tabulated for each of the different configurations in Table 3.1.

This clearly shows the advantage of using an Octapole heater over a Dipole heater for

Condition	Homogeneity
Coils only	235ppm
Coils + leads	827ppm
Coils + leads + dipole heater	8285ppm
Coils + leads + Octapole heater	1165ppm

Table 3.1: Homogeneities for different conditions with Helmholtz coils

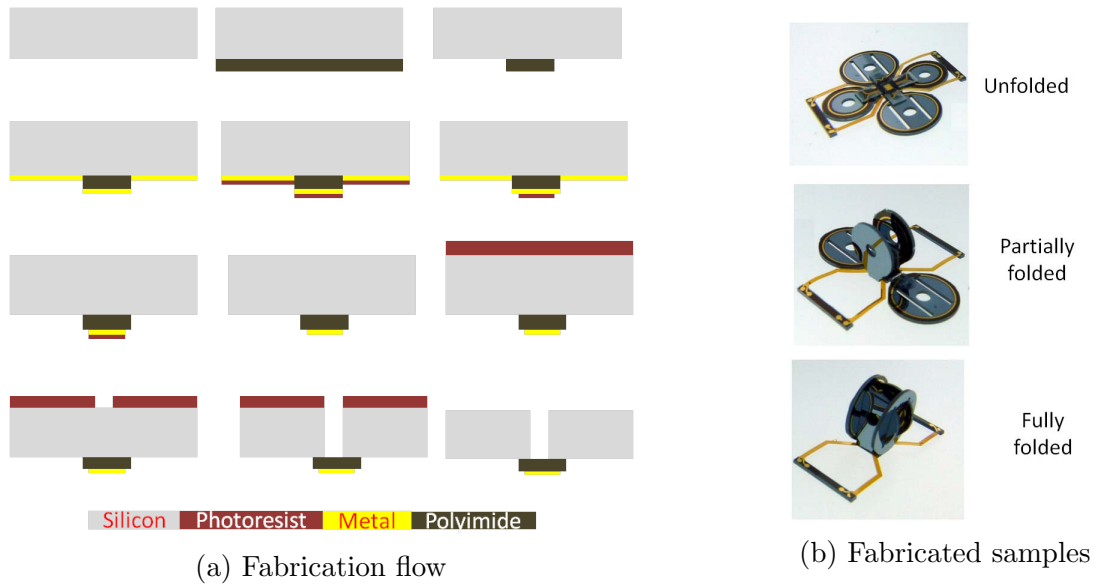


Figure 3.6: Fabrication of Helmholtz coils

homogeneity requirements.

### 3.1.2 Fabricated Samples

Folded coils were fabricated by Dr. Sergei Zotov and Dr. David Blocher at UCI. The folded samples are shown in Figure 3.6b. A similar fabrication flow is described again later in Section 3.5.3.

### 3.1.3 Characterization

One of the fabricated samples of Helmholtz coils was wire bonded for characterization. Only one smaller radius coil could be connected using the bond wire. As a bigger package was not available, two standard dip packages were arranged and a Si plate was attached using glue on top of the packages. The Helmholtz coil was gently attached on top of the Si plate with glue as shown in Figure 3.7. Wire bonding was attempted from the leads on Helmholtz coils to the package but only one connection was possible from a small coil to the package. This could be due to unclean samples, improper metal evaporation due to which bonding was not feasible. The fabricated metal traces were 5000 to 6000  $\text{\AA}$  thick and were made of Gold (Au) deposited on top of 500  $\text{\AA}$  Chromium (Cr).

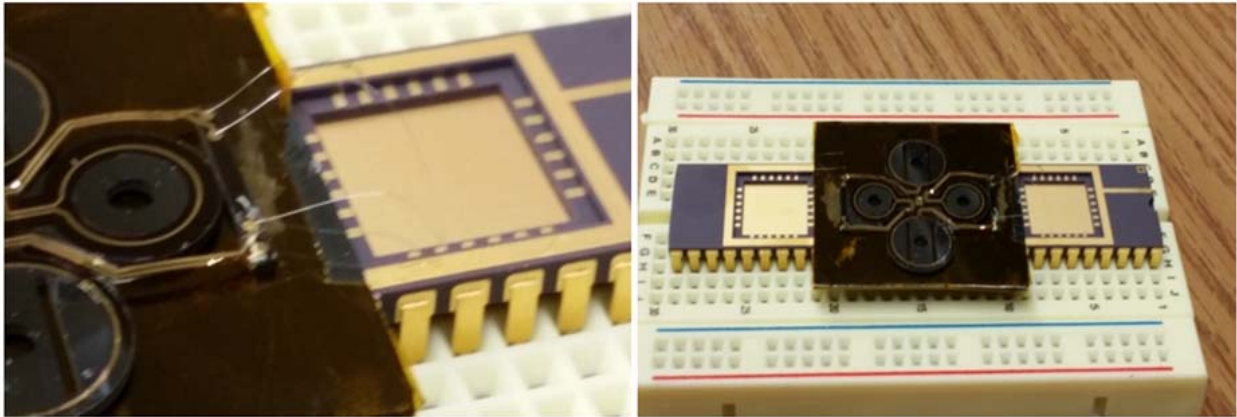


Figure 3.7: (left) Bond wire to DIP package (right) DIP package on breadboards

The connectivity was verified with a multimeter, which showed a resistance of around  $15 \Omega$  between the two connections. To get a  $10 \mu\text{T}$ , we required a current of 60 mA (from analysis as shown above). Hence connections were made from the bread board to provide a voltage of around 1V to pass a current of approx. 60 mA. A very sensitive Hall effect probe was suspended from the vertical optical ports of macro shields (Section 4.3). The height and placement of the coils was adjusted such that the probe tip is as close as possible to the coil and the tip of the probe is perpendicular. This arrangement is shown in Figure 3.8.

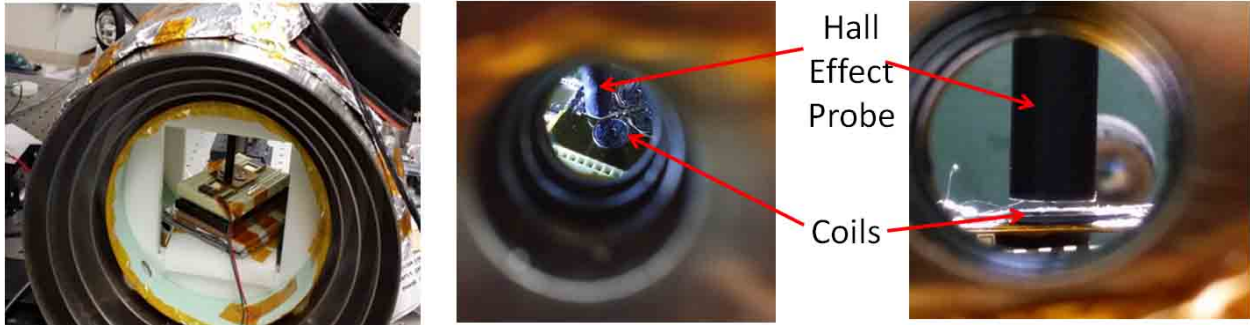


Figure 3.8: Close up of the Hall effect probe close to the single coil attached with bond wires, placed inside the magnetic shields

It was verified that after passing current, the measured magnetic field was  $8 \mu\text{T}$ , after taking into account an offset of around 3 mm on the axis and also including a 1.2 mm for the offset of sensor inside the probe tip. The measured value is very close to the expected value of  $10 \mu\text{T}$ . The possible reasons for the slight discrepancy could be due to contact resistance current loss, static field from breadboards causing improper magnetic field measurement or wrong estimate of the sensor tip distance from the center of coil.

## 3.2 Heaters

Two different designs for the micro heater were considered. A Dipole heater with pattern of conductors arranged as  $+-+--+$  and Octapole heater where the pattern of conductors is  $+-+--+$  which gives significantly better cancellation, as modeled earlier. The design is based on this patent [52]. These samples were designed/fabricated by Dr. David Blocher at UCI. The design of the heaters and fabrication flow of Octapole heater is shown here for reference in Figure 3.9. The footprint of the heaters is around (2.6 X 2.6) mm.

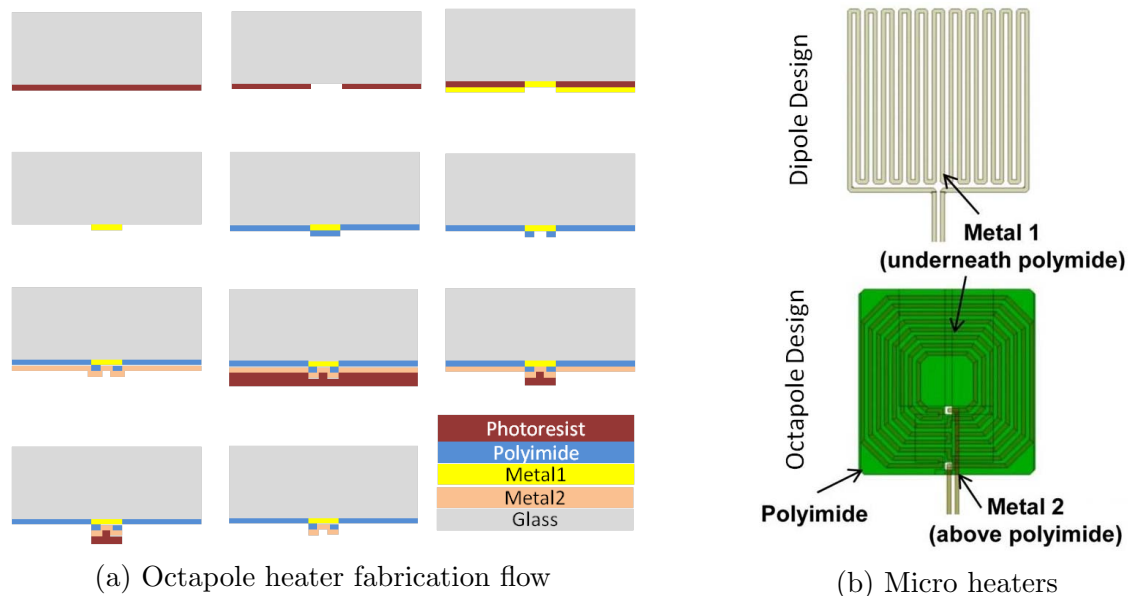


Figure 3.9: Micro heaters

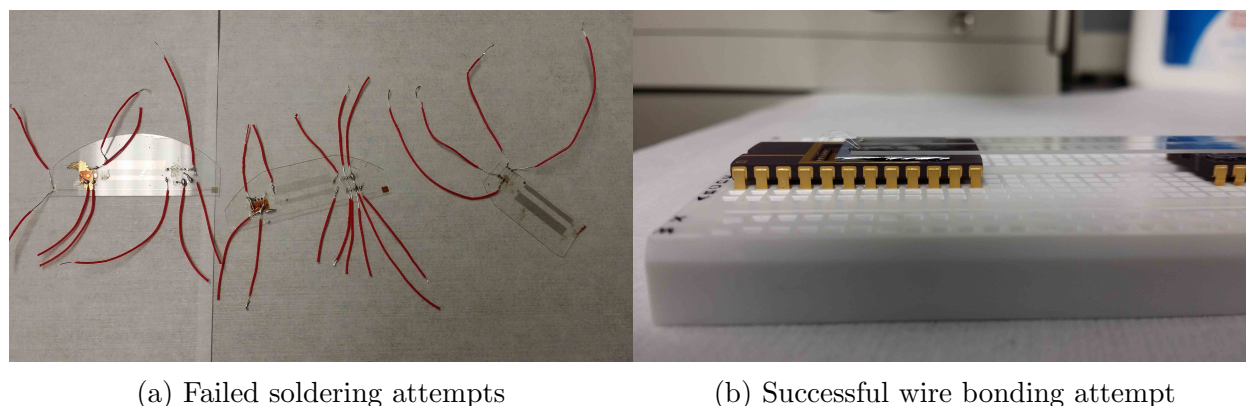
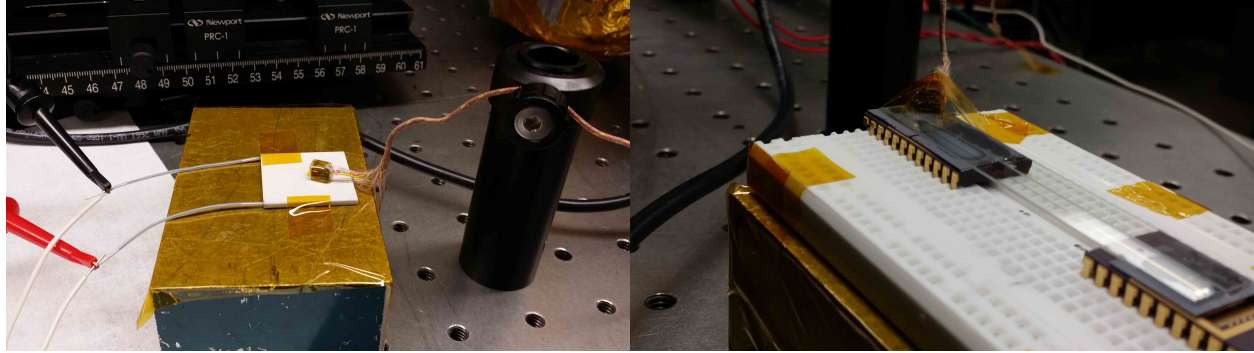


Figure 3.10: Electrical connection to heaters

### 3.2.1 Characterization

The samples were diced, and to characterize the heaters, initially soldering was attempted onto the electrodes on the glass wafers. But after several futile attempts (Figure 3.10a), wire bonding was attempted which resulted in a good connection. The two heaters were assembled on top of standard DIP packages and the wire bonding was done as shown in Figure 3.10b. The immediate test was to check the resistance of the two heaters. Dipole heater measured  $\approx 350 \Omega$  and the Octapole measured around  $210 \Omega$ .



(a) Ceramic heater

(b) Micro heaters

Figure 3.11: Si pedestal with temp sensor on (left) Ceramic heater (right) Fabricated heaters

A small stack of Si wafer pieces was assembled to mimic the pedestal on top of which the vapor cell would be placed for elevation. This stack was placed on conventional ceramic heaters and assembled with a thermal sensor on top of the stack to record temperature. The same experiment was repeated with the fabricated heaters, with the almost the same input power. The setup is shown in Figure 3.11. The ceramic heater setup reached a temperature of  $55^{\circ}\text{C}$  in 10 minute with input power of 1.5 W. The fabricated heaters reached  $45^{\circ}\text{C}$  in 8 minute with input power of 1 W. This shows that the heaters are comparable to the commercial heaters.

One fabricated sample from each of the designs was heated till it was burned out to find the maximum power limitation of the heaters. The power rating of Dipole heater was found to be 3.3 W and Octapole heater was around 4.2 W.

### 3.2.2 Magnetic Field from Heaters

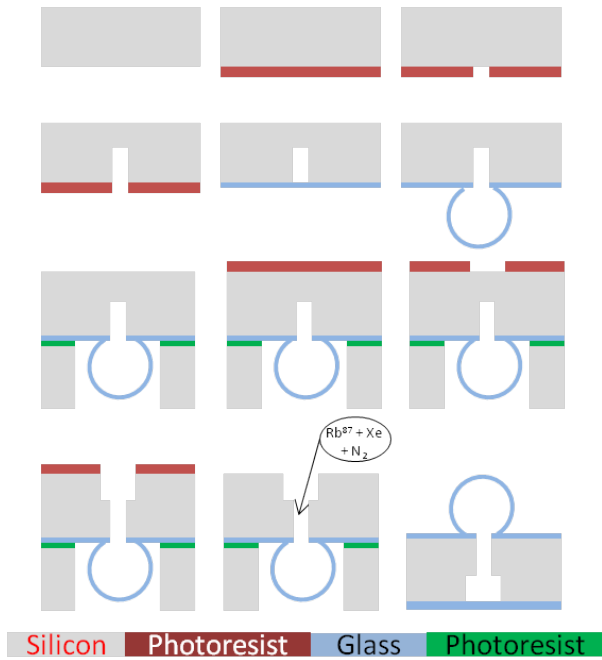
Later this assembly was put inside the shields to measure the magnetic field. But based on the current values (60 mA), the field produced by the heaters was in the nT region. The Hall effect meter was only sensitive to  $0.1 \mu\text{T}$  and hence no discernible measurements could be made.

## 3.3 Vapor Cell

The concept of using spherical glass blown cells for NMRG was demonstrated in [53]. The idea is to trap small volume of air at room temperature and when put at a high temperature, the air expands and pushes the glass boundary outwards. Glass starts to soften due to change in viscosity at around 800°C. Etching deep cavities in Si wafer and sealing the wafer with glass can create volume of trapped air, which when heated can result in very symmetrical glass blown structures. The important parameters to play with are the radius of the cavity opening and the height of the cavity used for glass glowing. Based on the modeling presented in [35], the radius of the opening and height of the cavity were selected as being 250  $\mu\text{m}$  and 750  $\mu\text{m}$  respectively.

### 3.3.1 Fabrication

The fabrication flow of glass blown cells is in Figure 3.12a. A double-side polished 1 mm Si wafer is first patterned with photoresist and circular openings of required radius are patterned. Using DRIE and constant monitoring of etch depth, cavities with a height of approx. 750  $\mu\text{m}$  are created in the Si wafer. The photoresist is stripped off and a 200  $\mu\text{m}$  thick glass wafer is anodically bonded on the top of etched Si wafer. This wafer is now put in a furnace at about 800°C for 2 to 3 minutes to create the glass blown shells. Carefully inverting the shell, the backside of the wafer is patterned to open up the earlier sealed chamber as shown in the fabrication flow. Once the backside is open, the required gas mixture along with Rb can be filled inside the shells. The backside can now be anodically bonded to create the glass blown vapor cells that can be used for NMRG. The gas filling and sealing the device was done at NIST with required gas composition. The samples are shown in Figure 3.12b.



(a) Fabrication flow for glass blown vapor cells



(b) Fabricated and gas filled vapor cells

Figure 3.12: Micro vapor cell

### 3.3.2 Characterization

The standard test of Rb absorption was done to verify that the gas filling was successful. The Figure 3.13 shows the hyper-fine splitting of Rb atomic structure and shows the two dips separated by  $\approx 7$  GHz. The theoretical separation is around 6.8 GHz [40, 39].

## 3.4 Folded Structure

A folded structure design is required to assemble all the individual components together. Developing sensors on the side walls of these folded structures [54] is a great strategy to develop a complete IMU solution [55, 56].

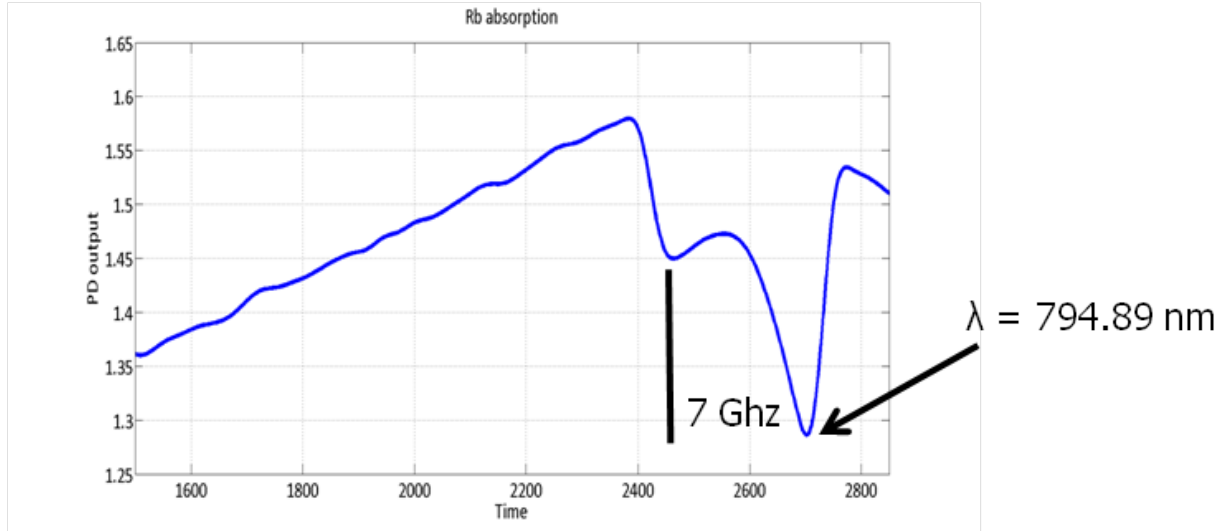


Figure 3.13: Rb absorption dip at 65°C

### 3.4.1 Design

One of the other major components in the folded NMRG is the folded pyramid structure itself. This would be used to assemble all the optical components and also act as a platform for the Helmholtz coils (as shown in Fig 3.1). Initially a very basic design was considered, where all the optical components are placed outside and the folded structures would contain just the Helmholtz coils and the reflectors. The corresponding Solidworks sketch is shown in Figure 3.14. For ease of optical access to the vapor cell, the side walls are designed at 45°. This device would be fabricated with just a two mask process, one for etching the structure itself and another for polyimide processing to keep the structures connected. The sketch is shown in Figure 3.14.

### 3.4.2 Practical Consideration for the Design

- Dielectric mirrors (from Newport Corp.)
  - Diameter  $\approx 12.7 \text{ mm} \pm 0.13 \text{ mm}$ , considered = 12.85 mm
  - Thickness  $\approx 3.1 \text{ mm} \pm 0.25 \text{ mm}$ , considered = 3.5 mm

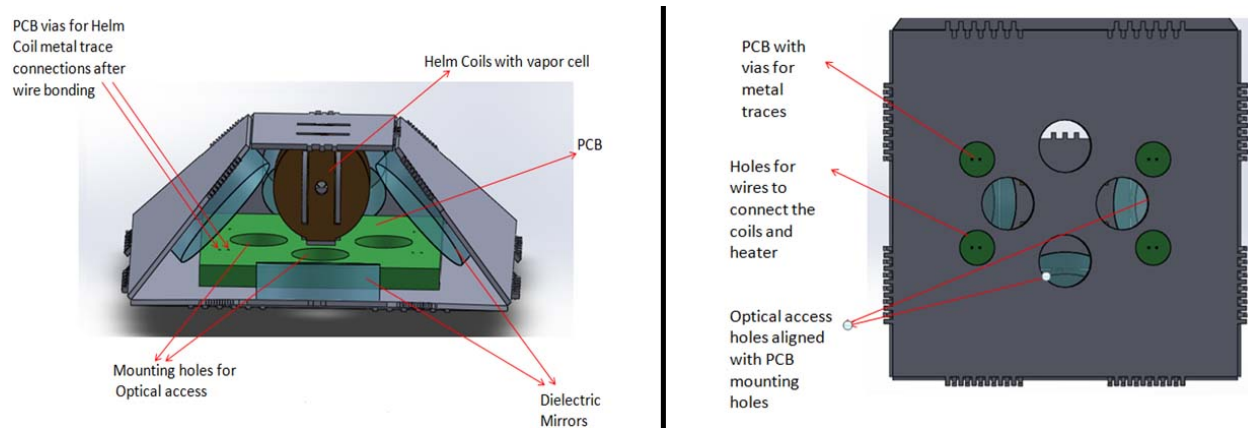


Figure 3.14: (Left) Front View: proposed design of 45° folded structure, with dielectric mirrors and assembled Helmholtz coils (Right) Bottom view: showing optical ports and access for wires to PCB

- Custom PCB to be designed for the metal traces connection to the Helmholtz coils and also heater.
  - Mounting holes on PCB to provide optical access (diameter = 6 mm)
  - Vias on PCB for connections (min. size = 0.2 mm, min. spacing = 0.6 mm)
  - Heating wire (from Thorlabs), will be placed touching the coils base
  - Height of PCB = 1.59 mm (standard), considered = 2 mm (extra, in case planar foldable heaters is used)
- The whole structure would be mounted on a pedestal, which would fit inside the magnetic shields.
- The dielectric mirrors will be attached to the pedestal for optical probing using the current test setup (Figure 3.15)

### 3.4.3 Optical Modeling for the Folded Structure

The optical modeling for the proposed structures was done to confirm the feasibility of such a design for experiments. Shown below in Figure 3.15 is the sketch of prototype placed on

a pedestal with dielectric mirrors properly arranged for optical access. The whole assembly would be arranged inside Magnetic shields (to reduce stray magnetic fields) that contain ports for optical access.

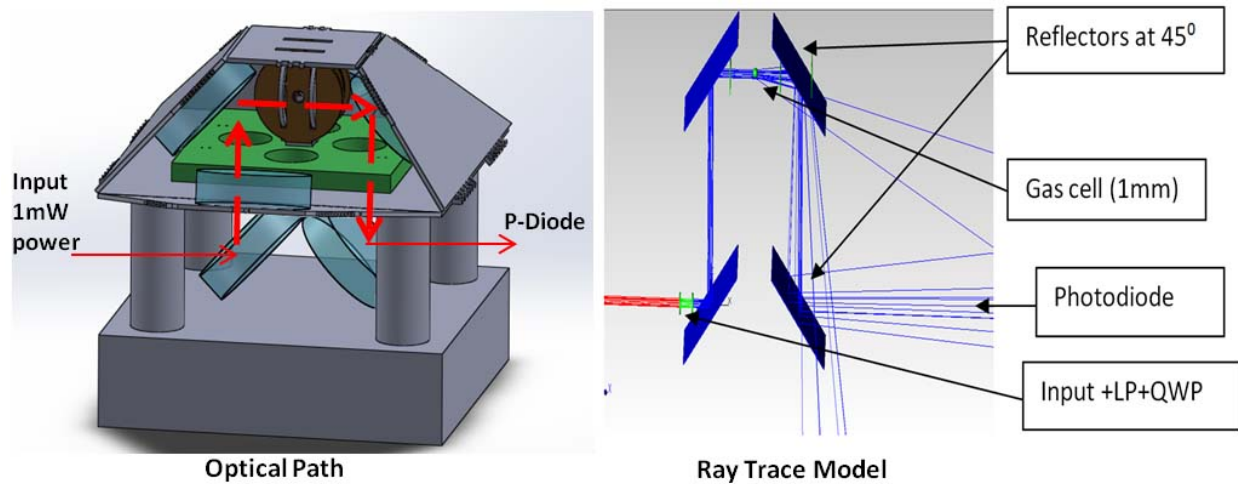


Figure 3.15: (left) Full assembly of 45° folded structures with reflectors and optical path in one axis. (Right) Ray tracing for the assembly (LP= Linear Polarizer, QWP = Quarter Wave Plate)

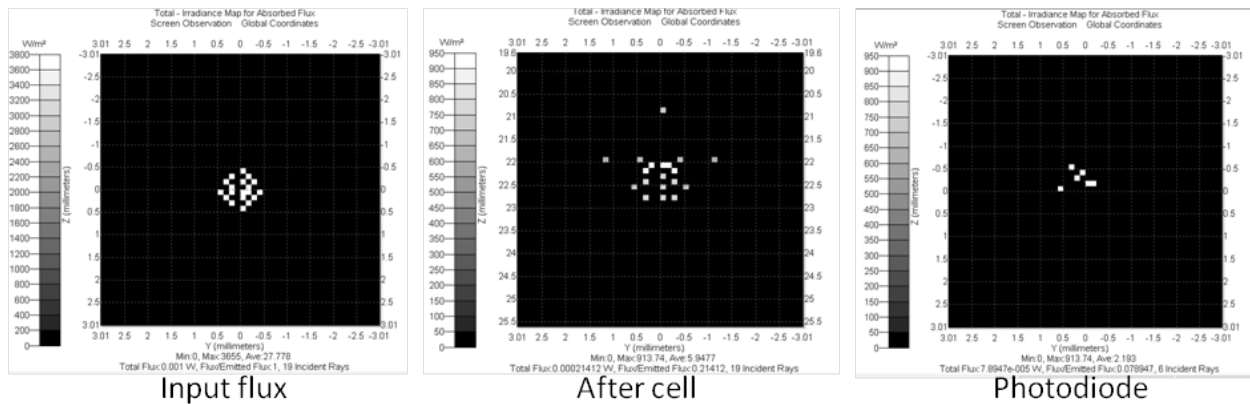


Figure 3.16: Beam profile at different locations along the optical path for flux

In the modeling it was assumed that photodetector was placed at around 30 cm from the cell, depicting the actual macro scale setup. It can be seen that the spherical glass blown cell acts like a diverging lens and the rays are scattered. After the two reflections shown, the amount of power collected at photodetector was  $\approx 78 \mu\text{W}$ , assuming input power is 1 mW, and showing that this structure is feasible to be used in the experiments. The input

power can be increased till 50 mW with a high power TOptica laser. Standard components of the shelf would be used for linear polarizer and quarter wave plate which would be placed outside the magnetic shields. In Figure 3.16, the optical flux at different locations of the optical path is shown. Similarly in Figure 3.17, the polarization of the beam is shown.

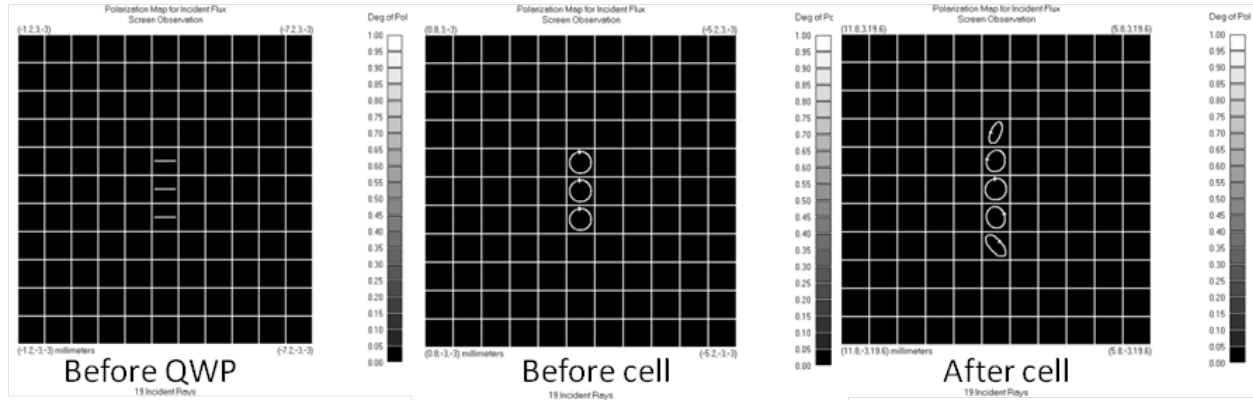


Figure 3.17: Beam profile at different locations along the optical path for polarization

### 3.4.4 Optical Characterization of Dielectric Mirrors

The dielectric mirrors from Newport Corp. were extensively characterized for effect on polarization upon reflections. The experimental setup is shown in Figure 3.18.

Different configurations for the mirror were tested along with optimization of linear polarizer and the quarter wave plate. The aim was to get a circular polarized light after the reflections from the dielectric mirrors. Thorlabs PAX equipment was used to measure the polarization of the resulting light. The results are all tabulated in Table 3.2 and the conclusions of the study are reported. The Figure 3.19 shows a sample case and how the polarization changes due to reflection from the mirror and how optimizing the setting on linear polarizer, the polarization can be recovered.

The following important conclusions are summarized below

- Each mirror changes the polarization by different amount

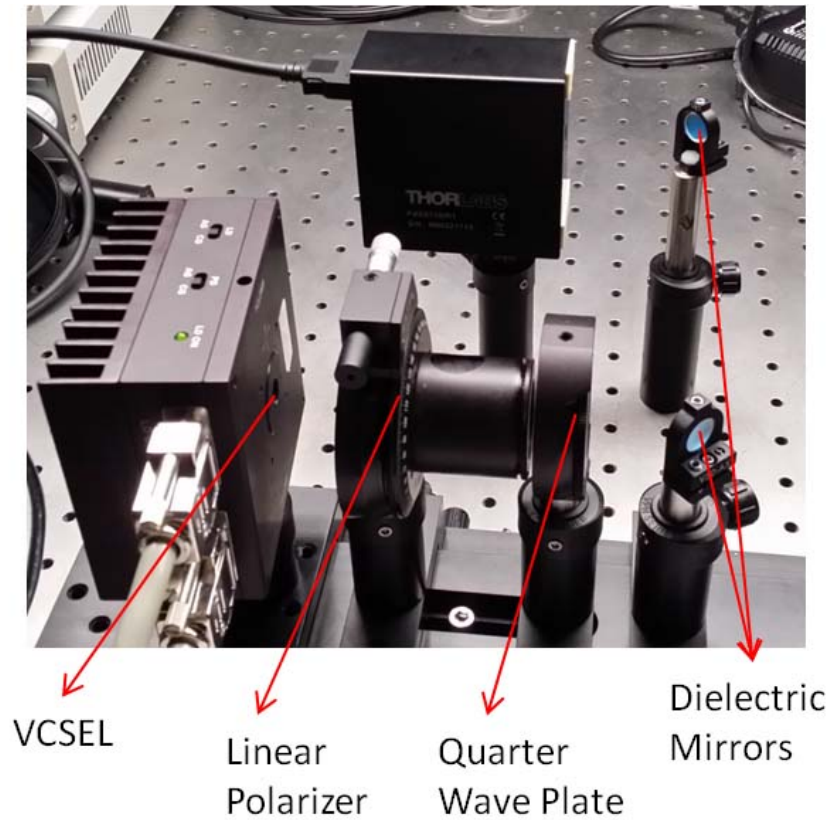


Figure 3.18: Setup for dielectric mirror characterization



Figure 3.19: Polarization changes due to dielectric mirrors

Condition	LP (deg)	QWP (deg)	Ellipticity (deg)
Only VCSEL	73	137	44.86
1 mirror (un optimized)	73	137	8
1 mirror (optimized)	108	137	44.6
2 mirror (un optimized)	73	137	-33
2 mirror (optimized)	154	137	44.39

Table 3.2: Optical characterization of dielectric mirrors

- This change can be nullified by changing just the linear polarizer angle.
- Orientation of mirrors inside the mount does not affect the optimized setting.
- Distance between the two mirrors does not change the polarization.
- Any two dielectric mirrors can be used to provide circular polarized light to the cell, after initial minimal optimization (adjusting just the linear polarizer).

### 3.4.5 Fabrication of Folded Structure

The fabrication mask for the folded structure is shown in Figure 3.20.

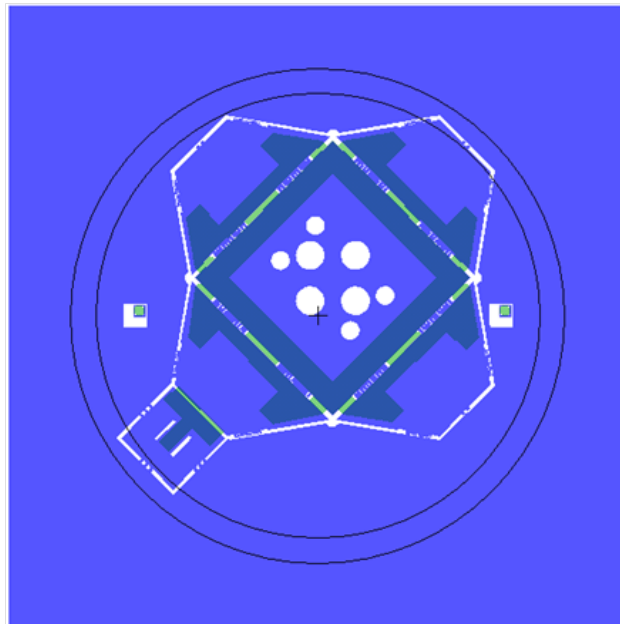


Figure 3.20: Fabrication mask for folded structure

The two mask process for fabrication involved one for polyimide processing as hinges and the other for defining the structure. After spinning polyimide on 500  $\mu\text{m}$  DSP (double side polished) Si wafer, 1st mask is used to pattern the polyimide design. After developing the sample, photoresist is spun and patterned on the backside after careful backside alignment.

Then a handle wafer is attached to the side containing the polyimide pattern with thermal grease (or dicing tape). Then backside etching is done using STS DRIE (Deep Reactive Ion Etching) through the whole wafer. Then the wafers are put in acetone to strip off thermal grease, photoresist. Ultrasonic shaker was also used to remove the residual thermal grease. Later the sample was carefully cleaned and assembled accordingly.

### 3.4.6 Assembly of Folded Structure

The micro coils, cell, were assembled first on a PCB designed according to the design described in section 3.4.1. Small Si wafer pieces were stacked to get the required elevation for the micro cell for optical access through the folded coils. The dielectric mirrors were attached using epoxy on the 4 side walls of the pyramid structure as shown in Figure 3.21. Later, careful folding of the folded pyramid resulted in the first assembled prototype of the design.

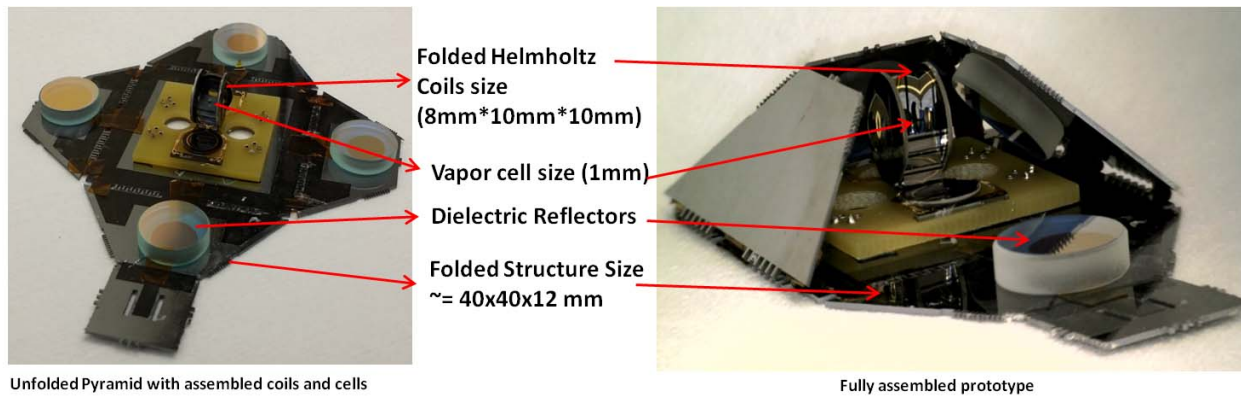


Figure 3.21: (left) Unfolded pyramid with assembled coils and cells (right) Fully assembled prototype

### 3.4.7 Optical Characterization of Folded Structure

Once the assembly was completed, optical characterization was done to check if the optical path for laser could be obtained using the folded assembly. A dielectric mirror was angled at  $45^\circ$  and placed on a pedestal over which the whole assembly was placed to mimic the design in section 3.4.3. The setup is shown in Figure 3.22. After a lot of careful alignment, of the VCSEL source, lenses, assembly, the output was detected on photo diodes confirming the light path after two reflections. The detected power was approximately  $26 \mu\text{W}$  for the input power of 1 mW. The optical modeling predicted  $78 \mu\text{W}$  of power for similar assembly.

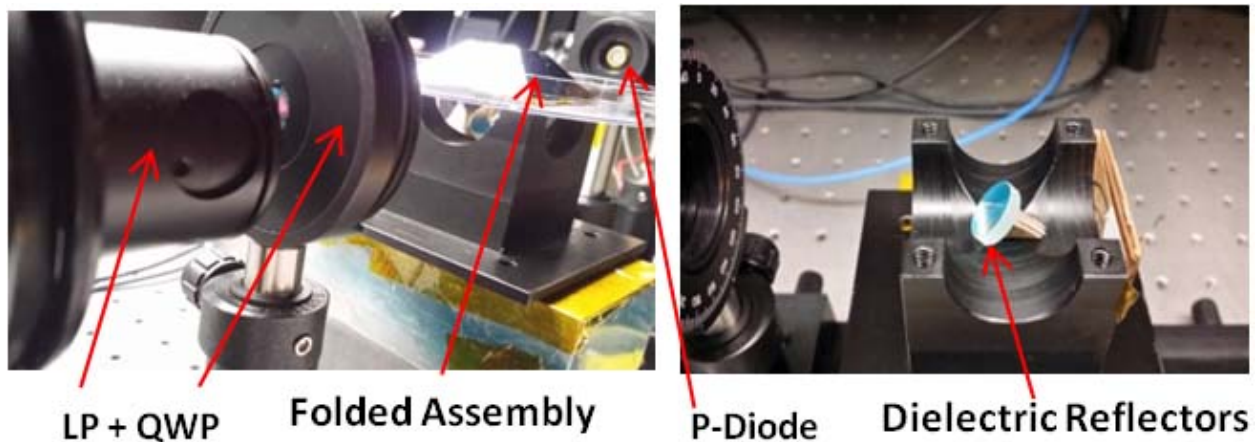


Figure 3.22: Optical testbed for folded structure

### 3.4.8 Miniaturization of Folded Prototype

The size of the assembled prototype was approx. (39.2 X 39.2 X 12) mm. The relatively larger size was constrained due to off the shelf dielectric mirrors. The dielectric mirrors have considerable thickness (at least 3 mm) due to which the side wall of the prototype ( $45^\circ$  angle wall) had to be further away from the coil assembly. This first prototype served as a crucial step in understanding the practical concerns and immediate plans to shrink the size were undertaken. The actual goal was to replace the dielectric mirrors with fabricated dielectric mirrors [57]. Another consideration was to use metallic mirrors. Metallic mirrors

have the advantage that the light maintains its polarization upon reflections. However, these mirrors could be lossy. Of the available materials, Gold was selected for its higher reflectivity (around 95 %) in the wavelengths of interest, 795 nm. However, for Gold to be deposited on Si, typically a thin layer of Chromium is used to ensure proper adhesion. Aluminum is also a strong contender for its low diamagnetic properties. In the immediate iteration, 5000 °A Gold layer deposited on top of 500 °A Chromium was selected as the reflective surface, instead of the bulky dielectric mirrors. This significantly reduced the area of the folded structures. A similar design to previous iteration with metallic mirrors was made in Solidworks to verify the concept as shown in Figure 3.23. The size shrunk from (39.2 X 39.2 X 12) mm to being just (29.2 X 29.2 X 12) mm.

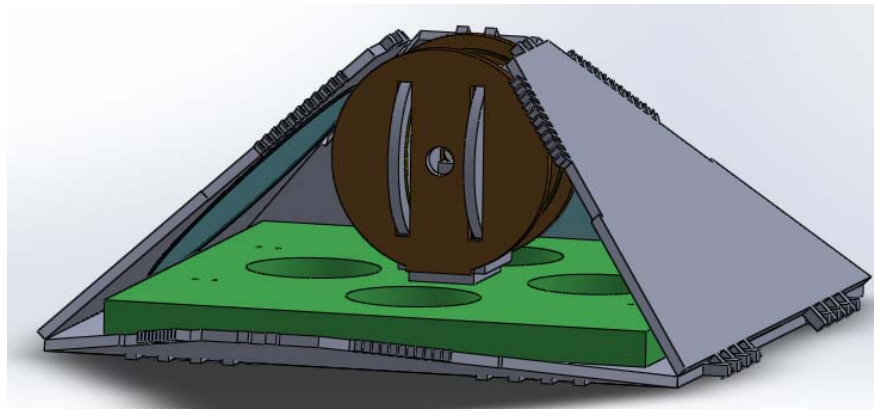


Figure 3.23: Modified folded structures with metallic mirrors

### 3.5 Novel Design for Folded Structure

While optimizing the size, a novel design approach was proposed to further reduce the size. It can be observed in Figure 3.23 that reflective surface on the side walls are required only in a specific region, where the light would be incident from the bottom plane. Most of the 45° side wall near the bottom plate is not used as reflectors. So the new design was proposed by minimizing the bottom plate of the design and still having the required reflective surfaces on the side walls. The full sketch of the design is shown in Figure 3.24.

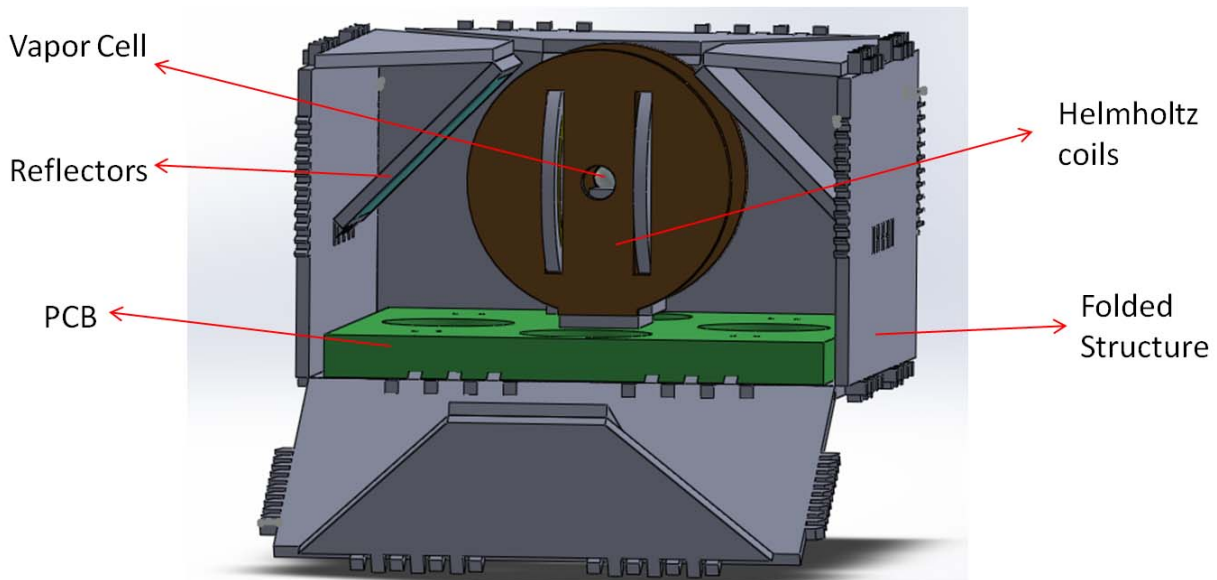


Figure 3.24: Novel design for folded structure

The reflective surfaces are provided on a much smaller surface. The Figure 3.25 shows this assembly step. The side walls when unfolded are made up of three segments, A, B, and C. Wall B and C are designed such that, when wall C is folded and secured in the slots in wall A, it forms a  $45^\circ$  angle. Wall C has the metallic mirror. Wall A is provided with proper fingers to secure the folded structure as shown in Figure 3.24 with three of the walls closed. After all the walls are folded, the top and bottom views are shown in Figure 3.26.

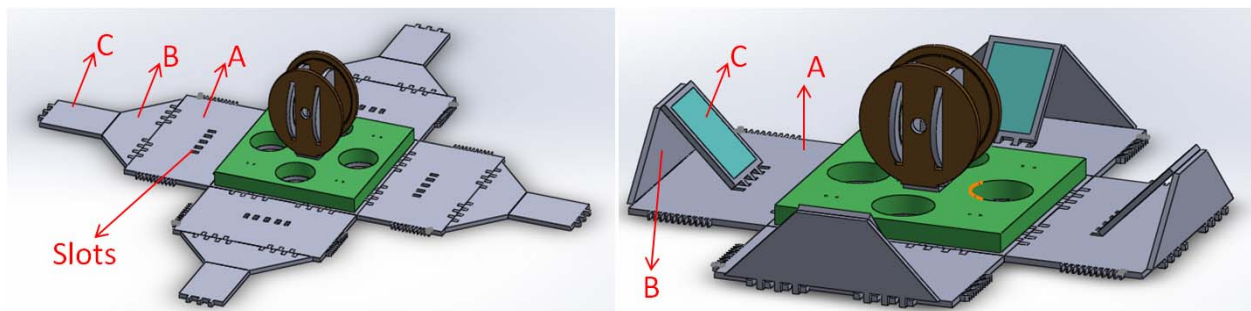


Figure 3.25: Folded structure (left) Completely unfolded (right) Partially folded

The size of the proposed new design is (20 X 20 X 11.6) mm compared to the previous fabricated sample of (39.2 X 39.2 X 12) mm, which is almost  $1/4^{\text{th}}$  of volume or base area.

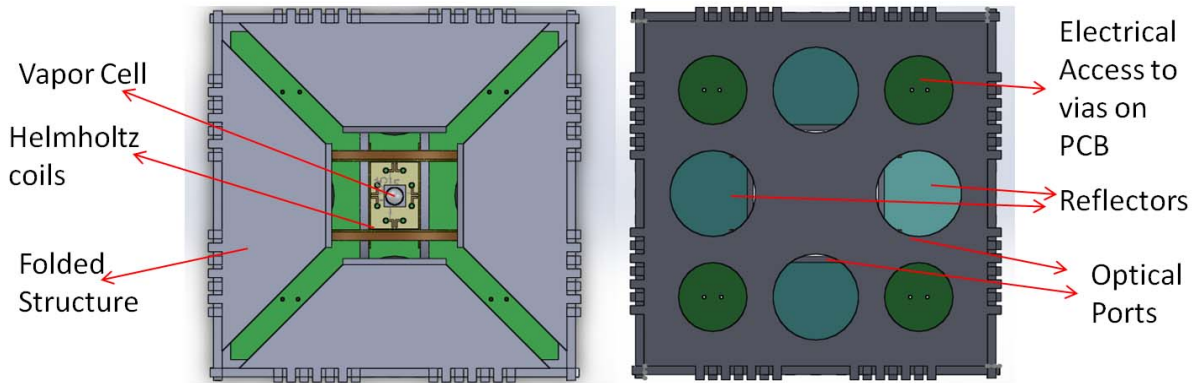


Figure 3.26: Folded structure (left) Top view (right) Bottom view

### 3.5.1 Redesign of Helmholtz Coils

The previous design of Helmholtz coil had a foot print of (25 X 25) mm due to the flexible traces. Hence the coils had to be redesigned to fit inside the modified folded structure. The radius of the coil was kept the same, but the traces were modified to fit inside the base of the folded structure. Assuming just the Helmholtz coils and the traces, the previous design had homogeneity of 660 ppm, whereas the new design had 540 ppm, calculated analytically. It shows that changing the design of the traces had minimal effect on the magnetic field generation. Moreover, the new design had a Si structure under the polyimide to provide more support and robustness to the traces compared to the previous samples. The new design, shown in Figure 3.27 occupies a foot print of approx. only (18.5 X 18) mm after folding, which easily fits inside the new folded structures.

### 3.5.2 Mask Design

Once all the practical concerns were addressed, a three layer mask was designed for both folded structure and Helmholtz coils. The masks are shown in Figure 3.28 below to be used for 4" Si wafers.

The mask for the folded structures shows 4 small structures placed around the wafer. These

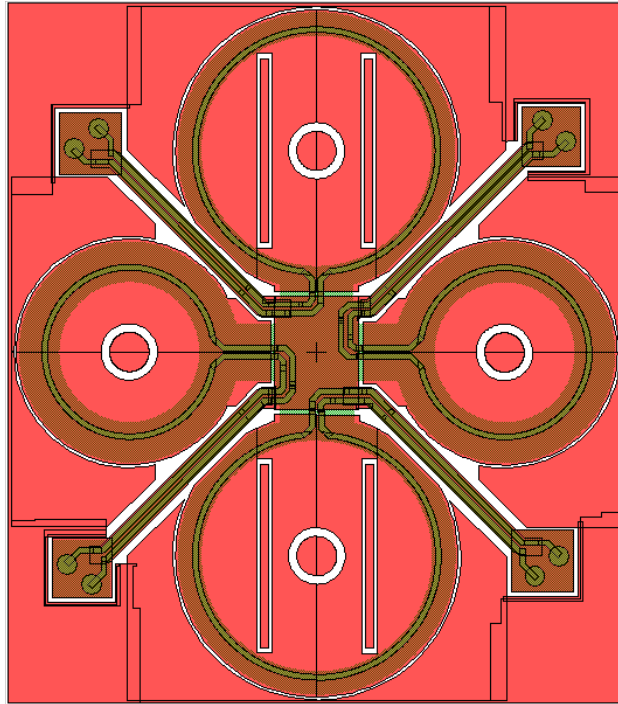


Figure 3.27: Modified Helmholtz coil design

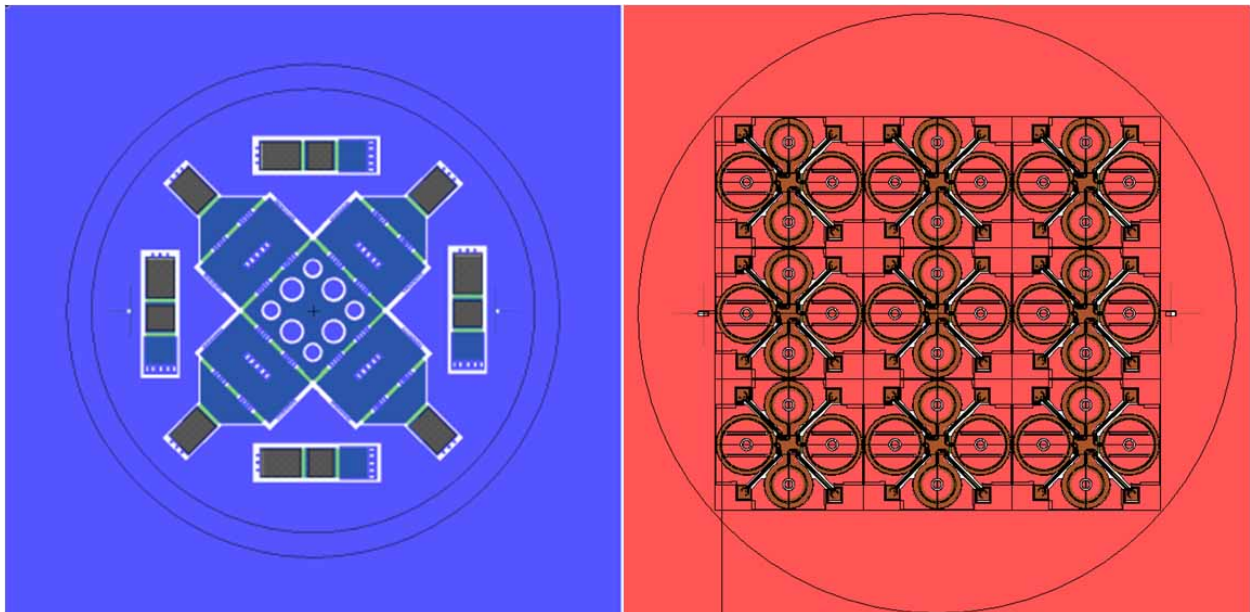


Figure 3.28: (left) Mask for new folded structure (right) Mask for modified coil design

are small folding structures that would be folded to become a  $45^\circ$  reflecting surface. These small structures would be used to characterize the metallic reflectors. Also these would be used for optical path arrangement. The mask for coils shows an array of coils, a total of 9 units.

### **3.5.3 Fabrication**

The fabrication would be a three mask process, one each for polyimide processing, metal deposition, and Si back side etching. The fabrication flow is depicted in Figure 3.29 for both designs, the only major difference being that for folded structures, the metal is deposited on opposite side of polyimide and for the coils, metal is deposited on the same side to form the metal traces. 4" DSP Si wafers have polyimide spun on them and patterned with the 1st mask. Thermal Curing of Polyimide is done to achieve the desired properties. Metal (500  $\text{\AA}$  Chromium and 5000  $\text{\AA}$  Gold) is deposited on the required side. Chromium provides better adhesion. Photoresist is spun on top of the metal and patterned using the 2nd mask. Later, metal etching is done to get the required pattern. Both Gold and Chromium etch are performed. Covering the polyimide side with dicing tape, photoresist is spun and patterned using 3rd mask to define the structure on the Si wafer. Then through wafer Si etching is done to release the devices.

### **3.5.4 PCB Design for Assembly**

A small PCB was designed for assembly of the coils onto the folded structures. This PCB has vias and traces onto which the Helmholtz coils would be assembled and the traces of the coils can be wire bonded onto the bare traces on the PCB. A bare trace PCB with Silver traces was tried earlier but had wire bonding issues. Hence the new design with bare Gold traces was fabricated for ease of wire bonding. The mounting holes on PCB are placed

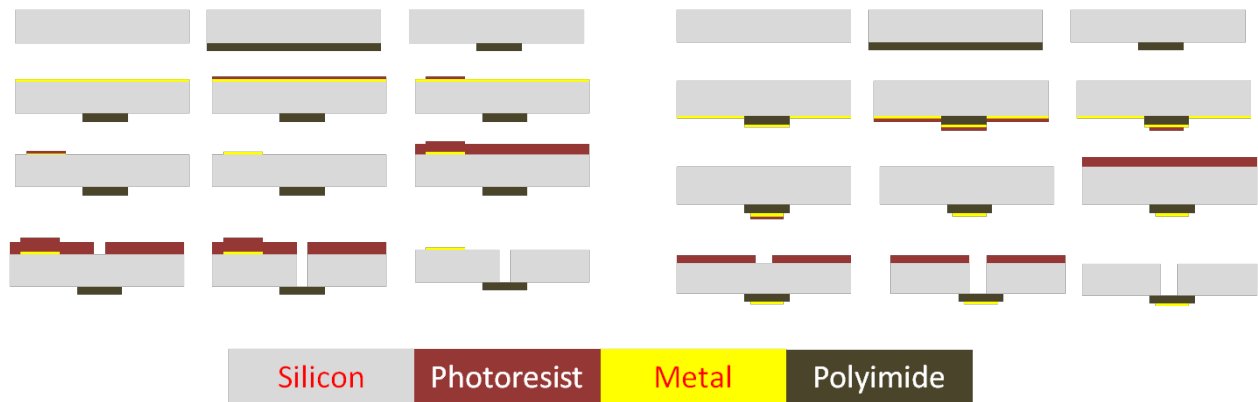


Figure 3.29: Fabrication process (left) Folded structure (right) Coils (Read the process flow as column wise then row wise)

matching the pattern of the bottom plate of the folded structures, for optical ports. The vias on the PCB would be centered exactly on the electrical access holes of the bottom plate for connecting to Helmholtz coils and also for heater. The PCB design is shown in Figure 3.30. The footprint is approx. (19 X 19) mm which easily fits inside the new folded structure.

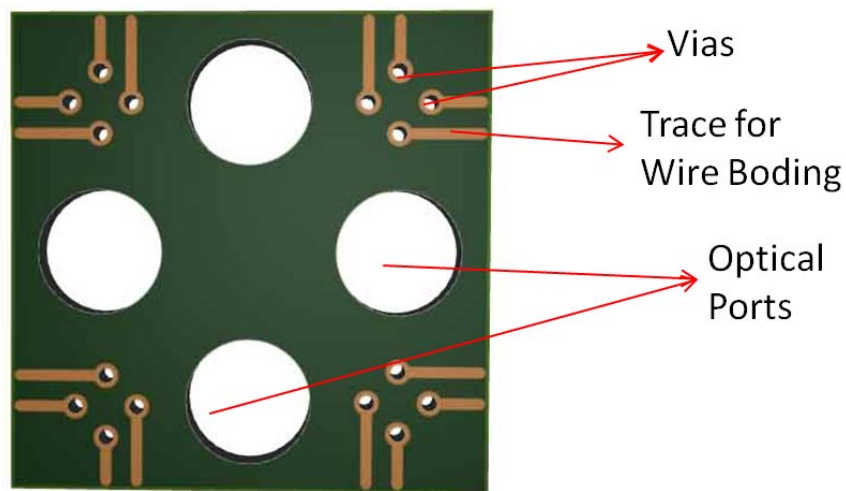


Figure 3.30: PCB design

### 3.5.5 Assembly

The fabricated coils and the folded structure along with the fabricated PCB were assembled to mimic the Solidworks design. The assembled device is shown in Figure 3.31. The final

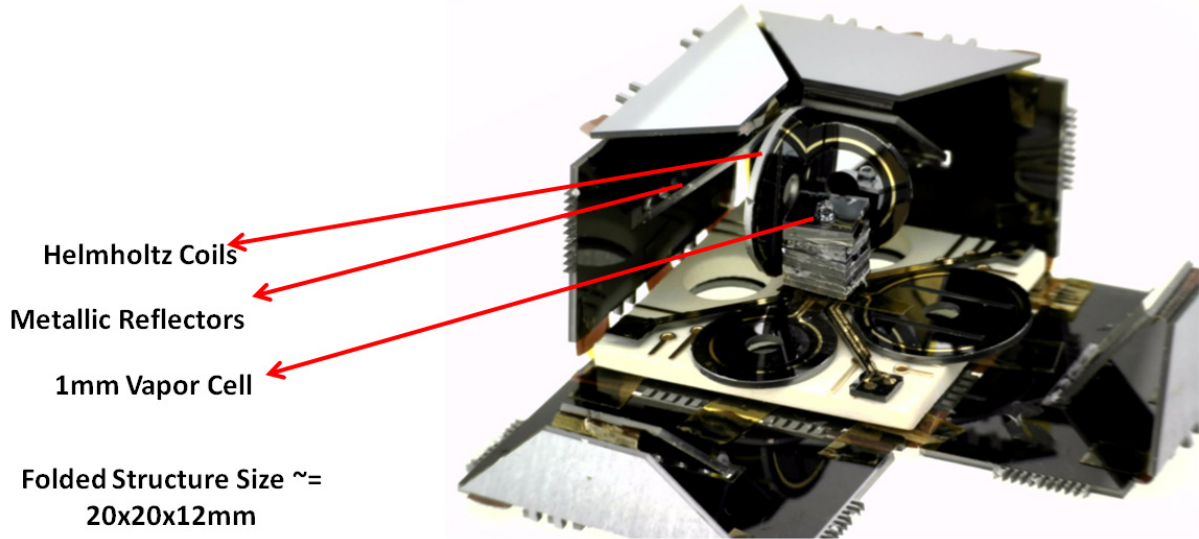


Figure 3.31: Assembly of the new folded prototype

size was  $1/4^{\text{th}}$  the size of the previous prototype. This assembly shows the proof of concept for the design.

### 3.5.6 Metallic Mirror Comparison

A similar setup to the optical characterization used for dielectric mirrors is shown by using only a single metallic mirror in Figure 3.32. The reflected power and the polarization change are compared to the dielectric case.

The power detected after reflection from metallic mirror and from a dielectric mirror are tabulated in the Table 3.3.

Power	Dielectric mirror	Metallic mirror
Input = $177 \mu\text{W}$	$171 \mu\text{W}$	$138 \mu\text{W}$
Reflectivity	96%	78%

Table 3.3: Reflectivity comparison

The other metric to compare is the polarization change upon reflection. The degree of polarization represented as ellipticity is tabulated in Table 3.4, when the output is measured

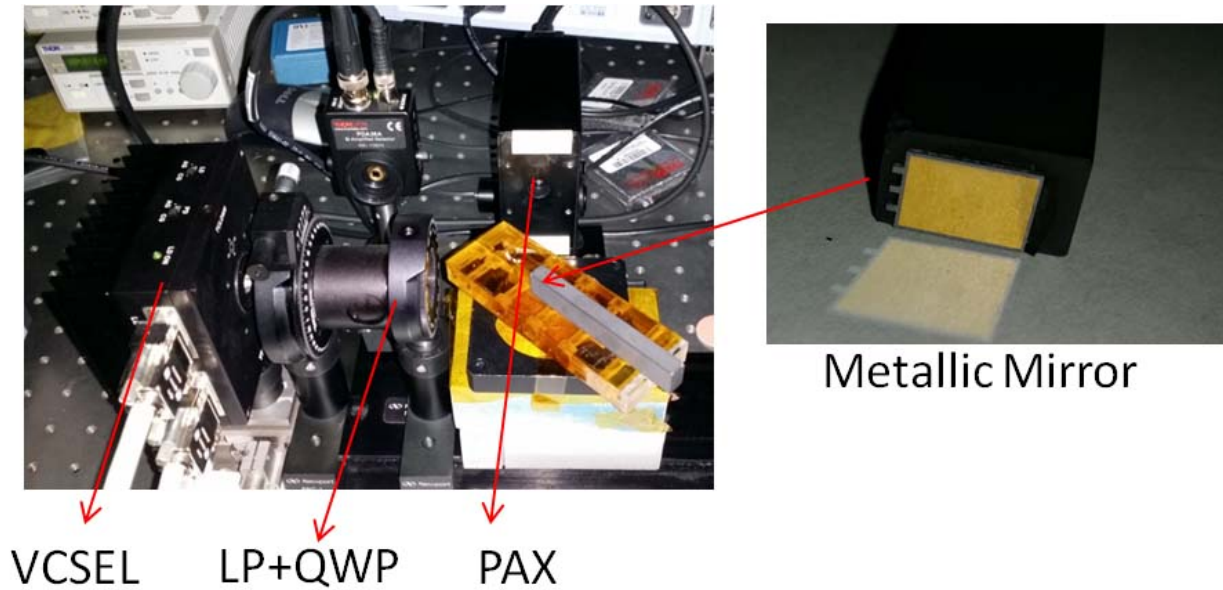


Figure 3.32: Metallic mirror characterization setup

after reflecting from the mirror.

<b>Ellipticity</b>	<b>Dielectric mirror</b>	<b>Metallic mirror</b>
Initial = 44.4°	7°	40°

Table 3.4: Polarization comparison

The VCSEL power also is a significant parameter in polarizing Rb. A simple analytical model was developed using the Rb polarization equations from [35] to create a Rb polarization % versus VCSEL power plot as shown in Figure 3.33. The figure shows that due to usage of metallic mirrors, there is change in approx. 10%, but this can be recovered by operating at a slightly higher temperature, say by increasing the operating temperature by 5°C. Or using a higher power laser would also work in this case.

### 3.6 Magnetic Shielding

The final assembled prototype has to be placed inside shields to cancel out the effect of spurious magnetic fields including the Earth's field. The nominal Earth's field is around 50

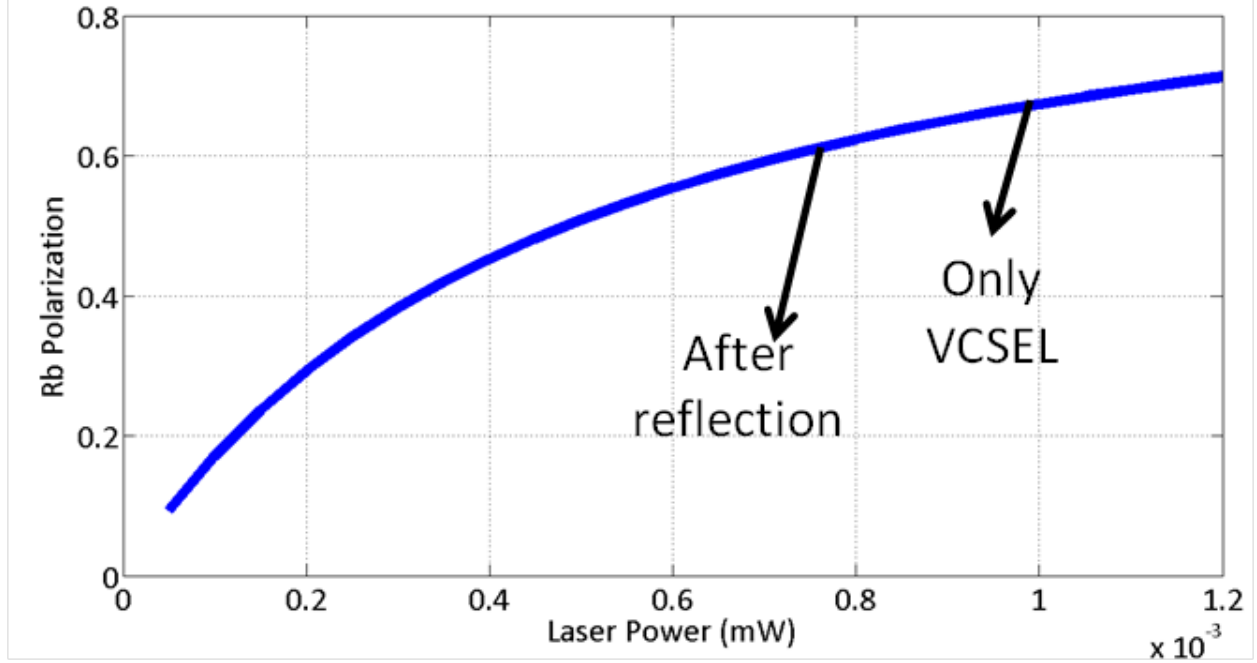


Figure 3.33: Rb polarization vs laser power, after reflection from metallic mirror

$\mu\text{T}$ . There are two kinds of shielding, active shielding [19] where a two isotope approach could eliminate the dependency of the detected rate on the applied static magnetic field and passive shielding, which could be provided by the packaging itself. A conservative shielding factor of  $10^6$  is chosen for the external shield design.

### 3.6.1 Analytical Modeling

Shielding factor of a cylindrical shield is defined as  $S = \mu t/d$ ,  $\mu$  = magnetic permeability of the material,  $t$  = thickness and  $d$  = diameter of the shields. Obviously a single shield cannot provide the required shielding. Hence a nested shield design is explored, where cylinders with varying diameter will be placed around the folded assembly thus providing the required shielding. The shielding factor due to 'n' nested shields is given as

$$S = S_n \prod_{i=1}^{n-1} [1 - (\frac{D_i}{D_{i+1}})^k] \quad (3.2)$$

where  $D_i$  = diameter of  $i^{th}$  shield, where  $S_i$  = Shielding factor of  $i^{th}$  shield,  $k$  is a design factor and for transverse shielding of cylinders,  $k = 2$  [58].

Using this equation, shielding factor and size were optimized for different thickness and diameters, the thicker the shields, the more the shielding factor and larger the shields, lesser the shielding. A shield thickness of  $500 \mu\text{m}$  was chosen and the gap between the cylinders was chosen as  $2500 \mu\text{m}$  in order to minimize the size. These specifications were the minimum possible design features as confirmed by the manufacturer. The Figure 3.34 shows shielding factor and volume for different number of shields.

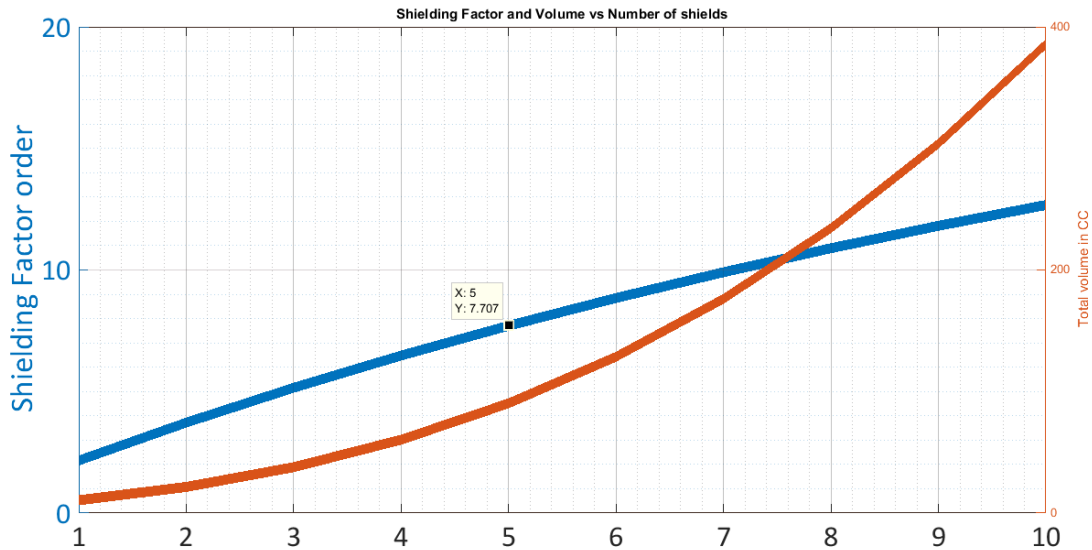


Figure 3.34: Shielding factor and volume vs number of shields

### 3.6.2 Design

Assuming a very conservative value of magnetic permeability  $\mu = 10,000$ , using just 5 shields we can achieve shielding factor on the order of  $10^7$ . However, due to presence of ports for the optical access and also for electronics access, the lid of the cylinder would have several holes and thus reducing the shielding factor slightly. So a layered 5 shield design is chosen for manufacturing. This would occupy a total volume of around 90 cc. Solidworks sketches

are designed as proof of concept. So an initial cylinder diameter of 31 mm is chosen to fit exactly around the assembled prototype. Thereafter, each new cylinder is added with a gap of  $2500\mu\text{m}$ . The completed shield assembly and the cross section of the assembled prototype are shown in 3.35. However, FEM modeling was necessary to confirm the magnetic shielding of this design.

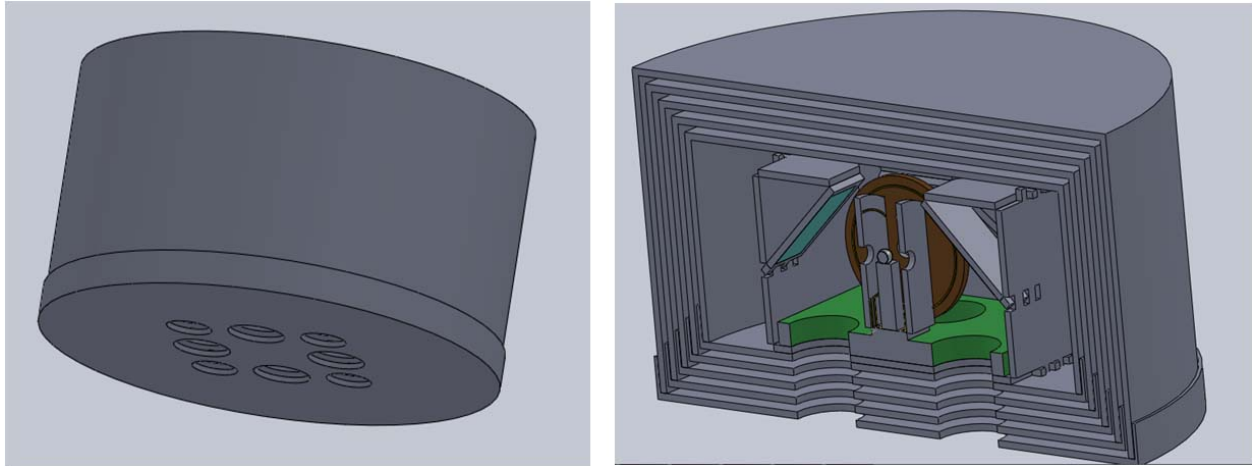
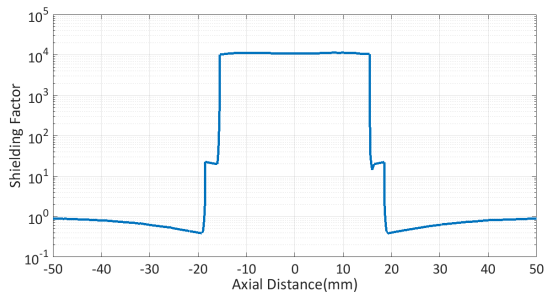


Figure 3.35: Magnetic shield design (left) fully assembled (right) Cross section view

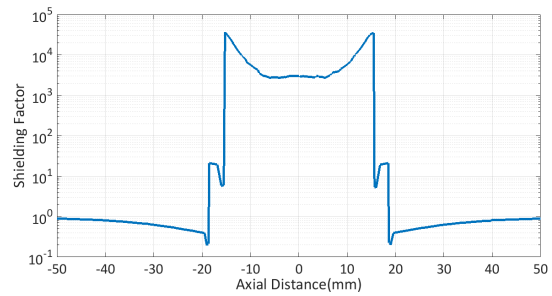
### 3.6.3 FEM Modeling

Based on the Solidworks design, FEM models were simulated in COMSOL. Different parameters like effect of optical ports, thickness of the shields and spacing between the shields were studied with just two nested shields for quick simulation time. The Figure 3.36 compares the effect of change in shielding factor due to presence of optical ports on the bottom of the shields as per the design. The Figure 3.37 shows the effect of changing spacing between the shields and changing the thickness of the shields.

So a spacing of 2.5 mm and a thickness of 0.5 mm are chosen as per the manufacturing specs. The FEM modeling for a 4 layered nested shields is shown in Figure 3.38 including all optical and electrical ports.

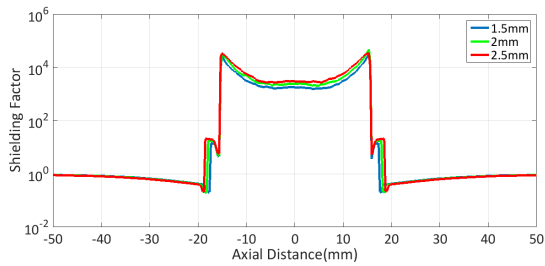


(a) Shields with no optical ports

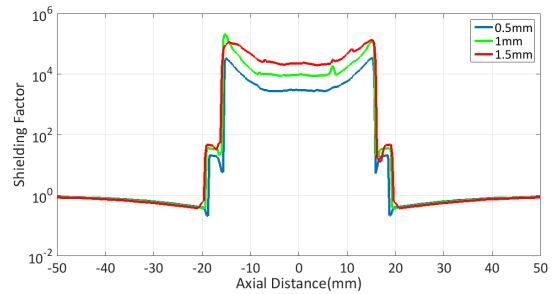


(b) Shields with optical ports

Figure 3.36: Effect of optical ports on shielding factor



(a) Varying spacing



(b) Varying thickness

Figure 3.37: Effect of spacing and thickness on shielding factor

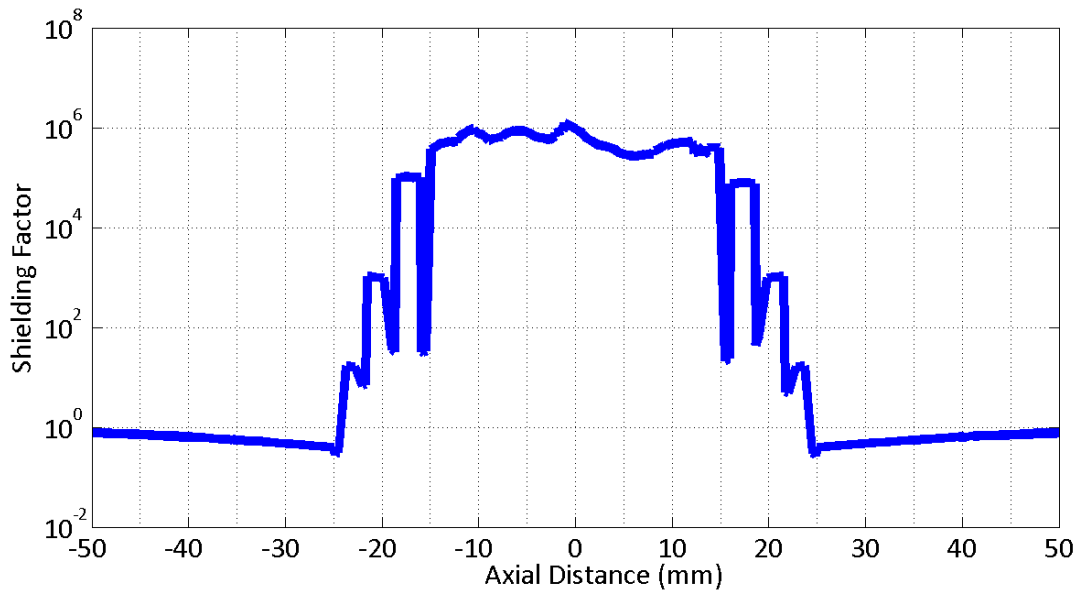


Figure 3.38: Shielding factor of 4 layer nested shields

### 3.6.4 Manufactured Shields

Based on modeling and analysis, a 5 layered shields were manufactured by Amuneal that have spacer rods between the shields to keep them in place. This is shown in Figure 3.39.



Figure 3.39: Manufactured 5 layer magnetic shield

# Chapter 4

## Experimental Setup and Characterization

The first few sections of this chapter describe all the efforts done to setup a working test bench for characterization of miniaturized NMRG. Initial attempts were made to conduct NMR experiments using a macro cell. This helped to fine tune aspects of the setup without worrying much about the optical alignment issues. Once all the details of the setup were addressed, the macro cell was replaced with a micro cell where optical alignment inside the shields becomes a huge challenge. The efforts in this regard are described here.

### 4.1 VCSEL/Optics Setup

A 795 nm VCSEL from Princeton Optronics was used for few experiments before it started exhibiting polarization switching phenomenon. Later VCSEL from Oclaro was used for most of the experiments. All the optical components are bought from Thorlabs/Newport Corp.

VCSEL's are current controlled and temperature stabilized components. The output wave-

length is a function of both these parameters. Temperature is usually kept constant at an operating point and the current is varied to tune for the desired wavelength. Characterization of some of the important parameters is discussed in Section 4.1.1.

The VCSELs have a very divergent beam. A collimating lens is usually needed to provide a collimated beam. Appropriate lens based on the distances are chosen to give a collimated beam profile of 3 mm diameter. A macro lens outside the mount is used to collimate the beam further.

A system of lenses can be used to increase the beam diameter or compress it. A conventional optical diagram and calculation reveal the required focal length of the lenses for the beam compression. Standard components of the shelf are used for beam splitting, linear polarizer, quarter wave plate etc. The photodetector with integrated amplification and highest sensitivity at the desired wavelength are used as detectors. The gain, noise figure and output bandwidth are always at a trade off. Careful gain selection is crucial for better SNR.

#### **4.1.1 VCSEL Characterization**

VCSELs from Oclaro (2 of them) were mounted in Thorlabs TCLDM9 separately, by carefully following the pin configurations. Figure 4.1 shows the assembly inside the VCSEL mount. The pin configuration has to be carefully verified using the data sheet and also the pin configuration on the VCSEL mount.

The VCSEL was controlled using Thorlabs temperature and current controller. The limits of temperature and current are to be carefully followed based on the data-sheet. The VCSELs were then characterized for different parameters in Table 4.1. These results were compared to the data-sheet to verify proper operation of VCSEL. The Figure 4.2 shows the results.

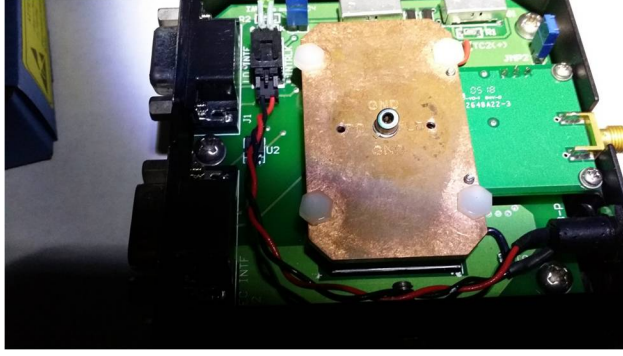


Figure 4.1: VCSEL mounting

Parameter	VCSEL 1	VCSEL 2
Power(mW) at 4mA	0.28	0.26
$\Delta\lambda/I$ (nm/mA)	0.21	0.22
$\Delta\lambda/T$ (nm/ $^{\circ}$ C)	.037	.06

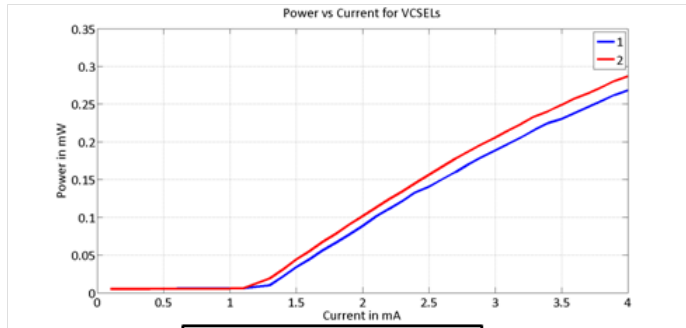
Table 4.1: VCSEL characterization

## 4.2 DC Heater Oven

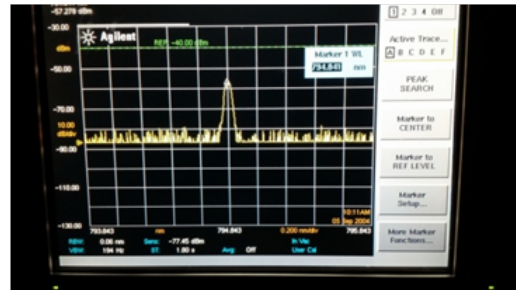
The Rb inside the cell needs to be heated in order to increase the vapor number density. Rb starts vaporizing at around  $40^{\circ}\text{C}$ . The heaters were commercial polyimide flexible heaters from Thorlabs. A temperature sensor was also attached to monitor temperature. A small oven was built with insulation and the heater to fit the macro cell (1") inside. The DC heater was heated to  $104^{\circ}\text{C}$ , and then turned off and then the temperature variation versus time was plotted to check the efficiency of insulation and the time available for measurements without significant variation. It took about 10 minutes to decrease by  $10^{\circ}\text{C}$  thus proving the feasibility of turning off the heater while making measurements (Figure 4.3).

## 4.3 Macro Coils/Shields

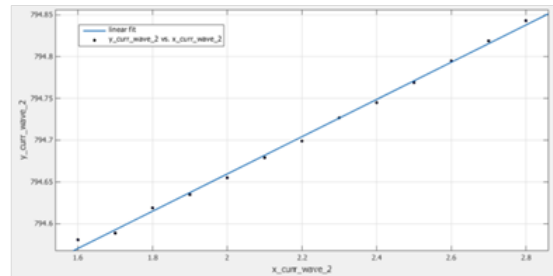
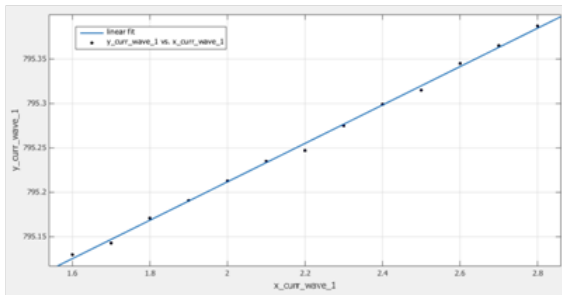
The magnetic shields (MS-1) from Twinleaf provide optical access ports and the atomic cell was centered along these ports. All the optical components were placed on mounts on rails



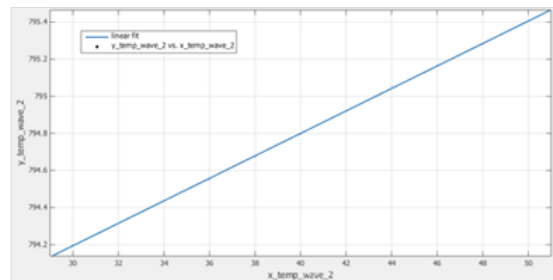
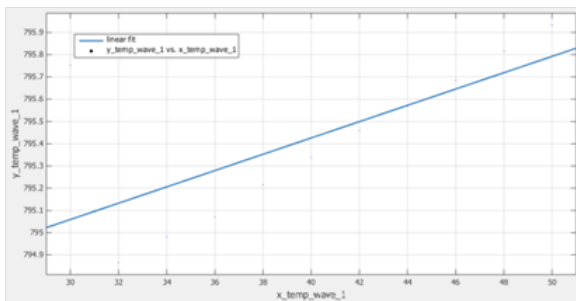
Power vs Current



Freq Spectrum



Wavelength vs Current for both VCSEL



Wavelength vs Temperature for both VCSEL

Figure 4.2: VCSEL characterization

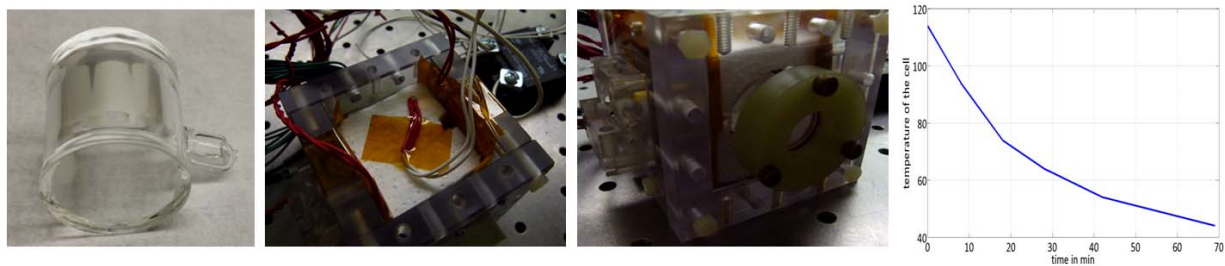


Figure 4.3: (1) Vapor cell (2,3) Heater with temperature sensor (4) Temperature vs time upon turn off

fixed to optical table, in line with the optical ports of the magnetic shields. The shields also have 3 axis coils with 0.49 Gauss/Ampere rating. The cell is placed at geometric center of the shields for uniform magnetic field. These shields provide a shielding factor  $\geq 10^6$  to cancel out Earth's magnetic field and any other disturbances. The shields are shown in Figure 4.4.

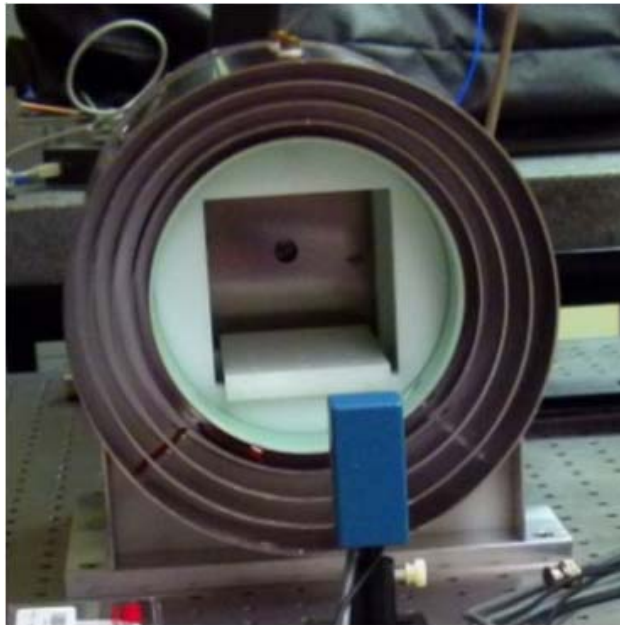


Figure 4.4: Macro shields on optical table

### 4.3.1 Coil Calibration/Degaussing

The macro coils need to be degaussed at least every couple of months. Each time the shields are opened and closed, there might be a build up of residual magnetic field which can interfere with the experiments. The coil current to magnetic field calibration can be done using a Gauss meter. An experimental method would be to find the Zeeman resonances for Rb and compare the current to the applied field along with the input frequency.

## 4.4 Rb Macro Vapor Cell Characterization

A 1" glass cell was used, which contained Rb<sup>87</sup>, Rb<sup>85</sup>, 75 Torr Xe, 50 Torr N<sub>2</sub>, 950 Torr Ne. The heater and the assembly for this cell is shown in the Figure 4.3. By varying the VCSEL source wavelength, Rb absorption for varying temperatures was also characterized to decide the operating temperature with sufficient Rb polarization. This is shown in Figure 4.5. Further measurements were done with cell temperature at around 84°C.

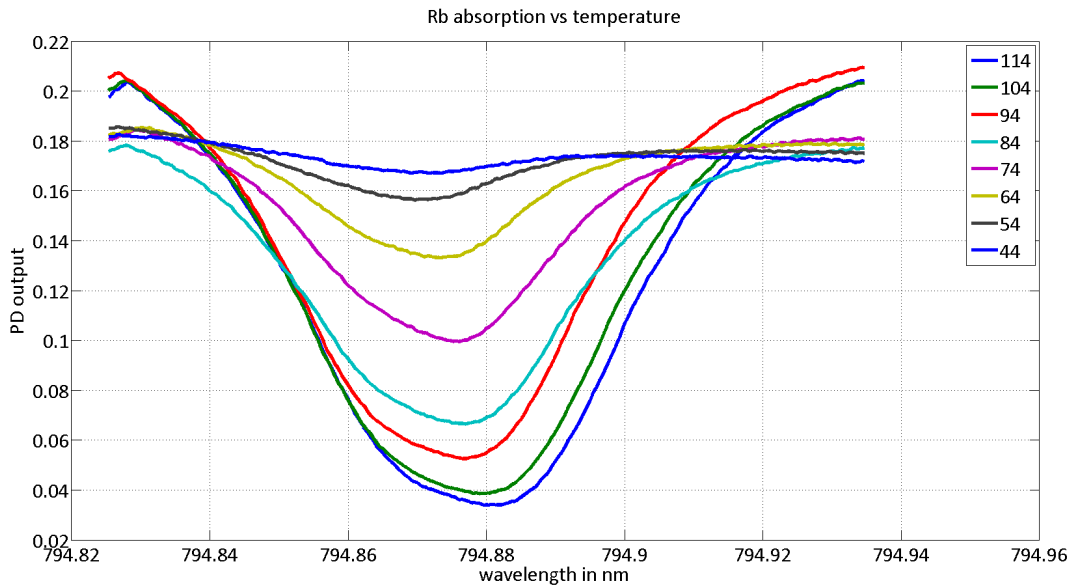


Figure 4.5: Rb absorption vs wavelength for different temperature

### 4.4.1 Zeeman Resonances

The laser source is tuned to wavelength corresponding to Rb absorption exactly. The magnetic shields come with built in 3 axis magnetic coils. A 35 kHz perpendicular axis magnetic field is applied, while the primary axis field is swept. Zeeman resonance was observed as shown in Figure 4.6. Input frequency = 35 kHz. Gyromagnetic ratio of Rb,  $\gamma = 2\pi \times 7$  Hz/10  $\mu$ T  $\implies B_{theory} = 5 \mu$ T.

From the plot for Zeeman resonances, current at absorption dip = 104 mA. For the coil current to magnetic field relation, 1 A corresponds to 0.49 G. So  $B_{exp} = 5.09 \mu\text{T}$ , verifies experimentally the proper operation of the setup.

In Figure 4.6, the bottom trace corresponds to the primary axis swept magnetic field. The top trace corresponds to the photodetector output. In the first repetition, the heater was not yet turned off, and the effect of magnetic field due to heater can be seen as the photo diode output varies significantly. After the heater is turned off, the next 3 measurements show sufficient repeatability in measurement. The experiment was also repeated for different frequencies and temperatures.

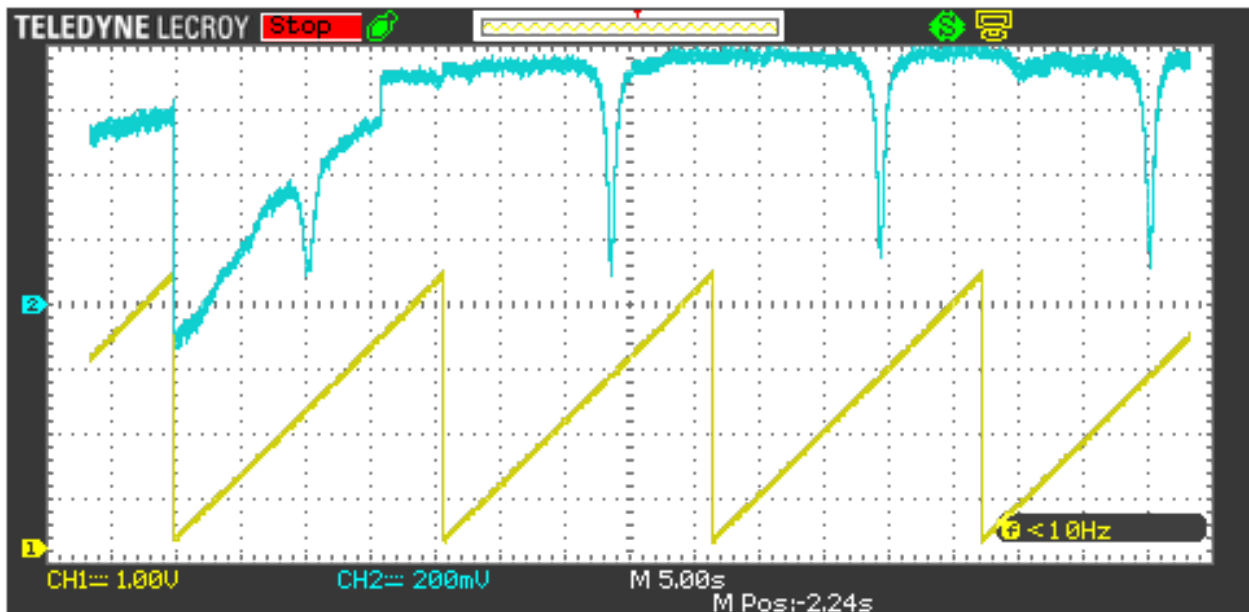


Figure 4.6: Zeeman resonance of Rb

#### 4.4.2 Rb Magnetometer using Macro Cell

The above mentioned setup was slightly modified to demonstrate a magnetometer. Using a beam splitter, a pump and probe beam were optically aligned to interact with the vapor cell. A static magnetic field  $B_0 = 2.8 \mu\text{T}$  was applied along Z axis along with an AC field  $B_c$

$= 3.5 \mu\text{T}$  at  $f_c = 17 \text{ kHz}$ . The orthogonal direction had an AC magnetic field  $B_1 = 10 \text{ nT}$  at  $f_a = 30 \text{ Hz}$ . The output of the probe beam was detected using a photodetector and this signal was fed into Lockin amplifier to demodulate at  $f_c$  and  $f_a$ . Later the static field was varied to observe the absorption and dispersion mode curves for the Rb magnetometer. The line width was approximately  $130 \text{ nT}$ . The frequency spectrum was measured after the first demodulation to give a signal at  $30 \text{ Hz}$ . This signal was measured to determine the sensitivity of the magnetometer, which was around  $150 \text{ pT}/\sqrt{\text{Hz}}$ . The absorption and dispersion mode of Rb magnetometer are shown in Figure 4.7

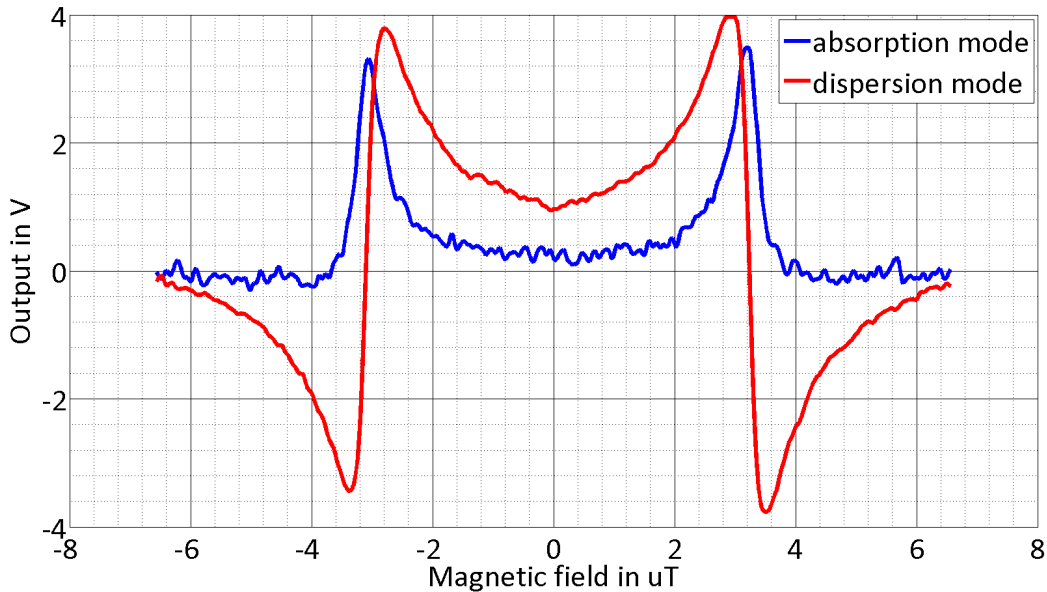


Figure 4.7: Rb magnetometer absorption and dispersion mode curves

## 4.5 Micro Vapor Cell Magnetometer

After demonstrating the experiments with macro cell, the feasibility of the setup was proven. The next step was to validate the micro cell. The setup and further experiments with Xe are also described here.

### 4.5.1 NMR Setup

The optical schematic of the setup is shown in Figure 4.8. The components are briefly described below.

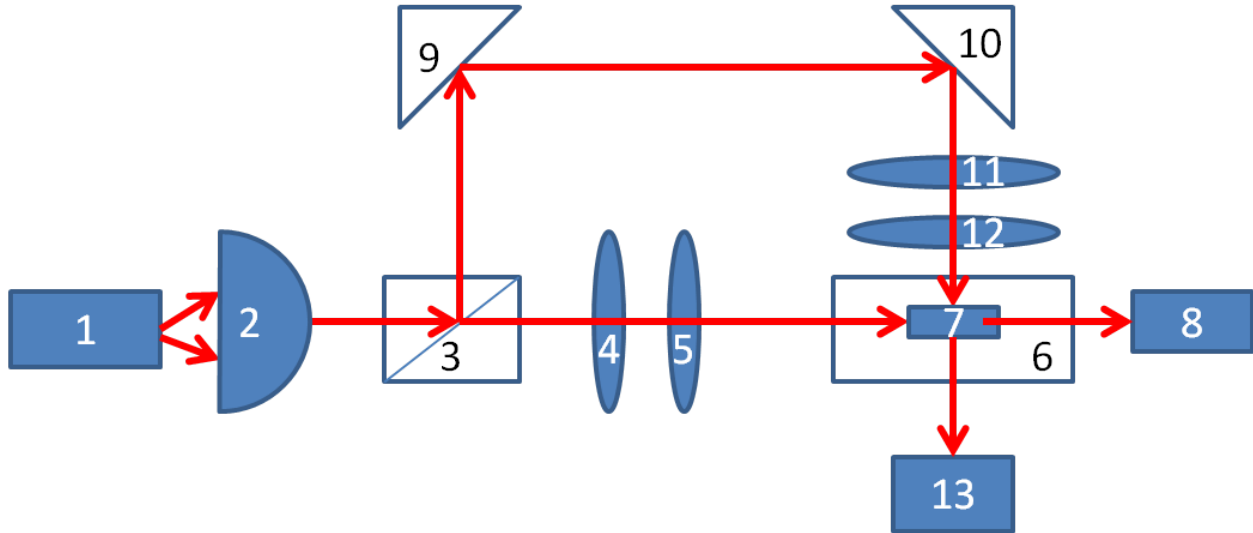


Figure 4.8: Optical setup for cell characterization

1. VCSEL : A 1 mW output power VCSEL from Oclaro was used. The VCSEL was securely placed in a temperature controlled mount (from Thorlabs, TCLDM9). The output wavelength was tuned by varying the current to the VCSEL, keeping the temperature constant.
2. Collimator lens : A plano-convex lens with approx. focal length around 50 mm, was placed at a suitable distance after the VCSEL to collimate the beam such that the beam spot size was around 1 mm.
3. Beam splitter : Non-polarizing beam-splitter (from Thorlabs, CM1-BS014) was used to split the beam into a probe beam and a pump beam with equal powers. Due to the extra path covered by the probe beam, its power reduces before hitting the cell.
4. Linear polarizer : Linear polarizer (from Thorlabs, GT15-B) is placed along the pump path before the quarter wave plate. The light is linearly polarized after passing this.

5. Quarter wave plate : QWP (from CVI, QWPO-795-05-4-R10) is used to circularly polarize the pump beam.
6. 4 Layer magnetic shields : The shields (from Twinleaf, MS-1) have a shielding factor around  $10^6$  and also have a set of 3 axis coils. The magnetic field inside the shield can be controlled by current sources (function generators) placed outside.
7. Atomic vapor cell : Any atomic vapor cell can be placed inside the shields with corresponding heating assembly to vaporize Rb.
8. Photodetector : A photodetector (from Thorlabs, PDA36A) with highest sensitivity in the required wavelengths (around 780 to 800 nm) of interest was used for detecting the pump beam. This was used to align the vapor cell inside and also to optimize any alignment issues based on detected power.
9. Reflector : General purpose Silver coated mirror (from Newport, 5103) were used to steer the probe beam accordingly to reach the vapor cell.
10. Reflector : Same as above.
11. Linear polarizer : Same component as described above, but this is placed in the probe beam path.
12. Quarter wave plate : Same component as above, to polarize the probe beam.
13. Photodetector : Same as above to detect the probe beam power.

A brief review of the setup is provided below. Unfortunately while doing some of the experiments, the micro glass blown cell (size 1 mm) was broken. A couple of small vapor cells were borrowed from Northrop Grumman (NGC) for testing at UCI. The cells are around (2 X 2) mm with square faces. This cell was placed on top of a commercial resistive heater. Thermal insulation around the cell was provided by styrofoam. Optical access to the cell

was provided carefully as shown in Figure 4.9. The whole assembly was placed inside the macro shields. A thermal sensor was also placed such that it was in contact with the cell at all times for temperature control. Commercial optics was arranged outside the shields to provide both the pump and probe beam laser path as shown in optical schematic. This was a highly challenging alignment task considering the adjustment of a micro cell inside a macro shield within a precision of 1 mm.

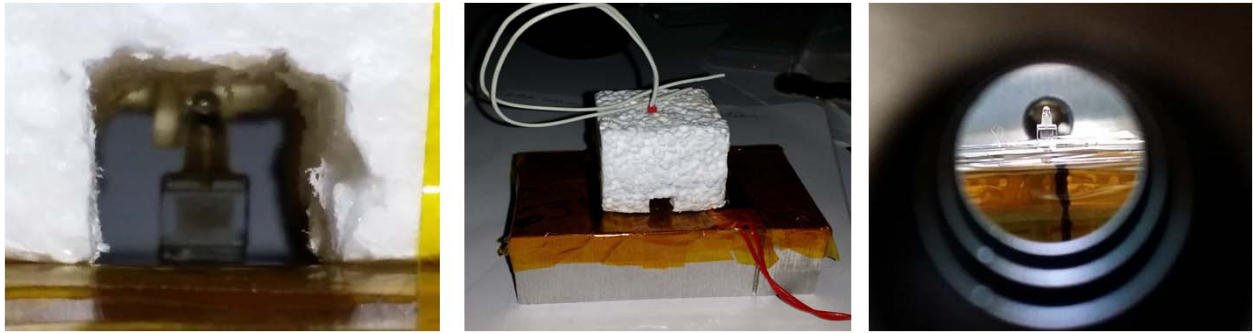


Figure 4.9: Micro vapor cell aligned inside macro shields

The VCSEL source was properly collimated using plano-convex lens to provide a collimated beam of approx. 1 mm in size maintained over a long distance. After collimation, the light is split using a beam splitter to provide both pump and probe beams. The pump beam is then passed through a Linear Polarizer and a Quarter Wave plate (LP+QWP) before interacting with the cell placed inside the shields. The LP+QWP are adjusted accordingly to provide a circularly polarized light. The probe beam is routed to reflect twice off the commercial reflectors and passing through another set of LP+QWP before interacting with the cell inside the shields in the orthogonal direction to the pump beam. Photodetectors placed outside the shield detect the light passing through the cell. The voltage on the photodetector is analyzed for proper alignment of the cell inside the shield along with IR sensitive cards (from Thorlabs VRC2, VRC2D1). The cell was heated up to around 100°C and the VCSEL current was swept to observe Rb absorption spectrum. The measurement was repeated at several temperatures and also for both pump beam and probe beam to confirm the optical alignment in two axes. The VCSEL wavelength at the absorption dip was 794.93 nm.

## 4.5.2 Zeeman Resonances and Magnetometer

The same measurement procedures as done in section 4.4.2 were followed to demonstrate the Zeeman resonance and magnetometer using micro cell. The orientation of magnetic fields is shown in Figure 4.10.

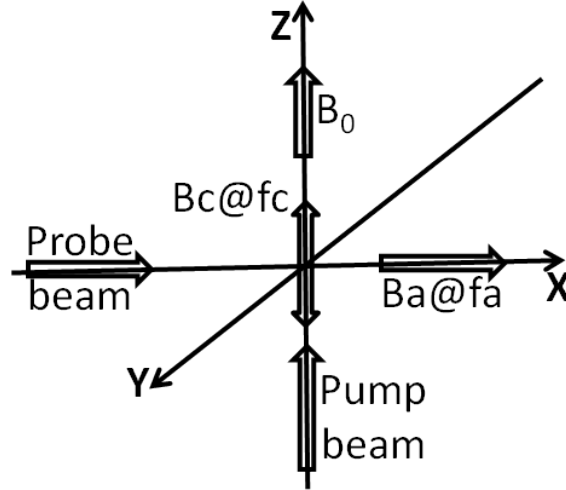


Figure 4.10: Orientation of magnetic fields

## 4.5.3 Magnetometer Sensitivity

In order to reconfirm the operation of the setup as a magnetometer, the following conditions were applied. With a carrier field of  $B_c = 3.5 \mu\text{T}$  at 24.5 kHz and a small varying magnetic field 100 nT signal at 41.5 Hz on the sensitive axis, the scale factor was extracted from the spectrum for the signal peak at 41.5 Hz corresponding to 100 nT in magnetic field. This yielded a scale factor of  $100 \text{ nT}/6\text{e-}3 \text{ V} = 16.6 \mu\text{T}/\text{V}$ .

The double demodulated signal was captured for a long duration to estimate Allan variance. The lowest possible signal corresponds to  $6.5\text{e-}6 \text{ V}$  which based on the scale factor yields the sensitivity to be around  $108 \text{ pT}/\sqrt{\text{Hz}}$ .

The next immediate step was to demonstrate the Xe precision signal but Xe was not detected

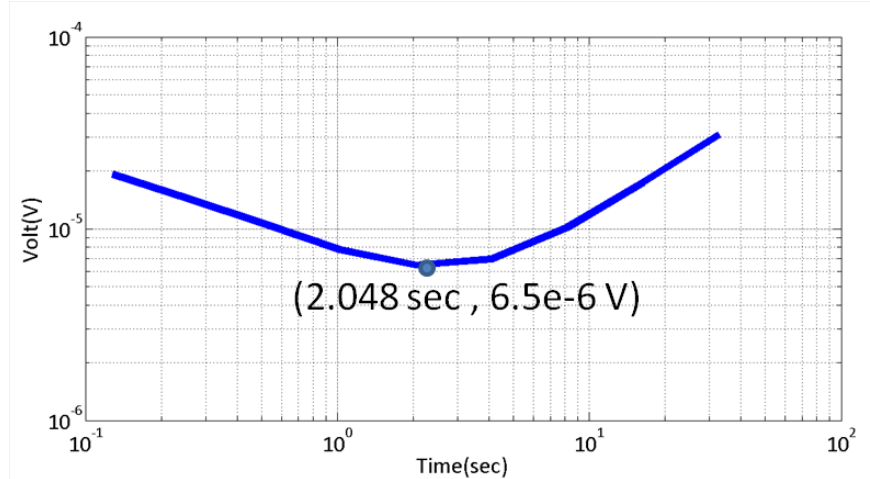


Figure 4.11: Allan variance of Rb magnetometer

upon several attempts. An alternate magnetometer configuration described below was also tried.

#### 4.5.4 Alternate Magnetometer Configuration

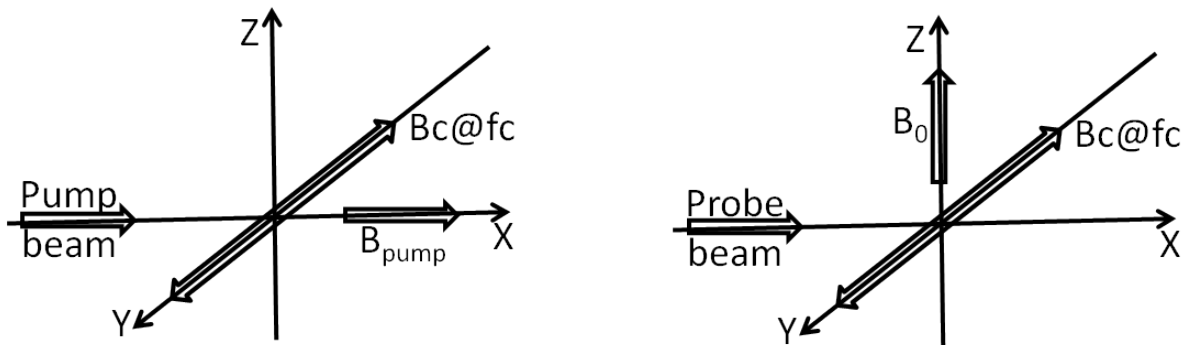


Figure 4.12: Alternate Dehmelt technique

An alternate configuration for magnetometer with only a single probe/pump beam was implemented in order to observe the Xe signal [59]. In this configuration, a small static field is applied along pump/probe axis of magnitude  $1 \mu\text{T}$  (X axis), a carrier magnetic field of  $100 \text{ nT}$  at  $2 \text{ kHz}$  on Y axis and a static field on Z axis of  $130 \text{ nT}$ . The X axis field is on for some time for the optical pumping. After a while X axis field is turned off and the

Z axis field is immediately turned on causing the Xe atoms to precess around Z and thus have a magnetic moment component in the Y axis. The Y axis is the sensitive axis of this magnetometer. This dispersion mode curve is observed in this configuration verifying the magnetometer operation. However, still no Xe response could be observed.

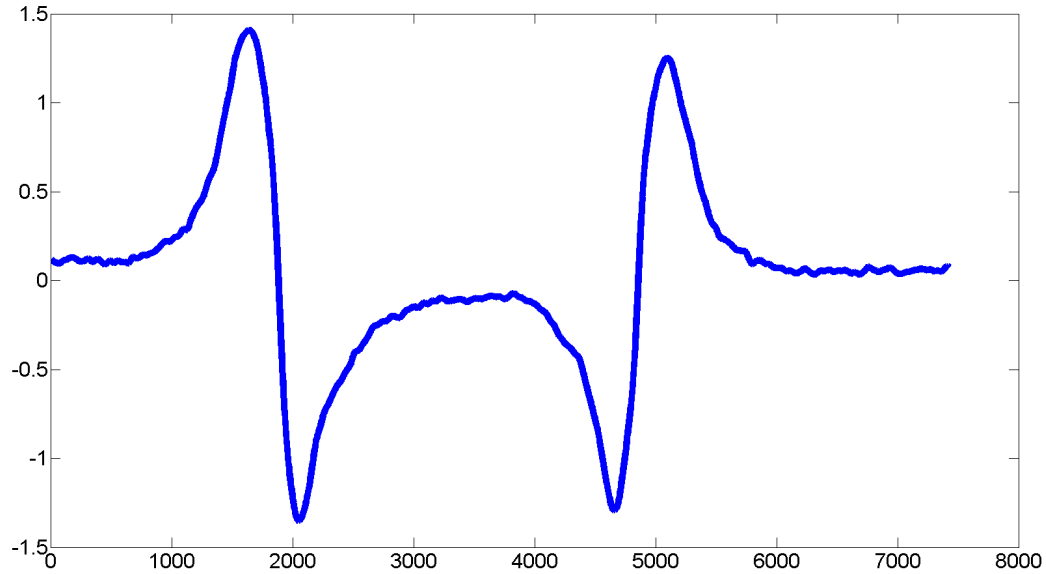


Figure 4.13: Micro vapor cell magnetometer dispersion mode response

## 4.6 Estimation of Xe Signal Level

The Xe signal level inside the cell was estimated based on our experimental setup using the following equations for polarization of Xe [35]

$$P_{Xe} = \frac{P_{Rb}}{\left(1 + \frac{T_{ex}}{T_1}\right)} \quad (4.1)$$

$$T_{ex} = \sigma_{ex} \nu N_{Rb} \quad (4.2)$$

$$B_{Xe} = 730 \times \mu_0 \mu_{Xe} N_{Xe} P_{Xe} \quad (4.3)$$

where,  $N_{Xe}$  for 50 Torr Xe  $\approx 1.2e18$  /cc ,  $P_{Xe}$  = Polarized Xe fraction,  $P_{Rb}$  = Polarized Rb fraction,  $\sigma_{ex}$  = Rb-Xe spin exchange cross section =  $1.6e-20$  cm<sup>2</sup> ,  $v$  = mean thermal velocity =  $\sqrt{\frac{8k_bT}{\pi m}}$ ,  $N_{Rb}$  = Rb number density,  $B_{Xe}$  = Magnetic field due to Xe.

The estimated Xe field was plotted against the change in temperature. All measurements were taken after heating the cell to a certain temperature and then turning off the heater while measuring. But when heater is turned off, there is a steady decrease in temperature which would cause the Rb polarization to decrease and thus also decreasing the Xe magnetic field. Figure 4.14 shows the change in temperature versus time after heater is turned off. The values for estimated spin exchange time and also the estimated magnetic field produced by Xe are tabulated. It can be seen that magnetic field produced by Xe falls below the sensitivity of magnetometer (108 pT) due to rapid decrease in temperature of the cell.

<b>Time sec</b>	<b>Temp C</b>	<b>Tex sec</b>	<b>Pol Xe</b>	<b>B Xe</b>
10	130	68	11%	330 nT
20	120	122	6%	175 nT
40	110	224	2%	67 nT
70	100	423	0.8%	23 nT
120	90	831	0.2%	6 nT
200	80.5	> 1000	<0.1%	.05 nT
300	72.4	> 1000	<0.1%	5e-4 nT

Table 4.2: Temperature vs Xe signal level

The temperature change versus time is plotted and also shows how the Xe signal level falls down in Figure 4.14 .

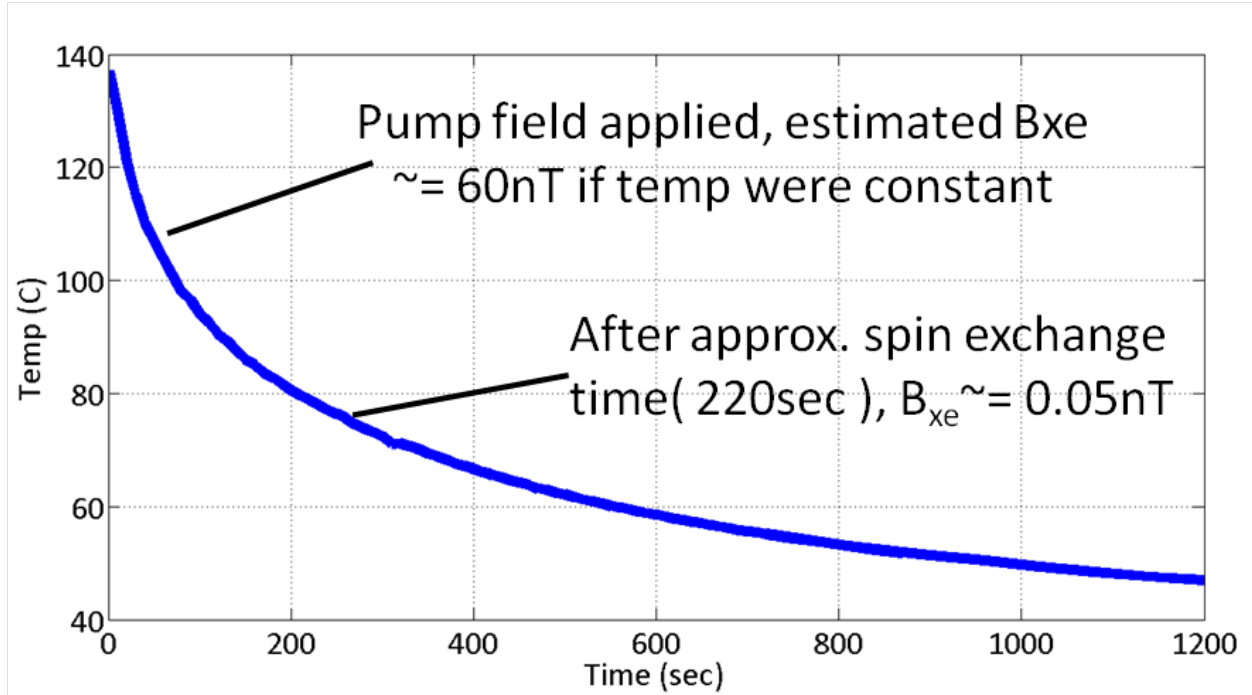


Figure 4.14: Cell temperature vs time

#### 4.6.1 AC Heater Implementation

In order to keep the temperature constant, the heater needs to be always on. This cannot be achieved with a DC heater as it produces static magnetic fields. An AC heater was implemented using breadboard electronics. The schematic of the AC heater is shown in Figure 4.15 [60]. The heater operated at 1 kHz which was still interfering with the system. A function generator amplifier (FGA) from Accel Instruments was acquired to heat the cell at 100 kHz, far away from Rb Larmor frequency of interest at around 18 kHz. The FGA was setup to give the required cell temperature but the Xe signal still could not be detected. Another reason for low Xe signal level could be that there was not enough Rb polarized. Some of the experiments were repeated at a higher cell temperature at around 120°C. After several repetitions and not detecting Xe, a laser source with very high power was used to increase the Rb polarization and thus facilitate more spin exchange, in turn increasing the Xe signal.

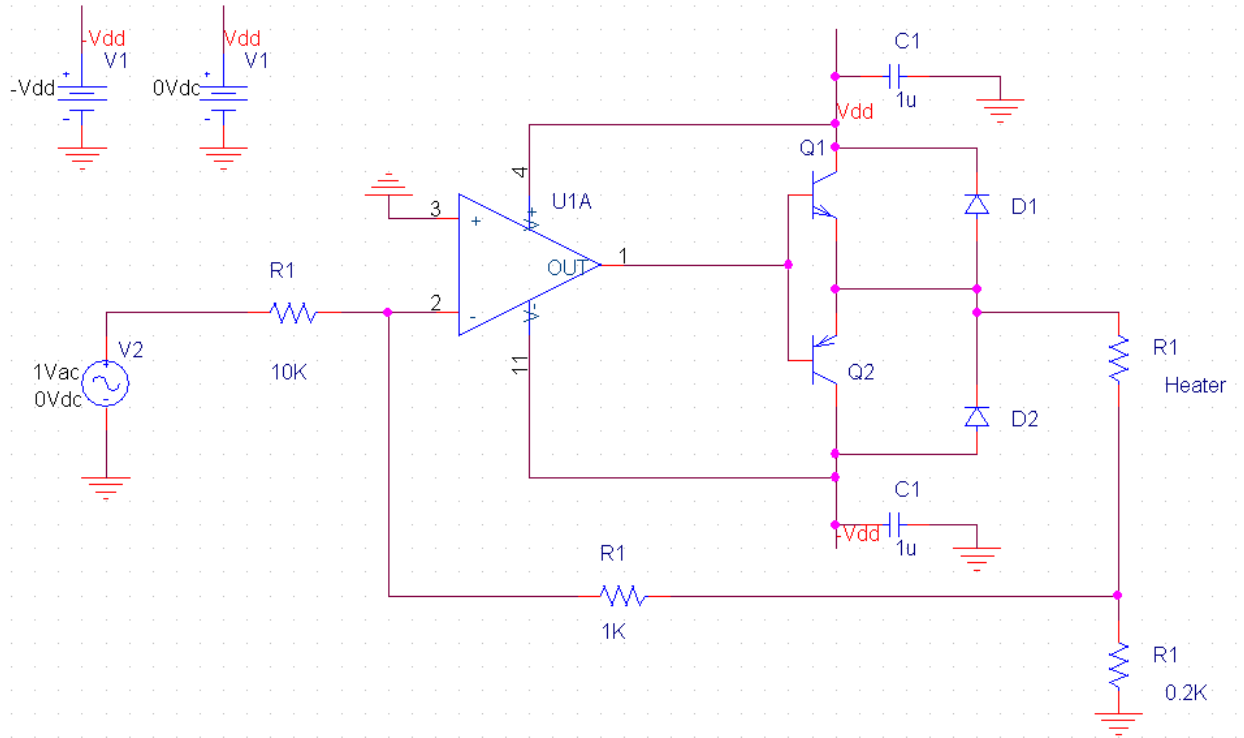


Figure 4.15: Schematic of AC heater

## 4.6.2 Experiments with TOptica Laser

The DLPro system from TOptica was thus tuned for the Rb absorption in micro vapor cell as shown in Figure 4.16. The output power of TOptica laser was around 9 mW and the detected power on photodetector was around 1 mW when the heater is off. After heater is turned on and the optical pumping begins, due to Rb absorption, the detected power was around  $500 \mu\text{W}$ , which was a significant improvement in signal level compared to using a VCSEL. The operating temperature was around  $105^\circ\text{C}$ . With this high power laser and the AC heater at 100 kHz, the Xe signal was finally detected.

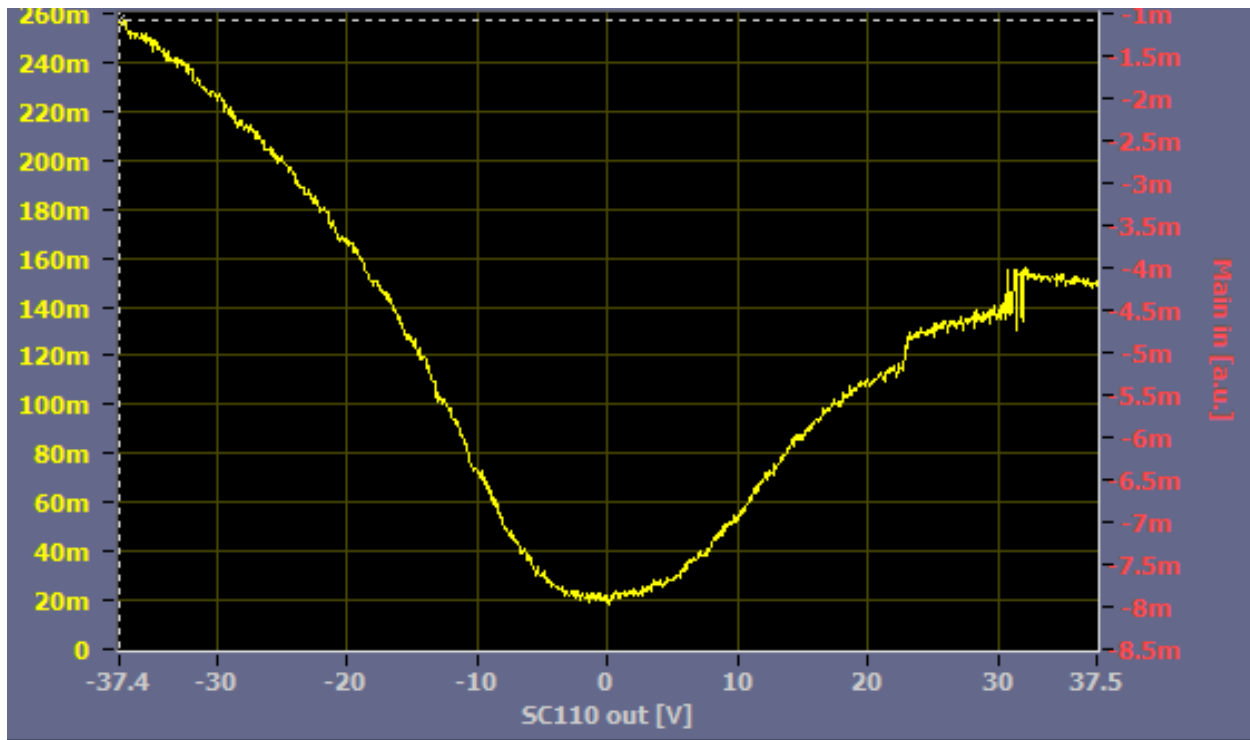


Figure 4.16: Rb dip using TOptica laser source

### 4.6.3 Xe Response Spectrum

Assuming there is sufficient polarized Xe in the cell, it always start precessing around the net magnetic field in the cell. There is always a static field in the Z axis to facilitate optical pumping. So, the Xe starts precessing around this field. However, as discussed earlier, Xe should be flipped into the perpendicular plane to detect Xe. This is achieved by applying a strong static field momentarily (a DC pulse) along the orthogonal direction. So the Xe immediately starts precessing around the combined magnetic field which does not point along Z but as a vector addition of the two applied fields. As the DC field is turned off, the Xe tries to return back to Z direction all the while precessing at the Larmor frequency. So there is a significant component of Xe that can be detected using the integrated Rb magnetometer as described earlier. A sample spectrum in Figure 4.17, shows the two prominent peaks at 12 Hz and 40 Hz corresponding to both isotopes of Xe, when the applied static field is around  $3.5 \mu\text{T}$ . The signal decays slowly as the Xe magnetization returns back to the original Z

direction. This relaxation time parameter is a very crucial performance metric for NMRG. The next section describes several experiments to quantify these.

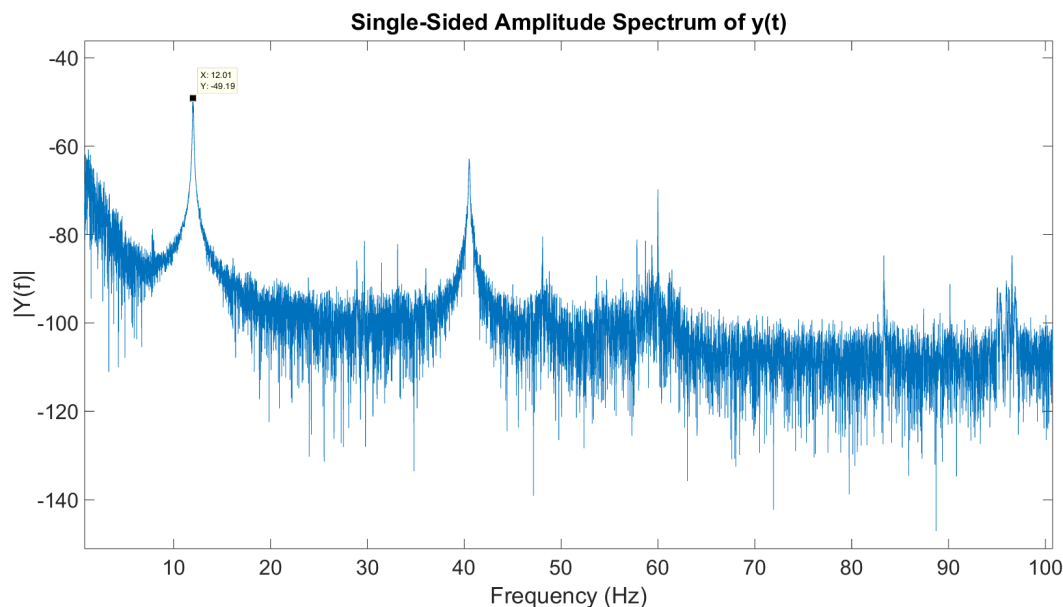


Figure 4.17: Spectrum showing Xe response

## 4.7 Experiments for Relaxation Time Measurements

After having detected Xe responses, the immediate characterization of Xe nuclei was to measure the relaxation times. In this section, briefly each step (experiment) is described with corresponding results.

### 4.7.1 DC Offset Cancellation

Xe precesses around the total magnetic field present at the cell. It is necessary to remove any spurious magnetic fields on different axes in order to observe the correct precession frequency defined by our steady DC field on the main axis. To achieve this, a strong DC field is applied on primary axis; a DC pulse is applied on perpendicular axis. The precession frequency is

noted. The measurement is repeated with the original steady DC field direction reversed. The frequency measured in this iteration is compared with the previous measurement to give the steady state DC error along the primary axis. This process is repeated for all three axes. For our setup we needed to apply DC voltage corrections on X axis = 40 mV and Y axis = 25 mV.

### 4.7.2 Primary DC field (Z axis) Estimation

To optimize the primary DC field, the AC carrier field ( $Z_{ac}$  field) is chosen a priori and the DC field is varied to find the Zeeman resonance peak. In the setup,  $Z_{ac} = 18.5$  kHz,  $Z_{dc} = 4$  V.

### 4.7.3 Cross Axis Rejection Ratio

Once the  $Z_{ac}$  field frequency and  $Z_{dc}$  field have been tuned, the other important parameter to optimize is the magnitude of the carrier field. This optimization involves finding the right  $Z_{ac}$  field amplitude and also the correct phase required for demodulation. This ensures that when Xe is driven continuously, the demodulation does not pick up the drive amplitude itself. By choosing a frequency different from both the isotopes precession frequency, the  $Z_{ac}$  amplitude is varied each time a continuous drive is applied on both X axis and Y axis. The phase of demodulation is adjusted to give the maximum signal when the signal is applied on Y and gives a null when applied on X axis. The ratio of signals for the two conditions can be roughly used as a metric for cross axis rejection. In our setup, the ratio was optimized to 125 with  $Z_{ac}$  amplitude at 12 V<sub>pp</sub>.

#### 4.7.4 Xe Drive Amplitude Optimization

For an open loop gyroscope operation, the Xe drive frequency needs to be applied at a certain amplitude such that there is maximum Xe signal detected by Rb magnetometer. This is achieved by slowly varying the drive amplitude and recording Xe amplitude for each iteration. A sample plot for Xe<sup>131</sup> is shown in Figure 4.18.

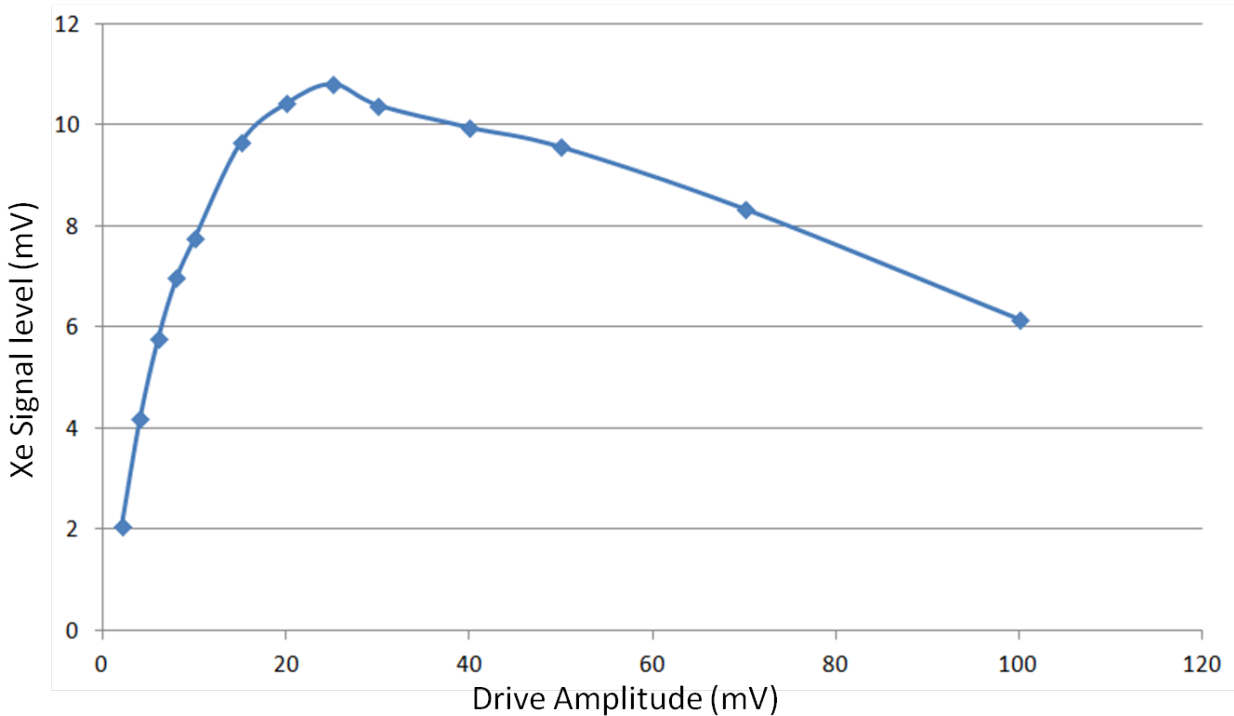


Figure 4.18: Drive amplitude optimization for Xe<sup>131</sup>

The SNR is also measured at the optimized amplitude. In our setup, the drive amplitude for Xe<sup>129</sup> was 16 mV<sub>pp</sub> at 40.5 Hz and for Xe<sup>131</sup> was 25 mV<sub>pp</sub> at 12 Hz. The corresponding SNR of Xe<sup>129</sup> = 38 dB, SNR of Xe<sup>131</sup> = 50 dB.

### 4.7.5 Estimation of pi and pi/2 pulses

In order to measure relaxation time measurements, the Xe isotopes need to be excited at the right frequency for the right duration with the correct amplitude to flip the magnetization exactly by  $90^\circ$ . This can be done in two ways, fixing the amplitude and varying the duration or number of cycles of the pulse at  $f_a$  or to keep the number of cycles or pulse duration constant and vary the amplitude of the pulse. In our experiments, we fix the number of cycles and vary the amplitude at the Xe precision frequency previously measured. The Xe signal is measured for each iteration of change in the amplitude. The figure of such a plot is shown in Figure 4.19. The maximum peak corresponds to the  $\frac{\pi}{2}$  pulse and the null corresponds to  $\pi$  pulse. The pulse generation, data capture and signal processing have all been performed using MATLAB and the Analog Discovery Data acquisition card.

- $\frac{\pi}{2}$  pulse for  $Xe^{129} = 10$  cycles of 40.5 Hz with amplitude of 170 mV
- $\frac{\pi}{2}$  pulse for  $Xe^{131} = 20$  cycles of 12 Hz with amplitude of 85 mV

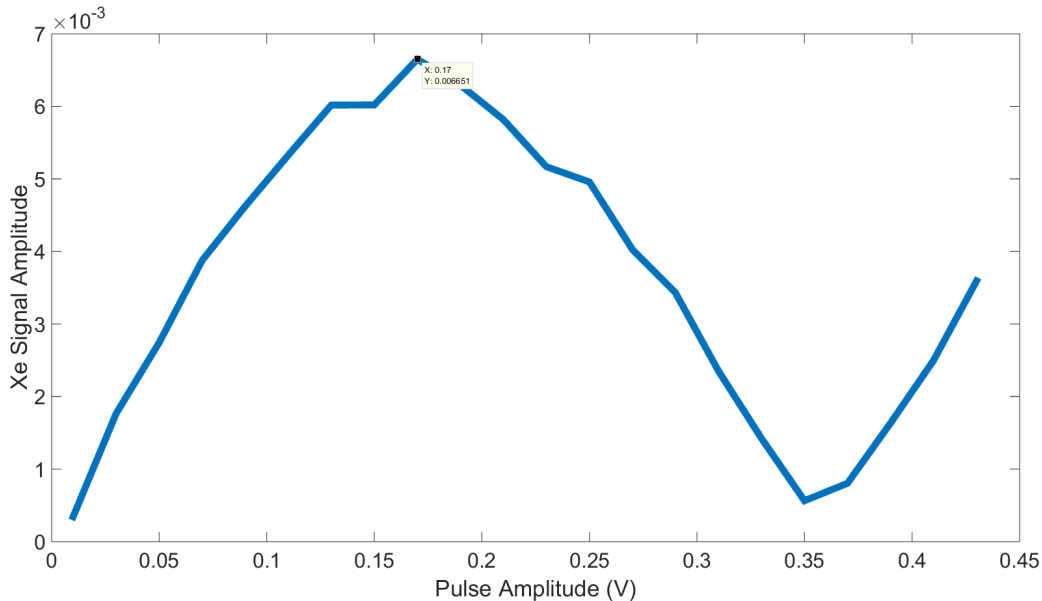


Figure 4.19: pi, pi/2 pulse amplitude optimization

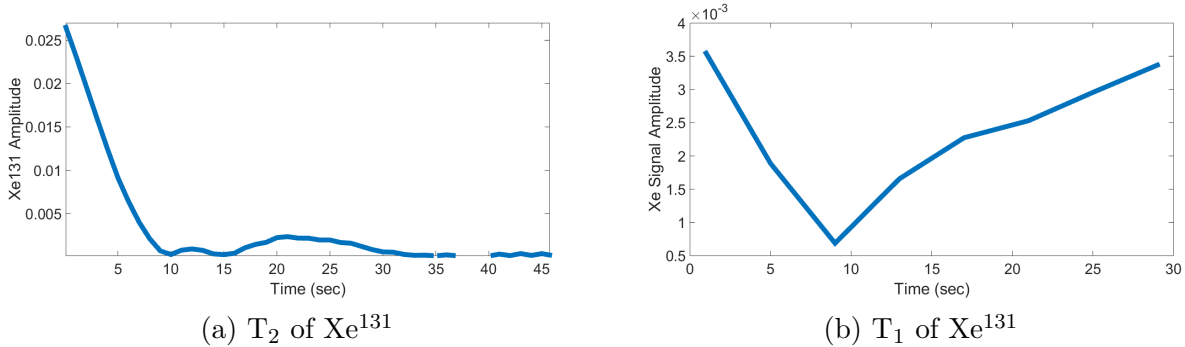


Figure 4.20: (left)  $T_2$  measurement, (right)  $T_1$  measurement

### 4.7.6 Relaxation Time Measurements

MATLAB scripts were written to generate the correct sequence of  $\pi$  and  $\frac{\pi}{2}$  pulse to estimate the  $T_1$  and  $T_2$  times for Xe. A detailed description of these measurements can be found in [61].

Flipping the Xe magnetization exactly by  $90^\circ$  and measuring the resultant decay signal would give the required  $T_2$ . So accurate measurement of  $T_2$  can be made with a single  $\frac{\pi}{2}$  pulse. For  $T_1$ , measurements, the application of pulses is slightly more involved.  $T_1$  measures the time it takes for Xe to get back to the original Z direction. Having Xe pointed in Z direction would not give us any signal to measure. So first a  $\pi$  pulse is applied to flip the Xe to opposite -ve Z direction. After sometime, the Xe tries to orient towards the +ve Z direction. With a slight delay, if a  $\frac{\pi}{2}$  is applied, Xe signal can be measured. The delay between the  $\pi$  and  $\frac{\pi}{2}$  pulses can be varied to get a plot as shown in Figure 4.20b. The delay time corresponding to the minimum is the estimate for  $T_1$ .

The Figure 4.20 shows a  $T_2$  of  $\text{Xe}^{131} \geq 6$  sec and a  $T_1$  of  $\text{Xe}^{131} \geq 13$  sec.

# Chapter 5

## Conclusion

A folded structure approach for NMRG was presented in this thesis. All the individual micro components were discussed in terms of designing, fabrication, and characterization details. A novel double-folded structure was designed and a complete assembled prototype was demonstrated. A complete table top setup for performing measurements on atomic vapor cells has been described in detail along with relevant experiments to eventually measure the relaxation times. MATLAB scripts for automated estimation of relaxation times have been developed to make faster measurements.

Attempts were made to assemble a functional micro NMRG using the components described in the thesis. Main challenges occurred due to cracking of polyimide and thus making the folded Helmholtz coils not functional as there was no electrical connection. Manual electric connection attempts were also made using conductive epoxy and soldering but no results could be achieved due to miniaturized size of the components.

## 5.1 Improvements on Current Work

Several optimizations on the setup were done to increase the Xe signal to get better estimates. Changing from Dehmlet to Faraday detection increased the results significantly. Also, changing the relative powers of pump and probe beam improved SNR by more than 20 dB. Another improvement was to have two different pump probe wavelengths at 795 nm and 780 nm respectively. With such optimizations on the current setup, the results till date are shown in this Table 5.1. These results are in collaboration with Mr. Radwan Mohammednoor at UCI.

<b>Xe Isotope</b>	<b>T<sub>1</sub> (sec)</b>	<b>T<sub>2</sub> (sec)</b>	<b>SNR (dB)</b>
Xe <sup>129</sup>	21.65	20.45	68
Xe <sup>131</sup>	23.78	18.06	74

Table 5.1: Xe relaxation times

## 5.2 Future Work

Some other materials are currently being explored in our lab to mitigate the cracking issue of polyimide. A lot of table top experiments using atomic vapor cells have been performed and the immediate next step would be to implement these experiments in a micro assembled NMRG based on the components described in this thesis. There have been several issues related to thermal design in this setup. Over long durations of time, there is a significant temperature drift causing the results to change over time. A proper temperature controller needs to be implemented to keep the results consistent. Also the micro shields can be used instead of the macro table top shields to miniaturize the whole setup and mimic the real application environment.

# Bibliography

- [1] M.Grewal, A.Andrews. “How Good Is Your Gyro [Ask the Experts]”, IEEE Control Systems Magazine, Vol.30, no.1, pp.12,86, Feb. 2010.
- [2] M.Larsen, M.Bulatowicz. “Nuclear Magnetic Resonance Gyroscope: For DARPA’s micro-technology for positioning, navigation and timing program”, IEEE International Frequency Control Symposium (FCS), Baltimore, MD, pp.1,5, 21-24 May 2012.
- [3] M.Armenise, C.Ciminelli, F.Dell’Olio, V.Passaro. (2011), “Advances in Gyroscope Technologies”, Available from <http://link.springer.com/>
- [4] J.Lyman. “Angular Velocity Responsive Apparatus”, US Patent No. 2,513,340, 1950.
- [5] D.Titterton, J.Weston. (2004), “Strapdown Inertial Navigation Technology”, Available from <http://app.knovel.com/web/index.v>
- [6] S.Murugesan. “Autonomous fault-tolerant attitude reference system using DTGs in symmetrically skewed configuration”, IEEE Transactions on Aerospace and Electronic Systems, Vol.25, no.2, pp.302,307, Mar. 1989.
- [7] V.Lappas. (2002), “A Control Moment Gyro (CMG) Based Attitude Control System (ACS) For Agile Small Satellites”, PhD Thesis, University of Surrey.
- [8] D.Rozelle. “The Hemispherical Resonator Gyro:From Wineglass to the Planets”, Proc. 19th AAS/AIAA Space Flight Mechanics Meeting, pp.1157-1178, Feb. 2009.
- [9] W.Chow, J.Gea-Banacloche, L.Pedrotti, V.Sanders, W.Schleich,M.Scully. “The ring laser gyro”, Reviews of Modern Physics, Vol.57, no.1, pp 61,104, Jan. 1985.
- [10] B.Culshaw, I.Giles. “Fibre optic gyroscopes”, Journal of Physics E: Scientific Instruments, Vol.16, no.1, Jan. 1983.
- [11] F.Dell’Olio, T.Tatoli, C.Ciminelli, M.Armenise. “Recent advances in miniaturized optical gyroscopes”, Journal of the European Optical Society - Rapid publications, Vol.9, Mar. 2014.
- [12] J.Fang, J.Qin. “Advances in Atomic Gyroscopes: A View from Inertial Navigation Applications”, Sensors, Vol.12, no.5, pp 6331-6346, May 2012.

- [13] A.Cronin, J.Schmiedmayer, D.Pritchard. “Optics and interferometry with atoms and molecules”, *Reviews of Modern Physics*, Vol.81, no.3, pp 1051,1129, July 2009.
- [14] T.Gustavson, P.Bouyer, M.Kasevich. “Precision Rotation Measurements with an Atom Interferometer Gyroscope”, *Physical Review Letters*, Vol.78, no.11, pp 2046, Mar. 1997.
- [15] J.Schaff, T.Langen, J.Schmiedmayer. (2015), “Interferometry with Atoms”, Available online at <http://arxiv.org/abs/1504.04285>.
- [16] K.Woodman<sup>1</sup>, P.Franks<sup>1</sup>, M.Richards<sup>1</sup>. “The Nuclear Magnetic Resonance Gyroscope: a Review”, *Journal of Navigation*, Vol.40, no.3, pp 366-384, Sept. 1987.
- [17] B.Grover, E.Kanegsberg, J.Mark, R.Meyer. “Nuclear Magnetic Resonance Gyro”, U.S.Patent No. 4,157,495, 1979.
- [18] S.Potts, J.Preston. “A Cryogenic Nuclear Magnetic Resonance Gyroscope”, *Journal of Navigation*, Vol.34, no.1, pp 19-37, Jan. 1981.
- [19] J.Simpson, J.Fraser, I.Greenwood. “An Optically Pumped Nuclear Magnetic Resonance Gyroscope”, *IEEE Transactions on Aerospace*, Vol.1, no.2, pp 1107-1110, Aug. 1963.
- [20] L.Iddings. “Electrostatically suspended gyroscope signal pickoff”, U.S.Patent No. 3320817 A, 1965.
- [21] N.Bruckner, R.Packard. “Large area multiturn superfluid phase slip gyroscope”, *Journal of Applied Physics*, Vol.93,pp 1798-1805, 2003.
- [22] J.Bernstein, S.Cho, A.King, A.Kourepennis, P.Maciel, M.Weinberg. “A micromachined comb-drive tuning fork rate gyroscope”, *Proceedings:An Investigation of Micro Structures, Sensors, Actuators, Machines and Systems,IEEE MEMS*, Fort Lauderdale, FL, pp 143-148, 7-10 Feb. 1993.
- [23] M.Zaman, A.Sharma, Z.Hao, F.Ayazi. “A Mode-Matched Silicon-Yaw Tuning-Fork Gyroscope With Subdegree-Per-Hour Allan Deviation Bias Instability”, *IEEE Journal of Microelectromechanical Systems*, Vol.17, no.6, pp 1526,1536, Dec. 2008.
- [24] F.Ayazi, K.Najafi. “A HARPSS polysilicon vibrating ring gyroscope”, *IEEE Journal of Microelectromechanical Systems*, Vol.10, no.2, pp 169,179, June 2001.
- [25] A.Trusov, I.Prikhodko, S.Zotov, A.Schofield, A.Shkel. “Ultra-high Q silicon gyroscopes with interchangeable rate and whole angle modes of operation”, *IEEE Sensors*, Kona, HI, pp 864,867, 1-4 Nov. 2010.
- [26] I.Prikhodko, S.Zotov, A.Trusov, A.Shkel. “Sub-degree-per-hour silicon MEMS rate sensor with 1 million Q-factor”, *16th International Conference on Solid-State Sensors, Actuators and Microsystems(TRANSDUCERS)*, Beijing, pp 2809,2812, 5-9 June 2011.

- [27] D.Senkhal, M.Ahamed, M.Ardakani, S.Askari, A.Shkel. “Demonstration of 1 Million Q-Factor on Microglassblown Wineglass Resonators With Out-of-Plane Electrostatic Transduction”, IEEE/ASME Journal of Microelectromechanical Systems, Vol.24, no.1, pp 29-37, Feb. 2015.
- [28] J.Cho, T.Nagourney, A.Darvishian, B.Shiari, J.Woo, K.Najafi, “Fused silica micro bird-bath shell resonators with 1.2 million Q and 43 second decay time constant”, in Proceedings Solid-State Sensors, Actuators, Microsystems Conference (Hilton Head), Hilton Head Island, SC, USA, pp 103104, 2014.
- [29] S.Knappe, V.Shah, P.Schwindt, L.Hollberg, J.Kitching, L.Liew, J.Moreland. “A micro-fabricated atomic clock”, Applied Physics Letters, Vol. 85, no. 9, pp 14601462, 2004.
- [30] T.Kornack, R.Ghosh, M.Romalis. “Nuclear Spin Gyroscope Based on an Atomic Comagnetometer”, Physical Review Letters, Vol. 95, no. 23, p 230801, Nov. 2005.
- [31] K.Kominis, T.Kornack, J.Allred, MRomalis. “A subfemtotesla multichannel atomic magnetometer”, Letters to Nature, Vol. 422, no. 6932, pp. 596-599, 2003.
- [32] A.Shkel. “Microtechnology Comes of Age”, GPS World, 2011, Available on at, <http://gpsworld.com/defense-warfighter-microtechnology-comes-age/>.
- [33] A.Shkel. “Expert Advice: The Chip-Scale Combinatorial Atomic Navigator”, GPS World, 2013, Available on at, <http://gpsworld.com/expert-advice-the-chip-scale-combinatorial-atomic-navigator/>.
- [34] E.Eklund, A.Shkel, S.Knappe, E.Donley, J.Kitching. “Spherical rubidium vapor cells fabricated by micro glass blowing”, IEEE 20th International Conference on Micro Electro Mechanical Systems, Hyogo, pp 171,174, 21-25 Jan. 2007.
- [35] E.Eklund. (2008). “Microgyroscope Based on Spin Polarized Nuclei”, PhD Thesis, University of California Irvine.
- [36] B.Samuels, S.Parker. “Optical Pumping”, Available online at <http://internal.physics.uwa.edu.au/stamps/2006Y3Lab/SteveAndBlake/theoretical.html>
- [37] R.Beth. “Mechanical Detection and Measurement of the Angular Momentum of Light”, Physical Review Letters, Vol.50, no.2, pp 115-125, July 1936.
- [38] R.Pooser, A.Marino, V.Boyer, K.Jones, P.Lett. “Quantum correlated light beams from non-degenerate four-wave mixing in an atomic vapor: the D1 and D2 lines of 85Rb and 87Rb”, Optics Express Vol.17, no.19, pp 16722-16730, Sept. 2009.
- [39] D.Steck. “Rubidium 85 D Line Data”, (2013), Available online at <http://steck.us/alkalidata>.
- [40] D.Steck. “Rubidium 87 D Line Data”, (2010), Available online at <http://steck.us/alkalidata>.

- [41] W.Happer, Y.Jau, T.Walker. (2010), “Optically Pumped Atoms”, Wiley-VCH Verlag.
- [42] T.Walker, W.Happer. “Spin-exchange optical pumping of noble-gas nuclei”, *Reviews of Modern Physics*, Vol.69, no.2, pp 629-642, Apr. 1997.
- [43] J.Hornak. “The Basics of NMR”, (2011), Available online at <https://www.cis.rit.edu/htbooks/nmr/inside.htm>.
- [44] J.Keeler. “Understanding NMR Spectroscopy”, 2nd edition, 2010.
- [45] C.Cohen-Tannoudji, J.Dupont-Roc, S.Haroche, F.Laloe, “Diverses resonances”, *Revue de Physique Appliquee*, 1970.
- [46] E.Donley. “Nuclear magnetic resonance gyroscopes”, *IEEE Sensors*, Kona, HI, pp 17,22, 1-4 Nov. 2010.
- [47] H.Dehmelt. “Modulation of a Light Beam by Precessing Absorbing Atoms”, *Physical Review Letters*, Vol.105, no.6, pp 1924-1925, Mar. 1957.
- [48] W.Bell, A.Bloom. “Optical Detection of Magnetic Resonance in Alkali Metal Vapor”, *Physical Review Letters*, Vol.107, no.6, pp 1559-1565, Sept. 1957.
- [49] A.Kastler. “Optical Methods of Atomic Orientation and of Magnetic Resonance”, *Journal of the Optical Society of America*, Vol.47, no.6, pp 460-465, Jun. 1957.
- [50] J.Mort, F.Luty, F.Brown. “Faraday Rotation and Spin-Orbit Splitting of the F Center in Alkali Halides”, *Physical Review Letters*, Vol.137, no.2A, pp A566-A573, Jan. 1965.
- [51] T.Kornack.(2005), “A Test of CPT and Lorentz Symmetry Using a K-He<sup>3</sup> Co-magnetometer”, PhD Thesis, Princeton University.
- [52] M.Bulatowicz. “Temperature system with magnetic field suppression”, US Patent No. 8,138,760 B2, 2012.
- [53] E.Eklund, A.Shkel. “Glass Blowing on a Wafer Level”, *IEEE Journal of Microelectromechanical Systems*, Vol.16, no.2, pp 232,239, Apr. 2007.
- [54] A.Trusov, M.Rivers, S.Zotov, A.Shkel. “Three dimensional folded mems technology for multi-axis sensor systems”, US Patent No. 20120032286 A1, 2012.
- [55] S.Zotov, M.Rivers, A.Trusov, A.Shkel. “Chip-scale IMU using folded-mems approach”, *IEEE Sensors*, Kona, HI, pp 1043-1046, 1-4 Nov. 2010.
- [56] A.Efimovskaya, D.Senkal, S.Askari, A.Shkel. “Origami-like folded MEMS for realization of TIMU: fabrication technology and initial demonstration”, *IEEE International Symposium on Inertial Sensors and Systems (ISISS)*, Hapuna Beach, HI, pp 1-4, 23-26 Mar. 2015.
- [57] M.Perez, U.Nguyen, S.Knappe, E.Donley, J.Kitching, A.Shkel. “Rubidium Vapor Cell with Integrated Nonmetallic Multilayer Reflectors”, *IEEE 21st International Conference on Micro Electro Mechanical Systems*, Tucson, AZ, pp 790-793, 13-17 Jan. 2008.

- [58] E.Donley, E.Hodby, L.Hollberg, J.Kitching. “Demonstration of high-performance compact magnetic shields for chip-scale atomic devices”, *Review of Scientific Instruments*, Vol.78, no.8, 2007.
- [59] P.Harle, G.Wackerle, M.Mehring. “A Nuclear-Spin Rotation Sensor Using Optical Polarization and Detection Methods”, *Applied Magnetic Resonance*, Vol.5, no.2, pp 207-220, Oct. 1993.
- [60] D. Senkal.(2009), “Haptic surgical aid system with magnetorheological brakes for dental implants”, Master’s Thesis, Washington State University, Vancouver.
- [61] J. Mirijanian.(2012), “Techniques to characterize vapor cell performance for a nuclear-magnetic-resonance gyroscope”, Master’s Thesis, California Polytechnic State University, San Luis Obispo.

# Appendix A

## Vendors

### Optics

These optical components have been used for the NMR setup described in Chapter 4. Most of the equipment was purchased.

#### **Newport Corp.,**

1791 Deere Avenue, Irvine, CA, 92606.

Contact: 949-863-3144.

Website: <http://www.newport.com>

They have a very good optical rails, mounts and lens mounts for optical table and the delivery is very quick. Typical lead time is around 1 week.

#### **Thorlabs Inc.,**

56 Sparta Avenue, Newton, New Jersey, 07860.

Contact: 973-579-7227.

Website: <http://www.thorlabs.us>

They have a huge collection of lenses, optical alignment tools, photo detectors, VCSEL controllers and are always very prompt with the delivery. Typical lead time is around 1 week.

**CVI laser optics,**

200 Dorado Place SE, Albuquerque, NM 87123.

Contact: 505-296-9541.

Website: <https://www.cvimellesgriot.com/>

They have a very wide collection of lenses with many focal lengths for use during beam expansion or compression. Typical lead time is around 2-3 weeks.

**Si Wafers**

The Si wafers were used for fabrication of micro components described in Chapter 3. They have a very wide range of wafers for different thickness and polished sides. Typical lead time is around 2 weeks.

**Ultrasil Corporation,**

3527 Breakwater Ave, Hayward, CA, 94545.

Contact: 510-266-3700.

Website: <http://www.ultrasil.com/>

**Fabrication Masks**

The L-Edit layout designs are submitted to the following company and corresponding masks are delivered within 2 weeks. There are some cheaper options for masks, if the device feature sizes are not very critical. These masks were used for fabrication as described in Chapter 3.

**Photo-sciences,**

2542 W 237th St., Torrance, CA, 90505.

Contact: 310-634-1500.

Website: <https://dev.photo-sciences.com/>

### **VCSEL**

They have 1 mW power VCSEL that do not exhibit any polarization switching. 2 VCSEL's at 795 nm were bought and all the experiments described in chapter 4 were performed using this. The lead time is around 5-6 weeks.

### **M2 Photonics LLC,**

10280 Brier Mill, Johns Creek, GA, 30022 .

Contact: 678-907-3904.

Website: <http://www.m2photonics.com/>

### **High Power Laser**

Two high power lasers (around 70 mW) with tunable range from 780 to 800 nm were used for NMR experiments described in Chapter 4. The lead time is around 3-4 weeks.

### **Toptica Photonics Inc.,**

1286 Blossom Dr, Victor, NY, 14564 .

Contact: 585-657-6663.

Website: <http://www.toptica.com/>

### **Function Generator Amplifier**

They have a wide range of FGA to amplify the signal output from a typical function generators that do not have high output current ratings. The AC heating for NMR experiments described in Chapter 4 was done using this. Typical lead time is less than 1 week.

### **Accel Instruments,**

4521 Campus Dr., Suite 254, Irvine, CA, 92612.

Contact: 949-923-5974.

Website: <http://www.accelinstruments.com/>

### **Magnetic Shields**

The custom made magnetic shields described in chapter 3, were designed and submitted to Amuneal. Based on the manufacturing tolerances, the shields had to be redesigned. The lead time varies from 5 to 10 weeks.

#### **Amuneal Manufacturing Corp,**

4737 Darrah Street, Philadelphia, PA, 19124.

Contact: 215-535-3000.

Website: <http://www.amuneal.com/>